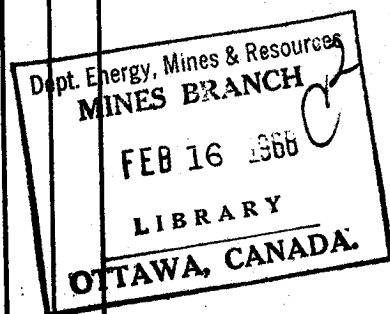CANADA

DEPARTMENT OF
ENERGY, MINES AND RESOURCES
MINES BRANCH

THE ANALYSIS OF STRESS FOR
THE PREDICTION OF
CRATER BOUNDARIES

K. SASSA, G. E. LAROCQUE, D. F. COATES

AND J. A. DARLING

FUELS AND MINING PRACTICE DIVISION

NOVEMBER 1966

1867 1967

Price $1.25

Mines Branch Research Report R 192

THE ANALYSIS OF STRESS FOR THE PREDICTION OF CRATER BOUNDARIES

by

K. Sassa[*], G.E. Larocque[**], D.F. Coates[***]
and J.A. Darling[****]

- - - -

ABSTRACT

A method of analysis is developed to compute the stress distribution resulting from detonation of a contained spherical charge in an elastic medium in the vicinity of a free face. This analysis uses the dynamic elastic properties of the medium, and the direct dilatational displacement and particle velocity wave shapes produced by the explosive, as a function of distance. Principal stresses at a point, as a function of time, are computed by superposition of the stress components due to the direct dilatational wave and the reflected dilatational and shear waves, using plane wave reflection theory. A computer program has been written to perform this analysis.

Laboratory and field measurements were used to obtain the necessary data to determine stress distribution and to predict crater dimensions. In the field experiments, a direct dilatational wave linear array and a shear wave linear array were used to determine all displacements and particle velocity wave shape data, as well as the dilatational wave velocity and shear wave velocity. It was found that only moderate changes occurred in displacement and particle velocity wave shape with distance. Both displacement and particle velocity decayed with distance according to a power law relationship in the range considered.

[*]Department of Mineral Science and Technology, Kyoto University, Kyoto, Japan; former National Research Council of Canada Research Fellow at the Mining Research Laboratories, Mines Branch, Ottawa (1963-1965).

[**]Research Scientist and [***]Head, Mining Research Laboratories, Fuels and Mining Practice Division, Mines Branch, Department of Energy, Mines and Resources, Ottawa, Canada.

[****]Research Scientist, Canadian Explosives Research Laboratory, Fuels and Mining Practice Division, Mines Branch, Department of Energy, Mines and Resources, Ottawa, Canada.

Two explosives were used in the field program. It was found that the ratio of the detonation pressures of these two explosives, corrected to the ratio of the imposed pressure of these two explosives by means of an acoustical coupling relationship, were in agreement with the ratio of the peak radial stress as determined in the computer program for the two explosives at equal distances from a shot centre.

Some agreement was found between predicted crater dimensions and those actually observed.

Direction des mines

Rapport de recherches R 192

L'ANALYSE DE LA TENSION POUR LA PRÉDICTION DES LIMITES D'UN CRATÈRE

par

K. Sassa*, G. E. Larocque**, D. F. Coates***
et J. A. Darling****

RÉSUMÉ

Une méthode d'analyse a été créée pour calculer la distribution de la tension résultant de la détonation d'une charge sphérique confinée dans un milieu élastique au voisinage d'une surface libre. Cette analyse utilise les propriétés élastiques dynamiques du milieu, ainsi que le déplacement direct en dilatation et les formes d'onde de la vitesse matérielle produites par l'explosif, en fonction de la distance. Les éléments principaux de la tension en un point sont calculés en fonction du temps en superposant les composantes de la tension produite par l'onde incidente de dilatation et par les ondes réfléchies de dilatation et de distorsion, en faisant appel à la théorie de la réflexion des ondes planes. Un programme pour l'ordinateur a été écrit afin de faire cette analyse.

Des mesures obtenues en laboratoire et sur le terrain ont été utilisées afin d'obtenir les données nécessaires pour déterminer la distribution de la tension et pour prédire les dimensions des cratères. Dans les essais sur le terrain, on s'est servi d'un réseau linéaire pour l'onde incidente de dilatation et d'un réseau linéaire pour l'onde de distorsion, afin d'obtenir des données sur les formes d'onde de la vitesse matérielle, l'ensemble des déplacements, ainsi que les vitesses des ondes de dilatation et

*Département de Science et de Technologie minières, Université de Kyoto, Kyoto, Japon; autrefois Attaché de recherche du Conseil National des Recherches du Canada aux Laboratoires de recherche minière, Direction des mines, Ottawa (1963-1965).
**Chargé de recherche et ***Directeur, Laboratoire de recherche minière, Division des combustibles et du génie minier, Direction des mines, Ministère de l'Energie, des Mines et des Ressources, Ottawa, Canada.
****Chargé de recherche, Laboratoire canadien de la recherche sur les explosifs, Division des combustibles et du génie minier, Direction des mines, Ministère de l'Energie, des Mines et des Ressources, Ottawa, Canada.

et de distorsion. On a trouvé que les formes d'onde de la vitesse matérielle et le déplacement ne subissent pas de variation radicale avec la distance. Le déplacement et la vitesse matérielle s'amortissent tous deux comme une puissance de la distance dans le domaine étudié.

Deux explosifs ont été utilisés dans les travaux sur le terrain. On a trouvé que le rapport des pressions de détonation de ces deux explosifs, ajusté au rapport des pressions imposées des deux explosifs au moyen d'une relation de couplage acoustique, était en accord avec le rapport des tensions radiales de pointe, déterminées par le programme de calcul pour les deux explosifs à des distances égales du centre de détonation.

On a trouvé un certain accord entre les dimensions prévues des cratères et les dimensions observées en fait.

CONTENTS

CONTENTS (concluded)

TABLES

FIGURES

FIGURES (continued)

FIGURES (continued)

FIGURES (continued)

FIGURES (concluded)

- - -

1. INTRODUCTION

One possible approach to the prediction of the crater produced by the detonation of an explosive charge in a rock mass in the vicinity of a free face, is to make an analysis combining a knowledge of the dynamic failure criteria for the material with a knowledge of the stress distribution that is produced within the rock mass by the detonation.

Recently, such a method of analysis has been reported (1). A maximum tensile failure for the material was assumed in this analysis, and the stress distribution was determined on the basis of elastic theory. In the case of small explosive charges, good agreement with this approach has been reported between predicted and realized craters.

In the present report, this method of analysis has been extended to attempt prediction of craters produced with much larger explosive charges. Continued investigation of the coupling phenomena between rock and explosive, which is a subject of considerable general interest (2, 3, 4, 5), is also reported.

2. METHOD OF STRESS ANALYSIS[4, 6]

The main stress wave projected into a surrounding medium by the explosion of a confined spherical charge is a longitudinal wave. As a result, in the case of blasting near one free face, the stress at any point A near the free face is a product of the three stress waves shown in Figure 1. Initially, at points behind the free face, the longitudinal wave projected directly in the rock establishes the stress conditions. In time, the reflected longitudinal and reflected transverse waves, in that order of appearance, contribute to the stress conditions at locations behind the free face.

In the present study the time-dependent stress conditions resulting from detonation of a contained charge in the vicinity of a free face are synthesized by consideration of these three wave motions. Hereafter in this report, these three wave motions are denoted as IP, RP and RS, and quantities concerning these wave motions are indicated by the suffixes ip, rp and rs respectively.
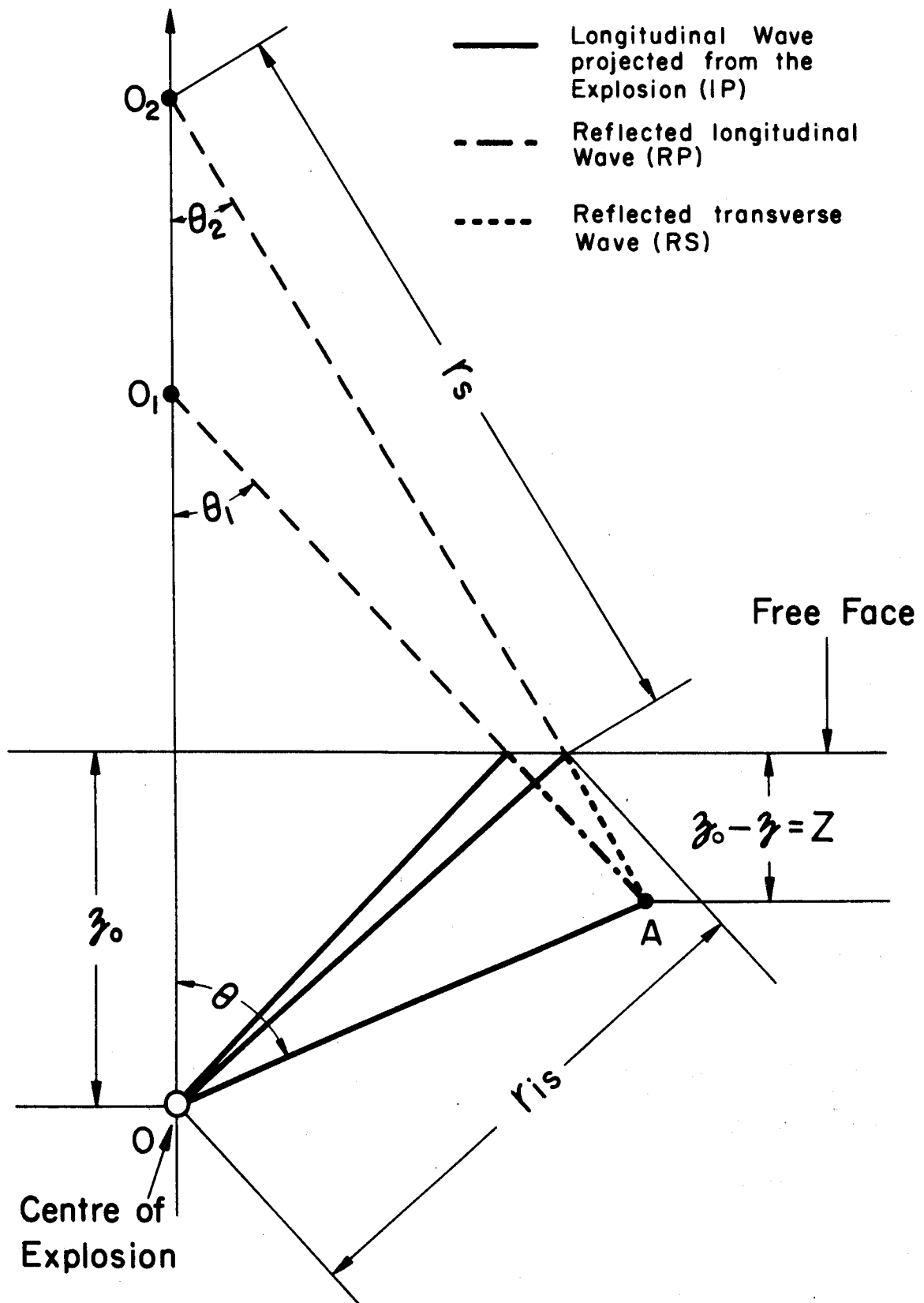
Figure 1. Spherical coordinate systems used in the analysis.

First of all, let the spherical charge under consideration be established at the origin of a polar coordinate system, with coordinates r, θ and ϕ contained within a homogeneous, ideally elastic medium of density ρ of infinite extent. θ is the angle in a vertical plane and ϕ the angle in the horizontal plane, with the subscript t used instead of ϕ on various symbols. According to the theory of elasticity, the strain components (ϵ_r, ϵ_θ, ϵ_t, $\gamma_{\theta t}$, γ_{rt}, $\gamma_{r\theta}$) at an arbitrary point in the medium are shown as follows:

$$
\left.
\begin{aligned}
\epsilon_r &= \frac{\partial U_r}{\partial r} \\[2mm]
\epsilon_\theta &= \frac{1}{r} \frac{\partial U_\theta}{\partial \theta} + \frac{U_r}{r} \\[2mm]
\epsilon_t &= \frac{1}{r \sin \theta} \cdot \frac{\partial U_t}{\partial \phi} + \frac{U_\theta}{r} \cdot \cot \theta + \frac{U_r}{r} \\[2mm]
\gamma_{\theta t} &= \frac{1}{r}\left(\frac{\partial U_t}{\partial \theta} - U_t \cot \theta\right) + \frac{1}{r \sin \theta} \cdot \frac{\partial U_\theta}{\partial \phi} \\[2mm]
\gamma_{rt} &= \frac{1}{r \sin \theta} \cdot \frac{\partial U_r}{\partial \phi} + \frac{\partial U_t}{\partial r} - \frac{U_t}{r} \\[2mm]
\gamma_{r\theta} &= \frac{\partial U_\theta}{\partial r} - \frac{U_\theta}{r} + \frac{1}{r} \frac{\partial U_r}{\partial \theta}
\end{aligned}
\right\} \quad \text{Eq. 1}
$$

where U_r, U_θ, U_t are the components of displacement in the r, θ and ϕ directions.

Also, the stress components (σ_r, σ_θ, σ_t, $\tau_{\theta t}$, τ_{rt}, $\tau_{r\theta}$) at that point are as follows:

$$
\left.
\begin{aligned}
\sigma_r &= (\lambda + 2\mu)\epsilon_r + \lambda(\epsilon_\theta + \epsilon_t) \\[1mm]
\sigma_\theta &= (\lambda + 2\mu)\epsilon_\theta + \lambda(\epsilon_t + \epsilon_r) \\[1mm]
\sigma_t &= (\lambda + 2\mu)\epsilon_t + \lambda(\epsilon_r + \epsilon_\theta) \\[1mm]
\tau_{\theta t} &= \mu\gamma_{\theta t} \\[1mm]
\tau_{rt} &= \mu\gamma_{rt} \\[1mm]
\tau_{r\theta} &= \mu\gamma_{r\theta}
\end{aligned}
\right\} \quad \text{Eq. 2}
$$

where λ, μ are Lamé's constants.

The components (U_r, U_θ, U_t) of displacement resulting from the direct longitudinal wave can be written in the following form:

$$U_r = U(r, T_{ip}),$$

$$U_\theta = U_t = 0,$$

$$\left.\right\} \text{Eq. 3}$$

where

$$T_{ip} = t - r/C_L,$$

t = time from the instant of detonation,

r = distance from the origin of the coordinate, and

C_L = propagation velocity of longitudinal wave in the medium.

Using Equations 1, 2 and 3, it can be shown that the stresses resulting from IP can be expressed as follows:

$$\sigma_{r\,ip} = (\lambda + 2\mu)\partial U(r, T_{ip})/\partial r + 2\lambda \cdot U(r, T_{ip})/r$$

$$\sigma_{\theta\,ip} = \sigma_{t\,ip} = \lambda \partial U(r, T_{ip})/\partial r + 2(\lambda + \mu)\cdot U(r, T_{ip})/r$$

$$\tau_{\theta t\,ip} = \tau_{rt\,ip} = \tau_{r\theta\,ip} = 0.$$

$$\left.\right\} \text{Eq. 4}$$

As displacement changes with time, the displacement $U(r, T_{ip})$ can be expressed as a product of $U_p(r)$ and $U_w(T_{ip})$, where $U_p(r)$ is a function of r and determines the peak value of the displacement, and $U_w(T_{ip})$ is a function of T_{ip} and indicates the wave shape or change in displacement with time, namely:

$$U_r = U(r, T_{ip}) = U_p(r) \cdot U_w(T_{ip}). \qquad \text{Eq. 5}$$

Then, by performing a partial differentiation on the radial displacement with respect to r, the following equation is realized:

$$\frac{\partial U(r, T_{ip})}{\partial r} = \frac{dU_p(r)}{dr} U_w(T_{ip}) + \frac{dU_w(T_{ip})}{dT_{ip}} \cdot \frac{\partial T_{ip}}{\partial r} \cdot U_p(r) \qquad \text{Eq. 6}$$

By definition, the radial particle velocity, $V(r, T_{ip})$, is the partial derivative of radial displacement with respect to time, and

$$V(r, T_{ip}) = \frac{\partial U(r, T_{ip})}{\partial t} = \frac{dU_w(T_{ip})}{dT_{ip}} \cdot \frac{\partial T_{ip}}{\partial t} \cdot U_p(r) \qquad \text{Eq. 7}$$

Also, since $T_{ip} = t - r/C_L$,

$$\left.\begin{aligned} \partial T_{ip}/\partial r &= -1/C_L \\[2ex] \partial T_{ip}/\partial t &= 1. \end{aligned}\right\} \text{Eq. 8}$$

Then, by substituting Equations 7 and 8 in Equation 6, the following equation is obtained:

$$\frac{\partial U(r, T_{ip})}{\partial r} = \frac{dU_p(r)}{dr} \cdot U_w(T_{ip}) - \frac{V(r, T_{ip})}{C_L} \qquad \text{Eq. 9}$$

Substitution of Equation 9 into Equation 4 gives:

$$\left.\begin{aligned} \sigma_{r\,ip} &= (\lambda + 2\mu)\left\{\frac{dU_p(r)}{dr} \cdot U_w(T_{ip}) - \frac{V(r, T_{ip})}{C_L}\right\} + 2\lambda\,\frac{U(r, T_{ip})}{r} \\[3ex] \sigma_{\theta\,ip} = \sigma_{t\,ip} &= \lambda\left\{\frac{dU_p(r)}{dr} \cdot U_w(T_{ip}) - \frac{V(r, T_{ip})}{C_L}\right\} + 2(\lambda + \mu)\,\frac{U(r, T_{ip})}{r} \end{aligned}\right\} \text{Eq. 10}$$

$$\tau_{\theta t\,ip} = \tau_{rt\,ip} = \tau_{r\theta\,ip} = 0.$$

Lamé's constants λ and μ can be obtained from a knowledge of the longitudinal and shear wave velocities, using the following equations:

$$C_L = \sqrt{(\lambda + 2\mu)/\rho}, \qquad \text{Eq. 11}$$

$$C_T = \sqrt{\mu/\rho}, \qquad \text{Eq. 12}$$

where C_L is the longitudinal wave velocity, C_T the shear wave velocity, and ρ the density of the medium.

Next, let us consider the stresses caused at a point by RP. The analysis of the stresses caused by RP is simplified by using the spherical

coordinates (r_1, θ_1, ϕ_1). The origin 0_1 is located on a continuation of the normal line joining charge centre 0 to the free face, as shown in Figure 1. Its exact location is the intersection of this line with a projection of the line indicating the direction of the reflected longitudinal wave. By using this coordinate system, the displacement and the particle velocity caused by RP occur only in the r_1 direction and are given by:

$$
\left.
\begin{aligned}
U_1(r_1, \theta_1, T_{rp}) &= U_{p_1}(r_1, \theta_1) \cdot U_{w_1}(T_{rp}) = A_{rp}(\theta_1) \cdot U_p(r_1) \cdot U_{w_1}(T_{rp}) \\
V_1(r_1, \theta_1, T_{rp}) &= V_{p_1}(r_1, \theta_1) \cdot V_{w_1}(T_{rp}) = A_{rp}(\theta_1) \cdot V_p(r_1) \cdot V_{w_1}(T_{rp})
\end{aligned}
\right\} \quad \text{Eq. 13}
$$

where $T_{rp} = t - r_1/C_L$ and $A_{rp}(\theta_1)$, which is a function of θ_1, indicates the ratio of the amplitude of RP to that of the incident longitudinal wave at the free face. Therefore by referring to Equations 1 and 2, the stresses caused by RP are given by:

$$
\sigma_{r\,rp} = (\lambda + 2\mu)\left\{ \frac{\partial U_{p1}(r_1, \theta_1)}{\partial r_1} \cdot U_{w_1}(T_{rp}) - \frac{V_1(r_1, \theta_1, T_{rp})}{C_L} \right\} + 2\lambda \frac{U_1(r_1, \theta_1, T_{rp})}{r_1}
$$

$$
\sigma_{\theta\,rp} = \sigma_{t\,rp} = \lambda\left\{ \frac{\partial U_{p1}(r_1, \theta_1)}{\partial r_1} \cdot U_{w_1}(T_{rp}) - \frac{V_1(r_1, \theta_1, T_{rp})}{C_L} \right\} + 2(\lambda + \mu) \frac{U_1(r_1, \theta_1, T_{rp})}{r_1}
$$

$$
\tau_{r\theta\,rp} = \mu \cdot \frac{1}{r} \cdot \frac{\partial U_{p1}(r_1, \theta_1)}{\partial \theta_1} \cdot U_{w_1}(T_{rp})
$$

$$
\tau_{\theta t\,rp} = \tau_{rt\,rp} = 0.
$$

<div align="right">Eq. 14</div>

Lastly, let us consider the stresses due to RS. In this case, spherical coordinates (r_2, θ_2, ϕ_2) with the origin at 0_2 are used to simplify the problem as shown in Figure 1. By using these polar coordinates, the displacement and the particle velocity caused by RS are in the θ_2 direction, and are given by:

$$
\left.
\begin{aligned}
U_\theta(r_2, \theta_2, T_{rs}) &= U_{\theta p}(r_2, \theta_2) \cdot U_{\theta w}(T_{rs}) \\
V_\theta(r_2, \theta_2, T_{rs}) &= V_{\theta p}(r_2, \theta_2) \cdot V_{\theta w}(T_{rs}),
\end{aligned}
\right\} \quad \text{Eq. 15}
$$

where $T_{rs} = t - r_{is}/C_L - (r_2 - r_s)/C_T$.

Therefore, by referring to Equations 1 and 2, the stresses induced by RS are given by:

$$\sigma_{r\,rs} = \lambda \left\{ \frac{1}{r_2} \cdot \frac{\partial U_{\theta p}(r_2, \theta_2)}{\partial \theta_2} \cdot U_{\theta w}(T_{rs}) + \frac{U_{\theta p}(r_2, \theta_2)}{r_2} \cdot U_{\theta w}(T_{rs}) \cot \theta_2 \right\}$$

$$\sigma_{\theta\,rs} = (\lambda + 2\mu) \cdot \frac{1}{r_2} \frac{\partial U_{\theta p}(r_2, \theta_2)}{\partial \theta_2} \cdot U_{\theta w}(T_{rs}) + \lambda \frac{U_{\theta p}(r_2, \theta_2)}{r_2} \cdot U_{\theta w}(T_{rs}) \cot \theta_2$$

$$\sigma_{t\,rs} = (\lambda + 2\mu) \cdot \frac{U_{\theta p}(r_2, \theta_2)}{r_2} \cdot U_{\theta w}(T_{rs}) \cdot \cot \theta_2 + \lambda \frac{1}{r} \cdot \frac{\partial U_{\theta p}(r_2, \theta_2)}{\partial \theta_2} \cdot U_{\theta w}(T_{rs})$$

$$\tau_{r\theta\,rs} = \mu \left\{ \frac{\partial U_{\theta p}(r_2, \theta_2)}{\partial r_2} \cdot U_{\theta w}(T_{rs}) - \frac{V_{\theta p}(r_2, \theta_2)}{C_T} \cdot V_{\theta w}(T_{rs}) - \frac{U_{\theta p}(r_2, \theta_2)}{r_2} \cdot U_{\theta w}(T_{rs}) \right\}$$

$$\tau_{\theta t\,rs} = \tau_{rt\,rs} = 0. \qquad\qquad \text{Eq. 16}$$

The attenuations of the maximum displacement and the maximum particle velocity caused by longitudinal and transverse waves can be assumed, within restricted ranges, to follow an inverse power function of distance. Therefore, the displacements and the particle velocities caused by IP, RP and RS can be expressed as follows:

$$U(r, T_{ip}) = A_o \cdot r^{-n} \cdot U_w(T_{ip})$$

$$V(r, T_{ip}) = B_o \cdot r^{-m} \cdot V_w(T_{ip})$$

$$U_1(r_1, \theta_1, T_{rp}) = A_{rp}(\theta_1) \cdot A_o \cdot r^{-n} \cdot U_{w1}(T_{rp})$$

$$V_1(r_1, \theta_1, T_{rp}) = A_{rp}(\theta_1) \cdot B_o \cdot r^{-m} \cdot V_{w1}(T_{rp}) \qquad\qquad \text{Eq. 17}$$

$$U_\theta(r_2, \theta_2, T_{rs}) = A_{rs}(\theta_2) \cdot A_o \cdot r_{is}^{-n} \cdot (r_s/r_2)^h \cdot U_{\theta w}(T_{rs})$$

$$V_\theta(r_s, \theta_2, T_{rs}) = A_{rs}(\theta_2) \cdot B_o \cdot r_{is}^{-m} \cdot (r_s/r_2)^k \cdot V_{\theta w}(T_{rs})$$

where A_o is a displacement intercept; B_o is a particle velocity intercept; n and m are the decay exponents of radial displacement and particle velocity caused by the longitudinal wave; h and k are the decay exponents of the transverse wave; and $A_{rp}(\theta_1)$ and $A_{rs}(\theta_2)$, functions of θ_1 and θ_2, indicate the ratio of the amplitude of RP and RS to that of the incident longitudinal wave at the free face.

Furthermore, according to the theory of reflection of an elastic wave, the wave shape does not change on reflection, therefore the following relations are valid:

$$U_w = U_{w1} = U_{\theta w}$$

$$V_w = V_{w1} = V_{\theta w}$$

$$\left.\right\} \text{Eq. 18}$$

equations: $A_{rp}(\theta_1)$ and $A_{rs}(\theta_2)$ were determined, using the following

$$A_{rp}(\theta_1) = \frac{\sin 2\theta_1 \sin 2j - (C_L/C_T)^2 \cdot \cos^2 2j}{\sin 2\theta_1 \sin 2j + (C_L/C_T)^2 \cdot \cos^2 2j} \qquad \text{Eq. 19}$$

$$\sin j = C_T \cdot \sin \theta_1/C_L$$

$$A_{rs}(\theta_2) = \frac{2(C_L/C_T) \cdot \sin 2i \cdot \cos 2\theta_2}{\sin 2i \cdot \sin 2\theta_2 + (C_L/C_T)^2 \cdot \cos^2 2\theta_2} \qquad \text{Eq. 20}$$

$$\sin i = C_L \cdot \sin \theta_2/C_T$$

Equations 19 and 20 are obtained by assuming plane instead of spherical wave reflections; therefore the values of $A_{rp}(\theta_1)$ and $A_{rs}(\theta_2)$, as calculated by using the above equations, include some error.

As shown above, by measuring or assuming the values of A_o, B_o, n, m, h, k, C_L, C_T, ρ and wave shapes of U_w and V_w, the stresses caused by the respective stress waves can be analysed. Accordingly, the stresses at any point within the rock, in the case of blasting with one free face, can be synthesized by transferring the stresses due to the three wave motions to a common coordinate system and synthesizing them with due consideration to their respective times of arrival.

3. COMPUTER PROGRAM

It is clear, from the equations shown above, that it would be very tedious to calculate the magnitude and the direction of the principal stresses induced within a rock as a function of time by using a desk calculator. Therefore these calculations were made by means of an electronic computer. This method of stress analysis described above, and the computer program used to calculate the magnitude and the direction of the principal stresses in the case of blasting with a spherical charge near a free face, were originally developed by Professor Ichiro Ito and the senior author at Kyoto University, Japan, in 1962. For the present study, the original program written for Kyoto University's computer K DC-1 was rewritten using Fortran II, to allow its use on the Department of Mines and Technical Surveys' IBM 1620. The flow chart of the program is shown in Figure 2. As shown, initialization of indices, calculation of required constants and selection of stress calculation locations all precede the stress calculations.

In the stress computations section of the program, since particle velocity and displacement wave shapes can change with distance from the shot point, the program is designed so as to select the right wave shape for the particular computation from the memory storage, where wave shape information concerning both particle velocity and displacement at different distances is stored. The selection of wave shape data is on the basis of the path distance from the shot centre to the point where the stresses are being computed. This selection is done in the DO loop where the stresses caused by IP are being computed. The computer selects wave shape data for the closest equivalent path length to that for the direct longitudinal wave, namely, the distance between 0 and point A. The stresses resulting from IP are determined at intervals of ΔT from the instant $T_{ip} = 0$. After calculating the stresses caused by IP, the stresses caused by RP are computed, using similar stored wave shape data having the closest equivalent path length to the distance between 0_1 and the point A_1. These stress components in polar coordinates with 0_1 as the origin are changed to polar stress components with the origin at 0, using the following relationships:

$$\sigma_{R\,rp} = \cos^2 \beta\, \sigma_{r\,rp} + \sin^2 \beta\, \sigma_{\theta\,rp} - 2 \sin \beta \cos \beta\, \tau_{r\theta\,rp}$$

$$\sigma_{F\,rp} = \sin^2 \beta\, \sigma_{r\,rp} + \cos^2 \beta\, \sigma_{\theta\,rp} + 2 \sin \beta \cos \beta\, \tau_{r\theta\,rp}$$

$$\sigma_{T\,rp} = \sigma_{t\,rp}$$

$$\tau_{RF\,rp} = \sin \beta \cos \beta (\sigma_{r\,rp} - \sigma_{\theta\,rp}) + (\cos^2 \beta - \sin^2 \beta)\, \tau_{r\theta\,rp}$$

$$\tau_{FT\,rp} = \tau_{TR\,rp} = 0$$

Eq. 21

START

Initialize the index.
Compute values of constants.

Select point at which stresses are to be determined. ← Loop

Arrangement for computing stresses caused by IP.

Compute $\sigma_{r\ ip}$, $\sigma_{\theta\ ip}$ $(= \sigma_{\phi\ ip})$ and store.

Print out $\sigma_{r\ ip}$, $\sigma_{\theta\ ip}$ $(= \sigma_{\phi\ ip})$.

Arrangement for computing stresses caused by RP.

Compute delay of arrival RP to IP.

Compute $\sigma_{r\ rp}$, $\sigma_{\theta\ rp}$ $(= \sigma_{\phi\ rp})$, $\tau_{r\theta\ ip}$

Transfer stresses to a common co-ordinate system.

Compute $\sigma_{r\ ip}$, $\sigma_{R\ rp}$, $\sigma_{\theta\ ip}$, $\sigma_{F\ rp}$, $\sigma_{\phi\ ip}$, $\sigma_{t\ rp}$ and store.

Modify $T_{ip} + k\Delta T$, $k=1,2,\ldots$

Modify $T_{rp} + k\Delta T$, $k=1,2,\ldots$

1

1

Arrangement for computing stresses caused by RS.

Compute delay of arrival RS to IP.

Compute $\sigma_{r\ rs}$, $\sigma_{\theta\ rs}$, $\sigma_{t\ rs}$, $\tau_{r\theta\ rs}$.

Transfer stresses to a common co-ordinate system.

Compute
$\Sigma\ \sigma_R = \sigma_{r\ ip} + \sigma_{R\ rp} + \sigma_{R\ rs}$
$\Sigma\ \sigma_F = \sigma_{\theta\ ip} + \sigma_{F\ rp} + \sigma_{F\ rs}$
$\Sigma\ \sigma_T = \sigma_{t\ ip} + \sigma_{t\ rp} + \sigma_{t\ rs}$
$\Sigma\ \tau_{RF} = \tau_{RF\ rp} + \tau_{RF\ rs}$ and store.

Compute and print out principal stresses and direction.

Determine whether principal stresses have been computed at all points required.

Modify $T_{rs} + k\Delta T$, $k=1,2,\ldots$

Modify $T_{ip} + k\Delta T$, $k = 1,2..$

Loop

Modify the index so as to change the point at which stresses will be computed.

END

Figure 2. Flow chart of computer program.

where $\beta = \theta + \theta_1$ and $\sigma_{R\,rp}$, $\sigma_{F\,rp}$, $\sigma_{T\,rp}$, $\tau_{RF\,rp}$, $\tau_{FT\,rp}$ and $\tau_{TR\,rp}$ are the stresses caused by RP with respect to polar coordinates with the origin at 0. After completion of the above calculation, the stresses caused by IP ($\sigma_{r\,rp}$, $\sigma_{\theta\,ip}$, $\sigma_{t\,ip}$) and RP ($\sigma_{R\,rp}$, $\sigma_{F\,rp}$, $\sigma_{T\,rp}$) are synthesized by considering the relative arrival times of RP to IP. Lastly, the stresses caused by RS are computed in a similar manner to that used previously to compute RP. Once again, wave shape data stored in the computer having the closest equivalent path length to rs are used, where

$$rs = r_{is} + (\text{distance between } 0_2 \text{ and A}) - r_s.$$

Conversion of the stress components due to the reflected shear from polar coordinates with origin 0_2 to polar coordinates with origin 0 is done by means of the following equations:

$$\sigma_{R\,rs} = \sigma_{r\,rs}\cos^2\gamma + \sigma_{\theta\,rs}\sin^2\gamma - 2\,\tau_{r\theta\,rs}\sin\gamma\cos\gamma$$

$$\sigma_{F\,rs} = \sigma_{r\,rs}\sin^2\gamma + \sigma_{\theta\,rs}\cos^2\gamma + 2\,\tau_{r\theta\,rs}\sin\gamma\cos\gamma$$

$$\sigma_{T\,rs} = \sigma_{t\,rs}$$

$$\tau_{RF\,rs} = (\sigma_{r\,rs} - \sigma_{\theta\,rs})\sin\gamma\cos\gamma + \tau_{r\theta\,rs}(\cos^2\gamma - \sin^2\gamma)$$

$$\tau_{FT\,rs} = \tau_{TR\,rs} = 0$$

$$\left. \right\} \quad \text{Eq. 22}$$

where $\gamma = \theta + \theta_2$ and $\sigma_{R\,rs}$, $\sigma_{F\,rs}$, $\sigma_{T\,rs}$, $\tau_{RF\,rs}$, $\tau_{FT\,rs}$ and $\tau_{TR\,rs}$ are the stresses caused by RS in the polar coordinates with origin 0. These stresses are then synthesized with the stresses caused by IP and RP, taking into account their respective arrival times, using the following equations:

$$\Sigma\,\sigma_R = \sigma_{r\,ip} + \sigma_{R\,rp} + \sigma_{R\,rs}$$

$$\Sigma\,\sigma_F = \sigma_{\theta\,ip} + \sigma_{F\,rp} + \sigma_{F\,rs}$$

$$\Sigma\,\sigma_T = \sigma_{t\,ip} + \sigma_{t\,rp} + \sigma_{t\,rs}$$

$$\Sigma\,\tau_{RF} = \tau_{RF\,rp} + \tau_{RF\,rs}$$

$$\Sigma\,\tau_{FT} = \Sigma\,\tau_{TR} = 0$$

$$\left. \right\} \quad \text{Eq. 23}$$

As is evident from the above equations, one of the three principal stresses within the rock always acts in the $\emptyset$ direction, and its magnitude is $\Sigma\sigma_T$. Therefore, the magnitudes of the two principal stresses in the $r\theta$ plane and their directions are calculated, using the following equations:

$$
\left.
\begin{aligned}
\sigma_1 &= \frac{\Sigma\sigma_R + \Sigma\sigma_F}{2} - \left[\left(\frac{\Sigma\sigma_R - \Sigma\sigma_F}{2}\right)^2 + (\Sigma\tau_{RF})^2\right]^{\frac{1}{2}} \\
\sigma_2 &= \frac{\Sigma\sigma_R + \Sigma\sigma_F}{2} + \left[\left(\frac{\Sigma\sigma_R - \Sigma\sigma_F}{2}\right)^2 + (\Sigma\tau_{RF})^2\right]^{\frac{1}{2}}
\end{aligned}
\right\} \quad \text{Eq. 24}
$$

$$
\tan 2\zeta = -\frac{2\Sigma\tau_{RF}}{\Sigma\sigma_R - \Sigma\sigma_F}
$$

After completion of stress calculations at one point, an index is modified which allows a similar computation at the next specified point. This procedure is continued until all the specified computations are completed.

4. FIELD EXPERIMENTS[7]

4.1 Test Site and Rock Properties[8]

The field experiments, designed to obtain the data required to compute the stress distribution as a function of time, were carried out at the Carol Lake, Labrador, property of the Iron Ore Company of Canada. Prior to the field experiments, seismic soundings were carried out to inspect the test site. The site selected was in a region where the major ore components were magnetite and specularite.

The physical properties of the rock were determined, using cores from the test site (8). The average specific gravity of the rock was $3.8\,\text{g/cm}^3$, with a standard deviation of $0.23\,\text{g/cm}^3$. The uniaxial compressive strength of the specimens varied from $1470\,\text{kg/cm}^2$ to $3220\,\text{kg/cm}^2$, with an average value of $2380\,\text{kg/cm}^2$ and a standard deviation of $380\,\text{kg/cm}^2$. The average value of the modulus of elasticity was found to be $8.75\times10^5\,\text{kg/cm}^2$, with a standard deviation of $0.7\times10^5\,\text{kg/cm}^2$. The static uniaxial tensile

strength was measured by the Brazilian test, and an average value of 85 kg/cm² was obtained. Since only 7 Brazilian tensile tests were carried out on the core, no standard deviation was determined. The dynamic tensile strength of the core obtained near the test site was determined using a Hopkinson-type bar test. The average dynamic tensile strength was found to be 127 kg/cm², with a standard deviation of 28 kg/cm².

4.2 Methods Used for the Field Experiments

(A) The Linear Array Experiment -

In order to obtain the necessary direct longitudinal stress wave parameters to utilize the computer program, a linear array experiment was designed. Figure 3 is an idealized sectional diagram of the linear array test site, locating the gauge and shot holes. The five gauge holes marked G in Figure 3 were drilled using an AX diamond bit. Both AX (1-7/8 in. $\emptyset$) and HM (3-7/8 in. $\emptyset$) diamond bits were used to drill the charge holes. The letters W and E on Figure 3 refer to charge holes drilled west and east of the linear array gauge holes. The bottoms of all gauge and shot holes were located in the same plane, approximately 28 ft below the ground surface. As a result, the presence of the free face had essentially no effect on the initial ground motion in the vicinity of the gauge holes resulting from the detonation of test charges. Sensing devices were installed near the bottom of the gauge holes, using a specially designed mounting system. The sensing devices were aligned with their sensitive axes paralleling the direction of the linear array. Since it was required that the path between the shot and gauge holes be unobstructed by other shot holes, initially only shot holes E_7 and W_7 were drilled. As the experiment progressed, other shot holes were drilled. The location of the bottom of each shot and gauge hole was accurately determined by survey in order to allow an exact determination of the distance between the explosive charges and the sensing devices.

(B) The Shear Array Experiment -

In order to obtain the shear wave particle velocity and displacement decay exponents for this particular rock, a shear array experiment was designed. Owing to practical difficulties, however, the original shear array layout could not be used; in its place the modified shear array shown in Figure 4 was used. In this array the AX size gauge and shot holes of the linear array experiment were used as gauge holes. A 10-ft-deep shot hole, S, was placed offset from G5 and the line of the gauge holes by 3 ft. This provided transmission paths between the shot and gauge holes which were unobstructed by other gauge holes. All the gauges were installed, using the previously mentioned mounting device, in a plane about 10 ft below the surface. In this array, the sensitive axis of the sensing devices was vertical in order to detect the ground motion resulting from a shear wave disturbance initiated at the bottom of S.
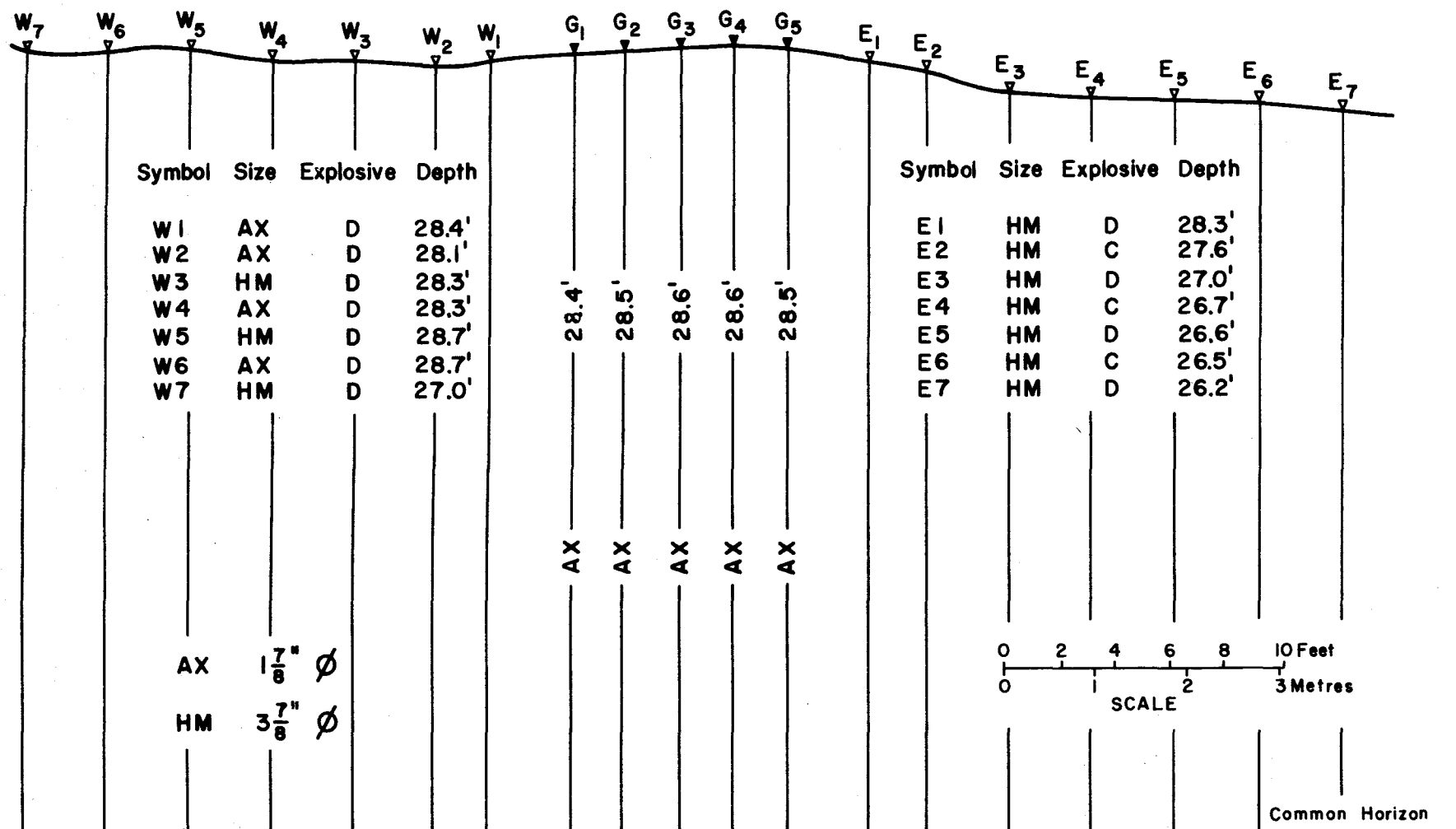
Symbol	Size	Explosive	Depth
W I	AX	D	28.4'
W 2	AX	D	28.1'
W 3	HM	D	28.3'
W 4	AX	D	28.3'
W 5	HM	D	28.7'
W 6	AX	D	28.7'
W 7	HM	D	27.0'

Symbol	Size	Explosive	Depth
E I	HM	D	28.3'
E 2	HM	C	27.6'
E 3	HM	D	27.0'
E 4	HM	C	26.7'
E 5	HM	D	26.6'
E 6	HM	C	26.5'
E 7	HM	D	26.2'

AX $1\frac{7}{8}"$ ⌀

HM $3\frac{7}{8}"$ ⌀

Figure 3. Section diagram of linear array at test site, locating
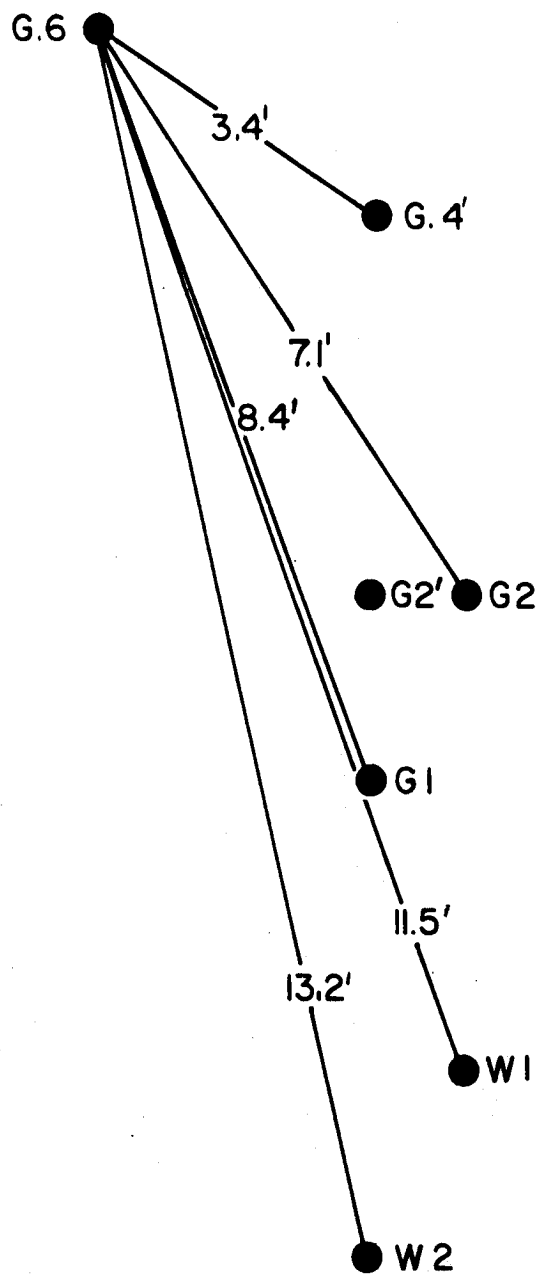gauge holes (G) and shot holes (E and W).

- 14 -

Figure 4. Plan diagram of shear array.

4.3 Explosives and Shear Wave Generator

Two explosives were selected for the field experiments. One of the explosives was Geogel 60%, a straight plastic gelatin dynamite having excellent water resistance properties and a specific gravity in cartridge form of 1.5. Geogel 60% has an unconfined detonation velocity of 6,200 m/sec and a detonation pressure, as determined by the aquarium technique, of 170 KB. The power of the explosive is equivalent to 0.96 g TNT/g. The second explosive used was Cilgel "B" 70%, a plastic ammonia semi-gelatin which is water resistant. It has an unconfined detonation velocity of 4,000 m/sec and an experimentally determined detonation pressure of 87 KB. It is equivalent in power to 1.12 g TNT/g.

In the field experiments, all explosive charges used had the same length-to-diameter ratio of 3 to 1. To obtain these ratios the charge weights shown in Table 1 were used in the various diameter holes.

TABLE 1

Charge Weights of the Explosives

	Geogel 60%	Cilgel B 70%
AX size holes	425 g	--
HM size holes	3,400 g	2,950 g

The contained detonation velocity of each explosive charge was measured with a resistance probe. Average values for Geogel 60% and Cilgel B 70% in the HM size holes were 6,300 m/sec and 4,100 m/sec respectively.

In the shear wave experiment, two methods involving the use of a detonator and a lead bullet were used to generate a shear wave at the bottom of the shot hole. Figure 5 is a section diagram of the detonator mount. This unit, attached to a 10-ft length of aluminum pipe, was placed at the bottom of the shot hole with the detonator in contact with the bottom of the hole. Figure 6 is a photograph of the gun constructed to fire a lead bullet down a 10-ft length of pipe at the bottom of the shot hole. The calibre of the gun is 0.45 in., and the lead slug with a mass of 16.5 g attains a muzzle velocity of 260 m/sec.

4.4 Sensing Devices and Mounting Assemblies

Accelerometers were used as sensing devices in both types of array experiment. The various parameters required from the field experiments were determined from recorded acceleration records. Endevco 2231 accelerometers were used in the linear array, and Clevite 25D21

1/2 NPT To Couple To
1"Aluminum Conduit

Detonator Wire
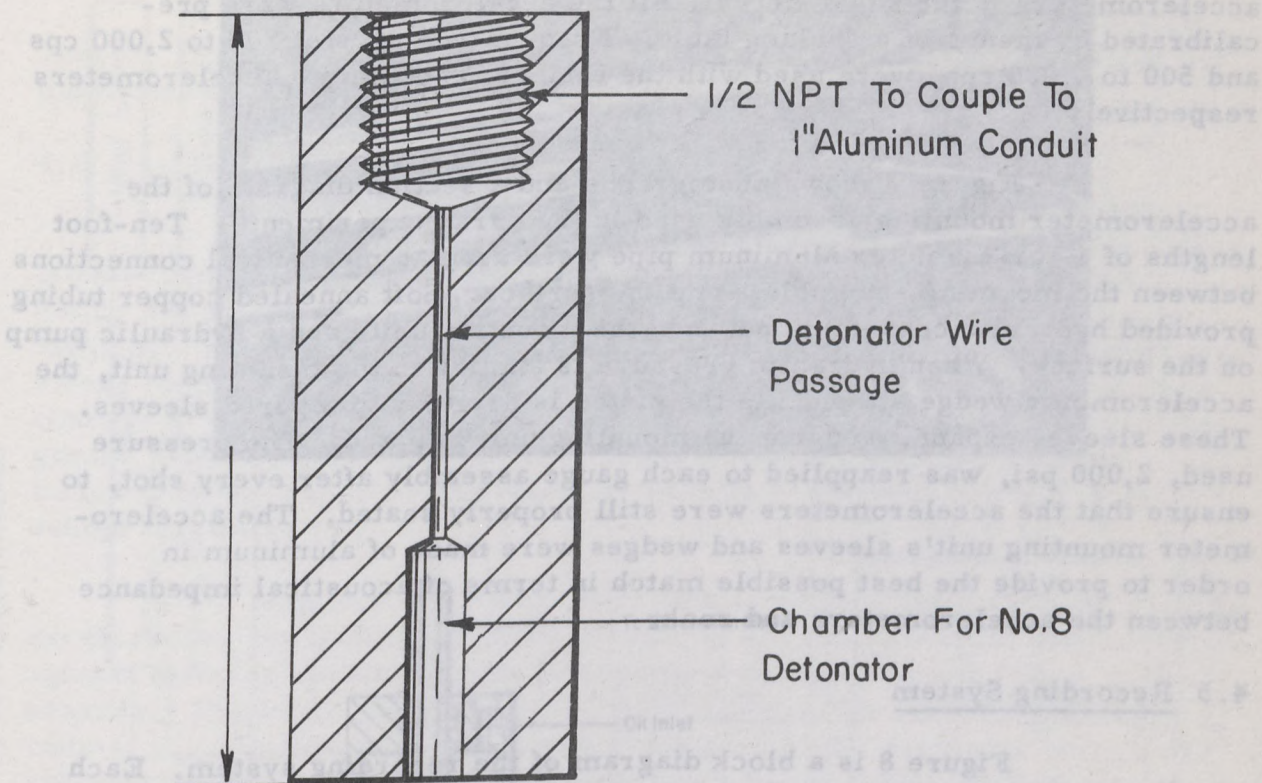Passage

Chamber For No.8
Detonator

Figure 5. Section diagram of detonator mount used for
shear wave generation.

Figure 6. Photograph of gun used for shear wave generation.

accelerometers in the shear array. All the accelerometers were pre-calibrated by means of a shaking table. Frequency ranges of 200 to 2,000 cps and 500 to 9,000 cps were used with the Endevco and Clevite accelerometers respectively.

Figure 7 shows photographs and a section diagram of the accelerometer mounting assembly used in the array experiments. Ten-foot lengths of 1-in.-diameter aluminum pipe were used as mechanical connections between the mounting assemblies and the surface. Soft annealed copper tubing provided hydraulic connection between the mounting units and a hydraulic pump on the surface. When hydraulic pressure is applied to the mounting unit, the accelerometer wedge attached to the piston is driven into tapered sleeves. These sleeves expand, wedging the mounting unit in place. The pressure used, 2,000 psi, was reapplied to each gauge assembly after every shot, to ensure that the accelerometers were still properly seated. The accelero-meter mounting unit's sleeves and wedges were made of aluminum in order to provide the best possible match in terms of acoustical impedance between the accelerometers and rock.

4.5 Recording System

Figure 8 is a block diagram of the recording system. Each accelerometer (Acc) was connected by the shortest possible length of cable to a cathode follower (CF), the latter unit mounted in a waterproof box. These cathode followers were connected by 250 ft of co-axial cable to the amplifiers (Amp) in the instrument shack. The output of the five accelero-meters, the firing pulse and the trigger pulse were recorded, using a seven-channel FM tape recorder (CEC, VR-3300, 0-20 kc/sec bandwidth). The switching unit shown in Figure 8 was used, at the completion of a test shot recording, to transfer all seven inputs of the tape recorder to an oscillator which provided, for the purpose of calibration, a known amplitude, known frequency sinewave voltage to all seven channels. The paper oscillograph was used only as a monitoring unit; possessing only a 0-5 kc/sec bandwidth, the galvanometers were incapable of reproducing with fidelity the output of the tape channels.

A dual beam oscilloscope was used for information playback. The trigger pulse recorded on one of the channels of the tape recorder was used to provide, on playback, an external trigger to the oscilloscope. On playback the outputs of the accelerometers were analysed one at a time. In order to produce a record of acceleration and particle velocity, the output from the tape recorder was applied concurrently to one channel of the dual beam oscilloscope (Channel A) and to an operational amplifier functioning as an integrator. The output of the operational amplifier, which was a voltage proportional to particle velocity, was applied to the remaining oscilloscope channel (Channel B). In subsequent returns of the tapes, by double integration, particle displacement records were produced.

To Extension Rods

Oil Inlet

Oil Chamber

O Ring Seal

Piston

Tapered Sleeves

Accelerometer Wedge
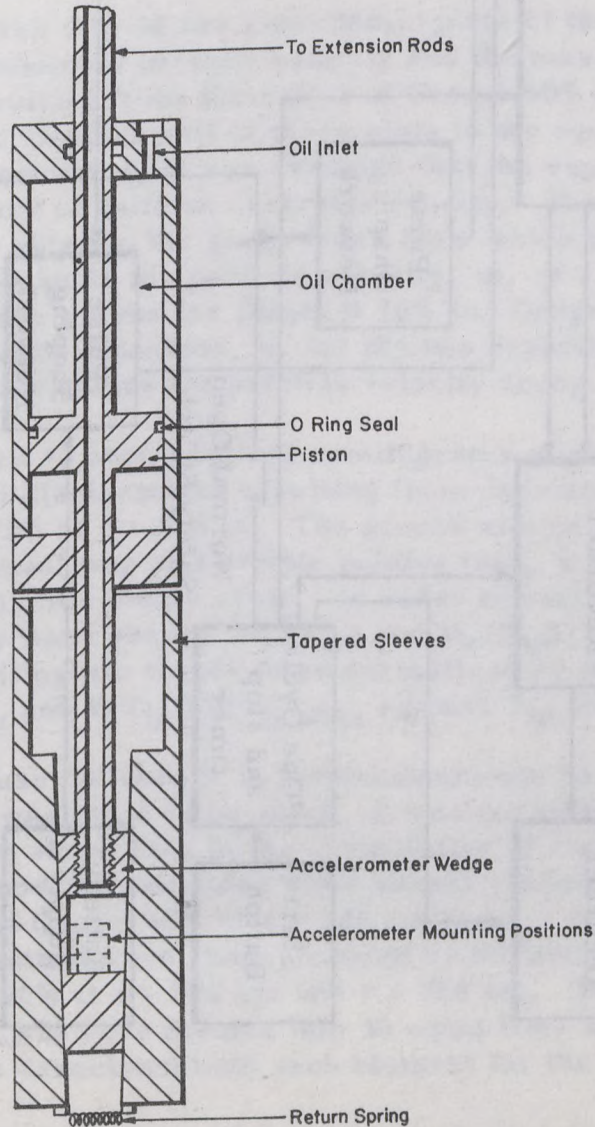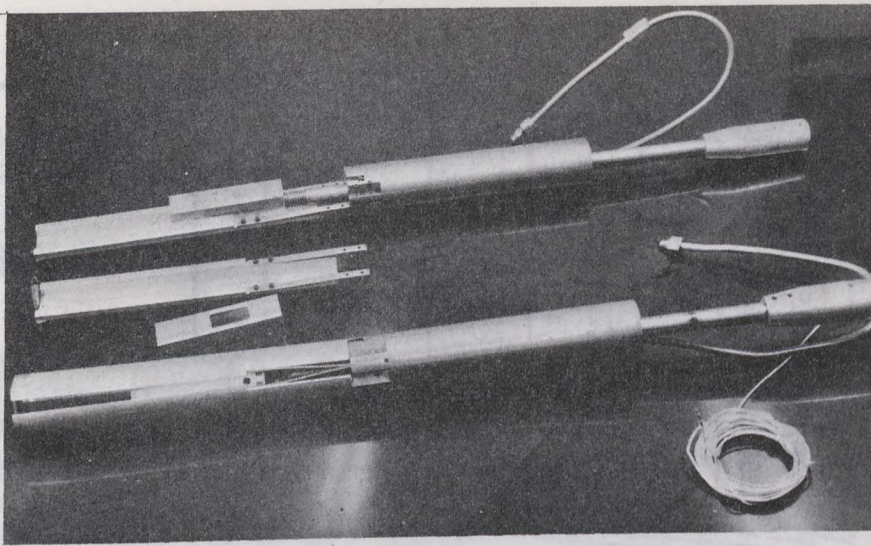
Accelerometer Mounting Positions

Return Spring

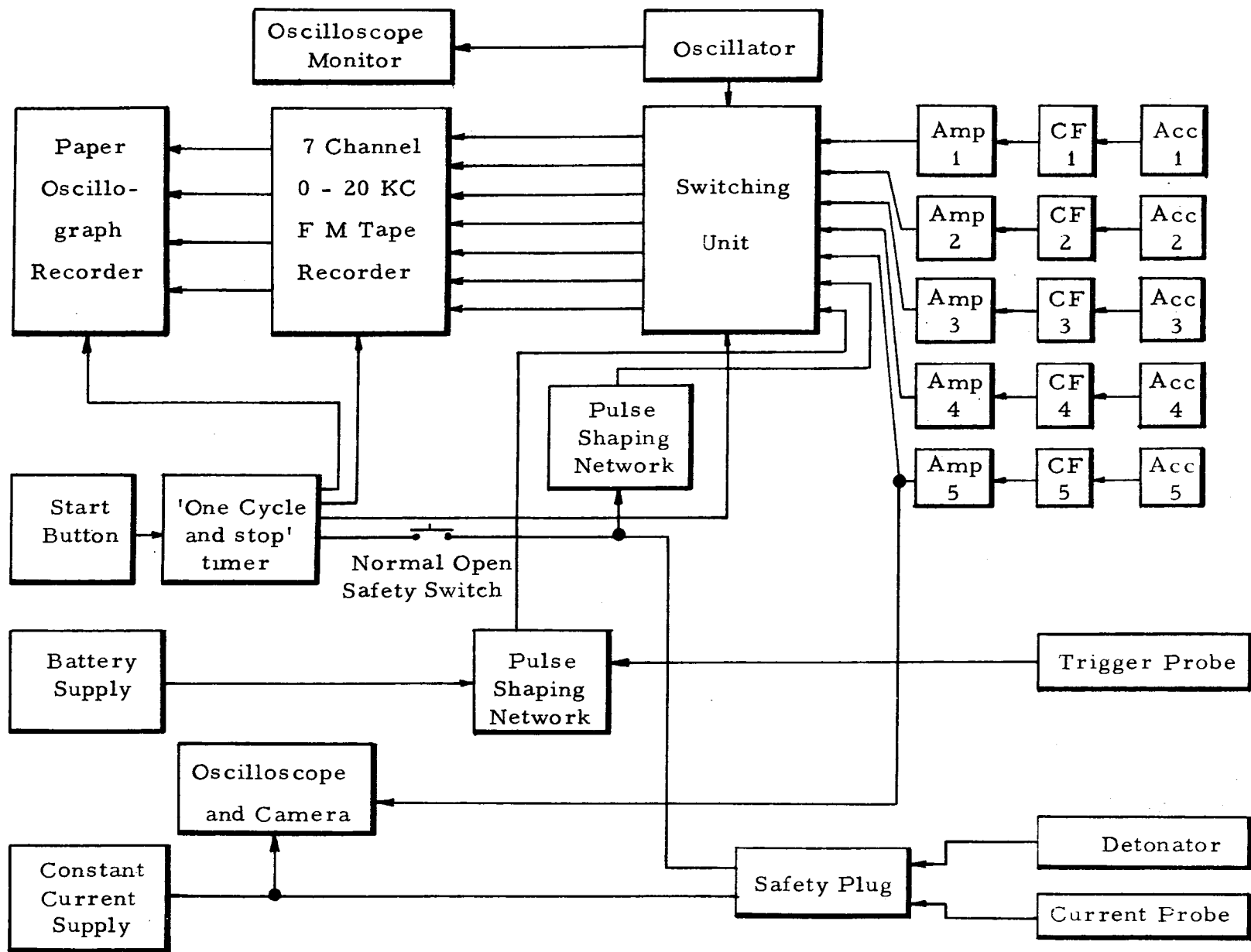Figure 7. Photograph and section diagram of accelerometer mount assembly.

Figure 8. Block diagram of recording system.

The above procedure, which was applied to accelerometer records from both the linear and shear arrays, supplied sufficient data to determine all required parameters.

4.6 Results of the Field Experiments

The longitudinal wave velocity in the test site was determined from acceleration records for gauge holes G1 and G5. This was done by noting the relative arrival times at these two points, and the path lengths involved. An average velocity of 6,400 m/sec was determined. Ultimately, stress analyses were limited to 3,400 g charges of Geogel 60% and 2,950 g charges of Cilgel B 70%. Therefore, only field results associated with the ground motion resulting from these two particular charge weights are included in this report. The complete results of the field trials are presented elsewhere (7).

Figures 9 to 14 are logarithmic plots of the maximum particle acceleration, the maximum particle velocity and the maximum displacement against distance resulting from detonation of Geogel 60% and Cilgel B 70% charges. The basic distance unit in these plots is the equivalent charge radius, r_c. To determine r_c it was assumed that the explosive charge was spherical in shape and of uniform cartridge density. The small numbers 1 to 5 on the graphs refer to the gauge holes from which the data were obtained. Decay exponents for particle velocity, m, of 1.3 and 1.4 were determined from these graphs for Cilgel B 70% and Geogel 60%, respectively. The displacement decay exponents, n, for the two explosives were numerically equal to their exponent values for particle velocity decay.

Figure 15 shows typical oscillograms of particle acceleration, particle velocity and displacement resulting from detonation of a 2,950 g charge of Cilgel B 70% at r = 5.8 m. The ground motion observed in the linear array experiment was of a simple pulsive type, with particle velocity consisting essentially of a single cycle. In order to establish displacement and particle velocity wave shapes ($U_w(T_{ip})$ and $V_w(T_{ip})$) for use in the computer program, oscillogram traces were normalized by plotting the values of $U(T_{ip})/U(T_{ip})_{max}$ and $V(T_{ip})/V(T_{ip})_{max}$ against T_{ip} and smoothed by eye.

Because the change in displacement and particle velocity wave shape with distance was found to be small, it was considered sufficient to use only two sets of wave shape data in the computation of stress distribution. Figures 16 and 17 show the smoothed wave shapes caused by the detonation of 3,400 g charges of Geogel 60% at r = 300 cm and r = 400 cm. Figures 18 and 19 show the smoothed wave shapes caused by the detonation of 2,950 g charges of Cilgel B 70% at r = 200 cm and r = 350 cm. The normalized wave shapes $U_w(T)$ and $V_w(T)$ were divided into 30 equal time elements and a numerical value was associated with each element for the purpose of stress computation.
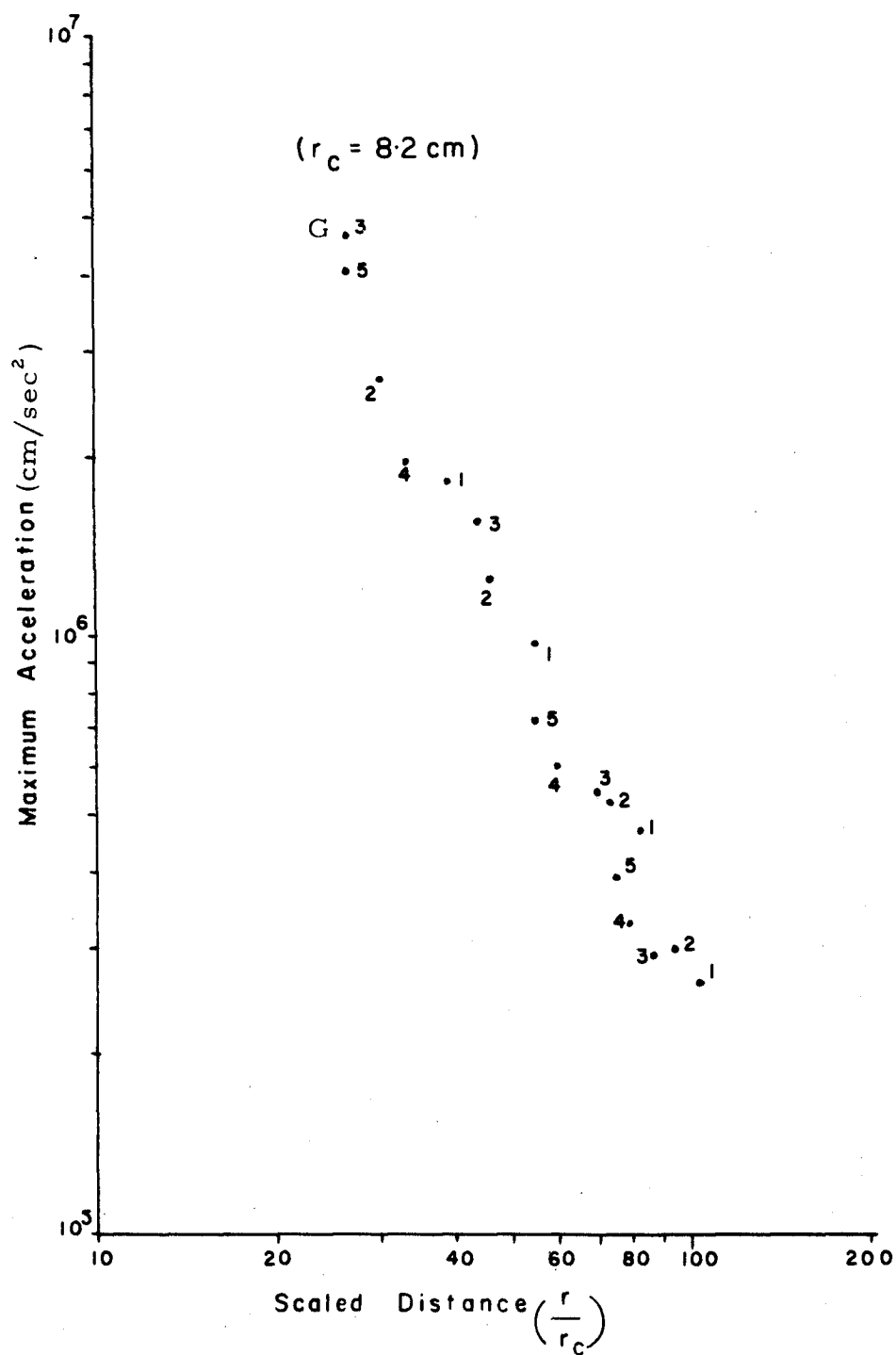
Figure 9. Maximum acceleration resulting from detonation of a 3,400 g charge of Geogel 60% vs. scaled distance (r_c = 8.2 cm), for east side HM shot holes.

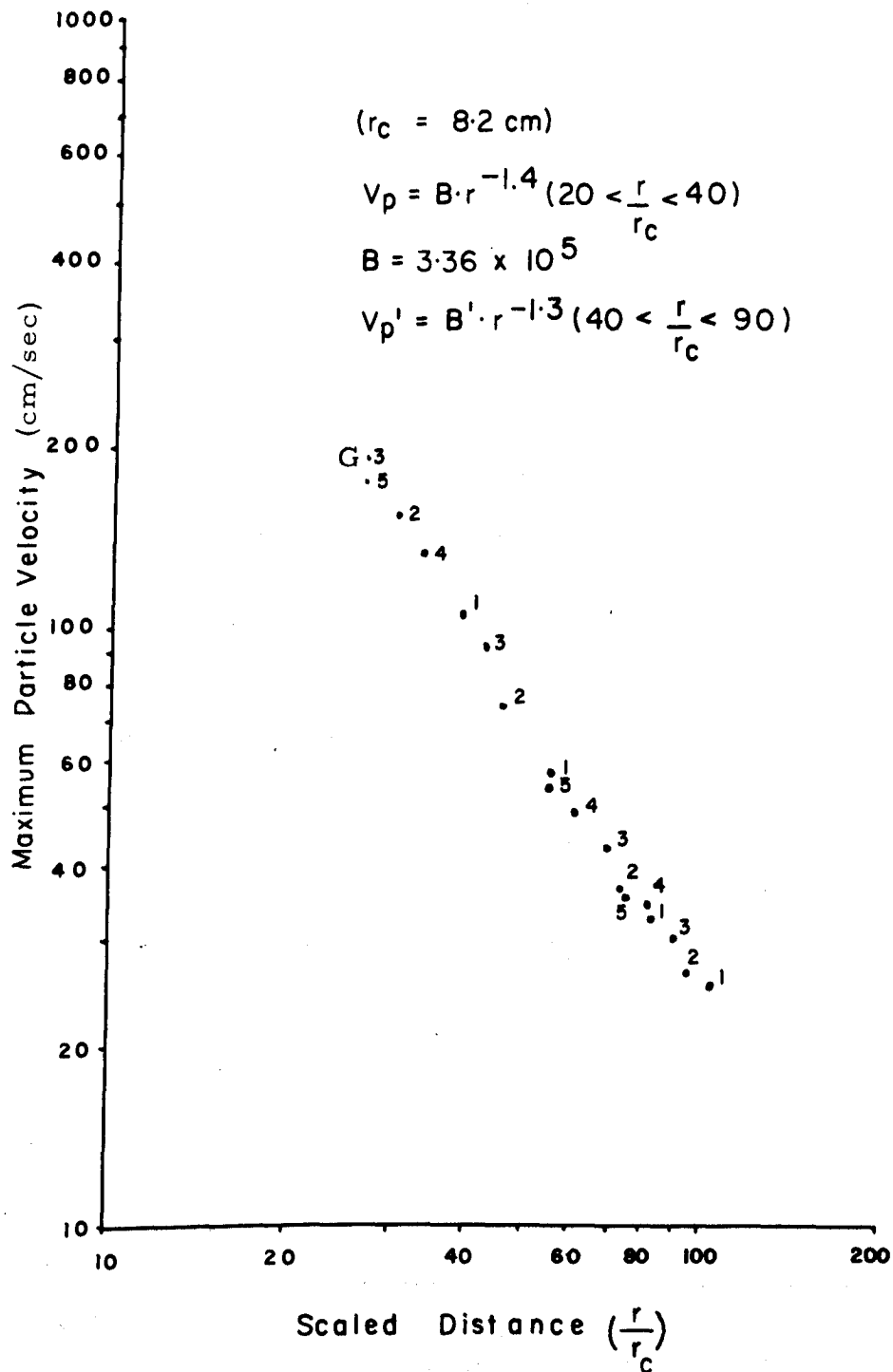Figure 10.   Maximum particle velocity by 3,400 g Geogel 60% vs. scaled distance (r_c = 8.2 cm), for east side HM shot holes.
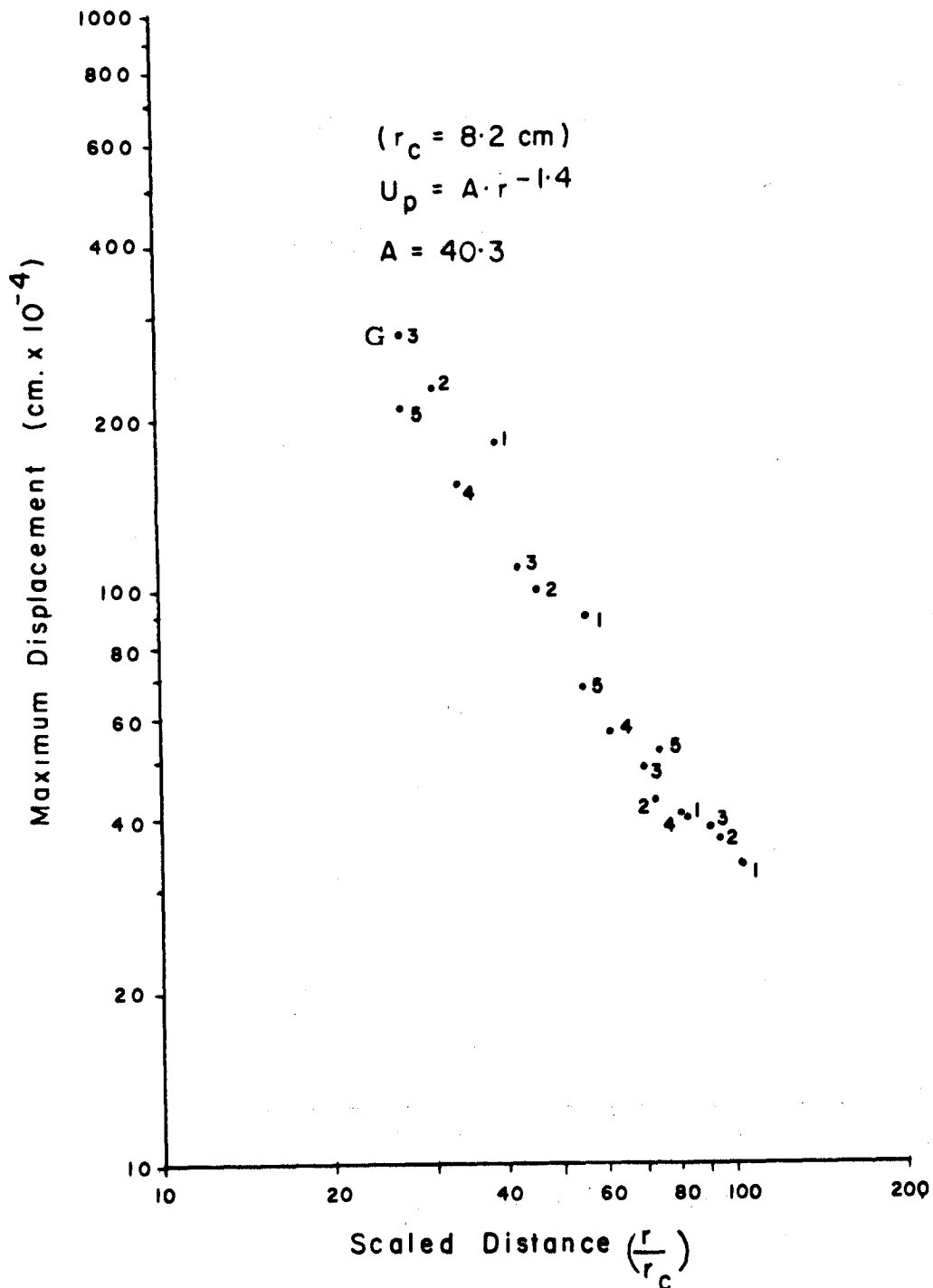
Figure 11. Maximum displacement by 3, 400 g Geogel 60% vs. scaled distance (r_c = 8.2 cm), for east side HM shot holes.
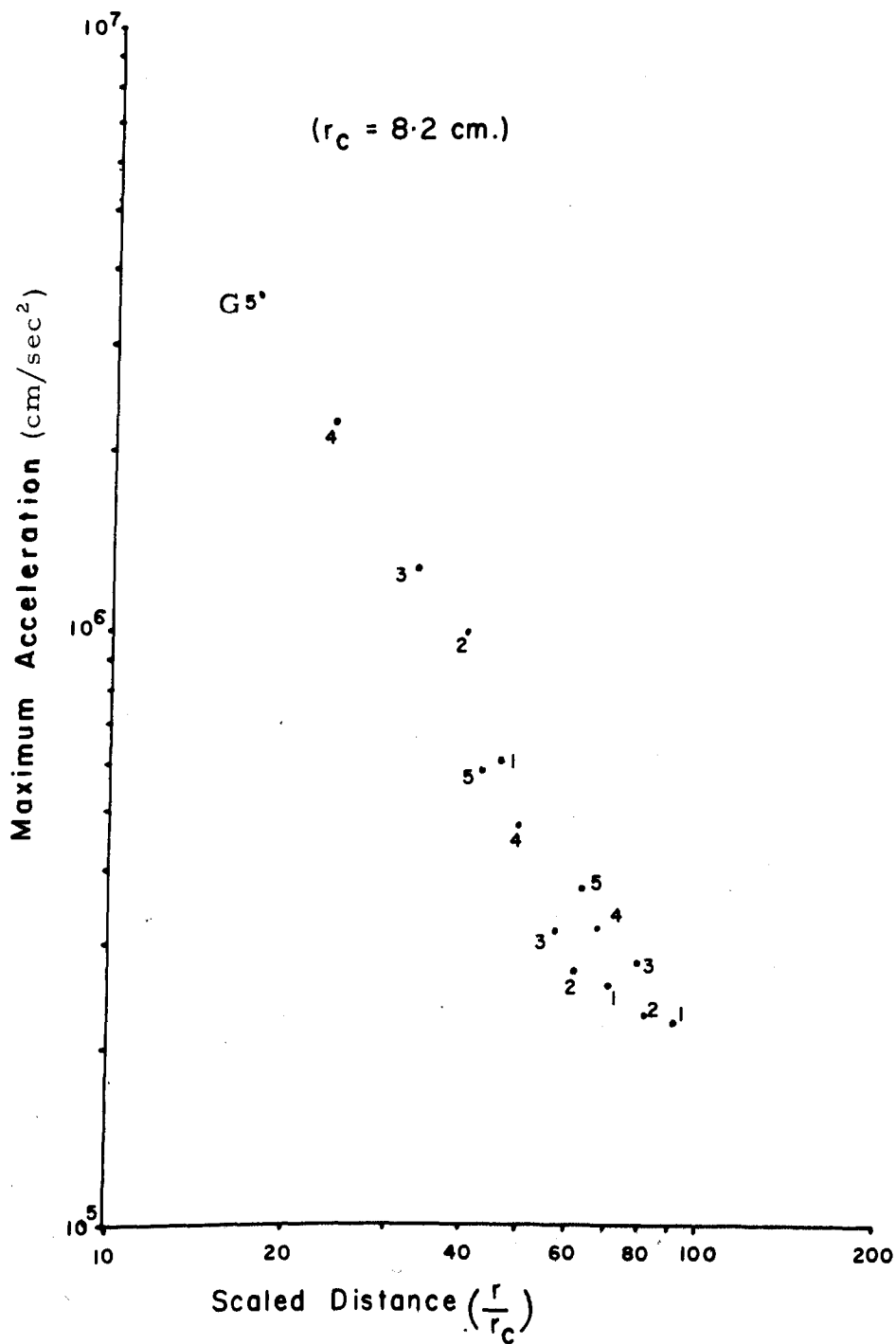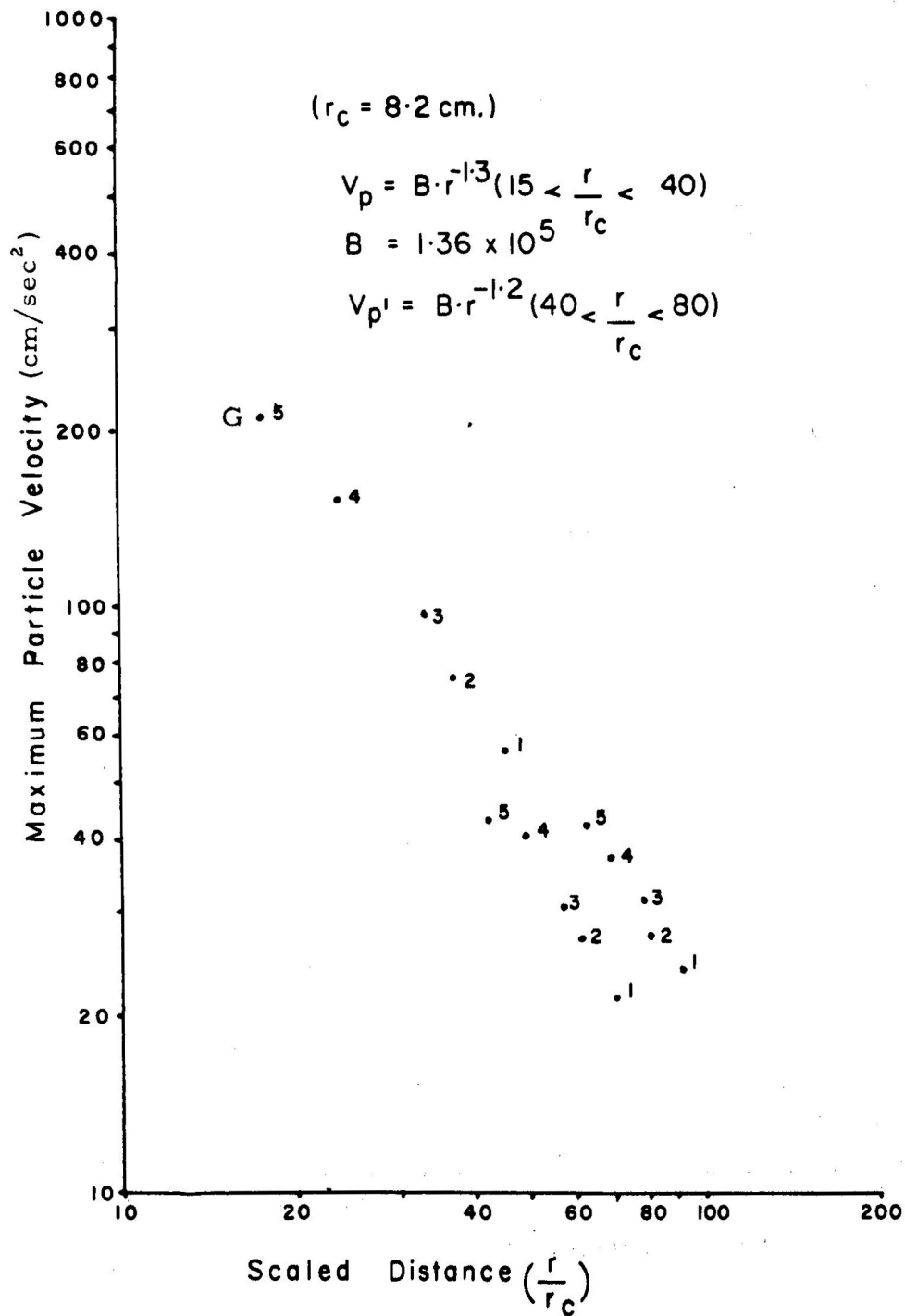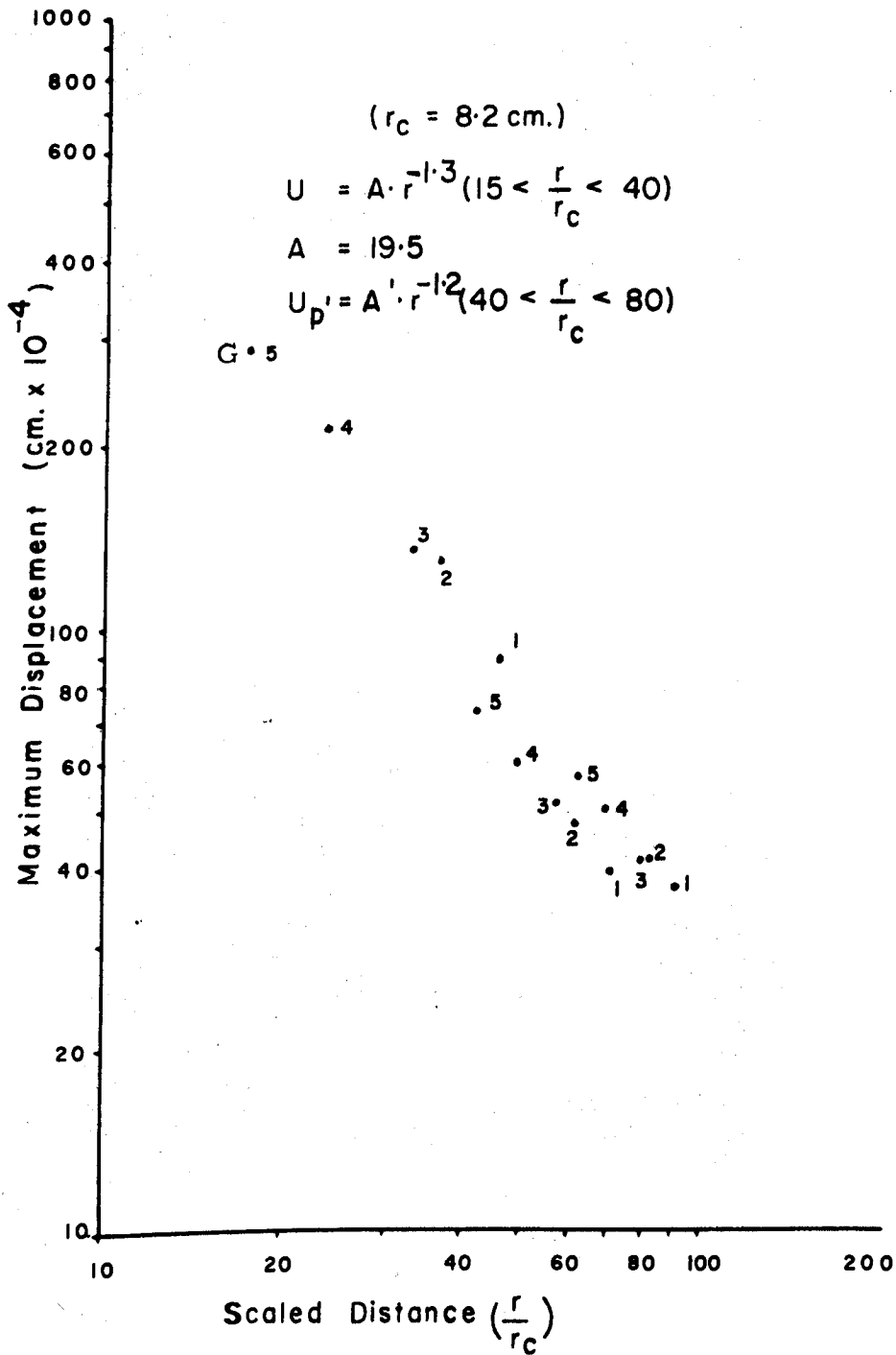
Figure 12. Maximum acceleration by 2,950 g Cilgel B 70% vs. scaled distance (r_c = 8.2 cm), for east side HM shot holes.

Figure 13. Maximum particle velocity by 2,950 g Cilgel B 70% vs. scaled distance (r_c = 8.2 cm), for east side HM shot holes.
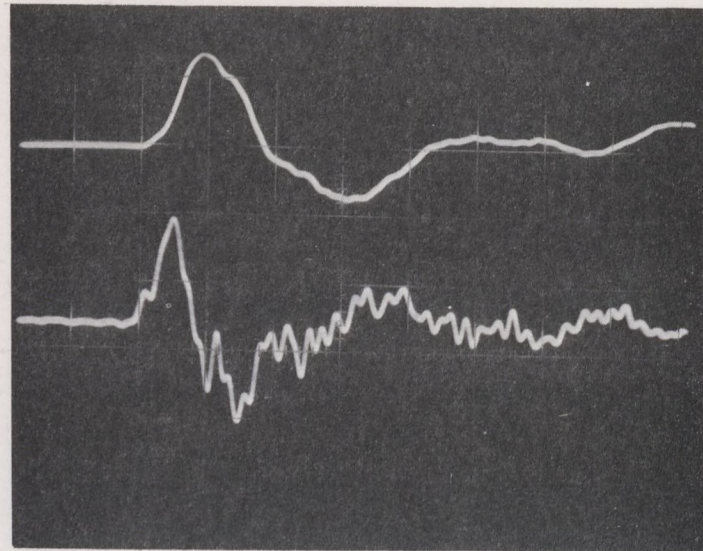
Figure 14. Maximum displacement by 2, 950 g Cilgel B 70% vs. scaled distance (r_c = 8.2 cm), for east side HM shot holes.
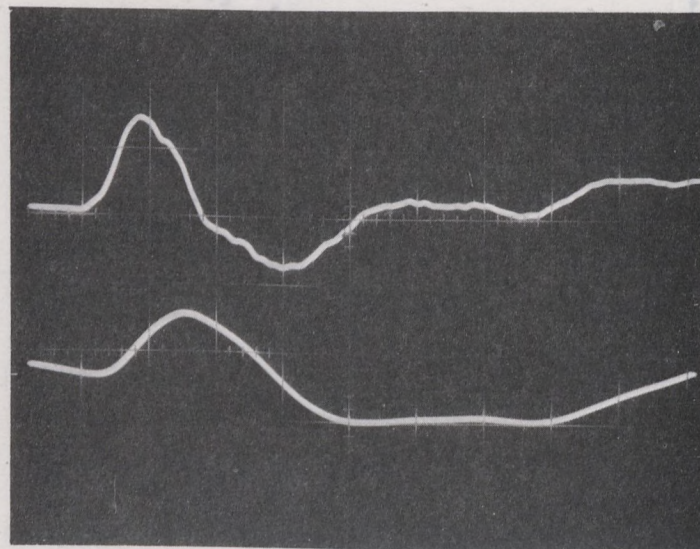
Upper beam : Particle velocity

Lower beam : Particle acceleration

Time scale

⊢——⊣
0.2ms

Upper beam : Particle velocity

Lower beam : Displacement

Time scale

⊢——⊣
0.2ms

Figure 15. Examples of oscillogram resulting from detonation of
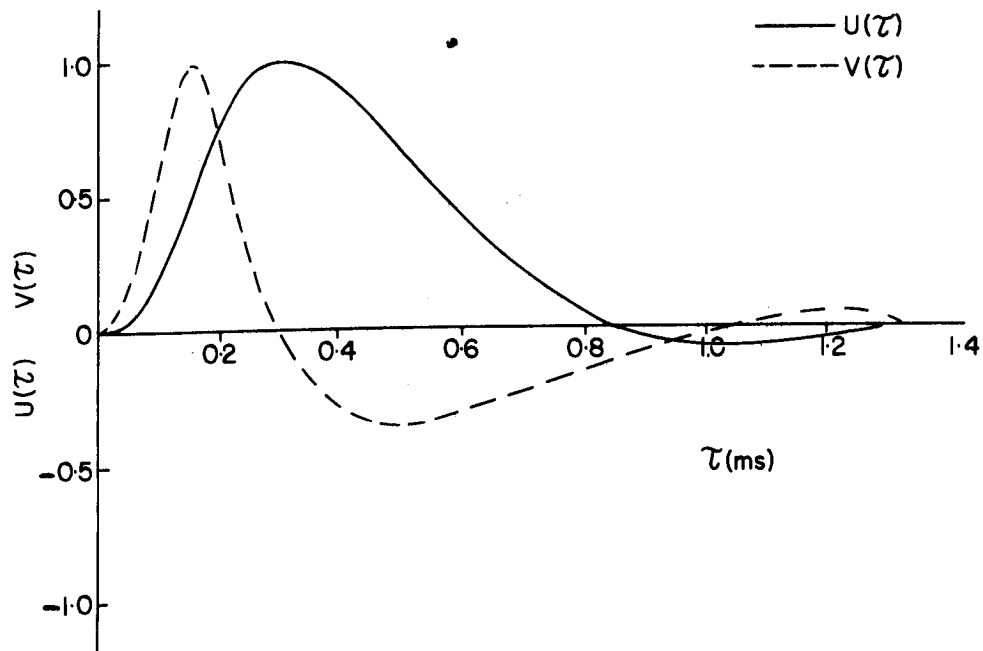2,950 g charges of Cilgel 70% at r = 5.8 m.

Figure 16.   Smoothed wave shapes resulting from detonation
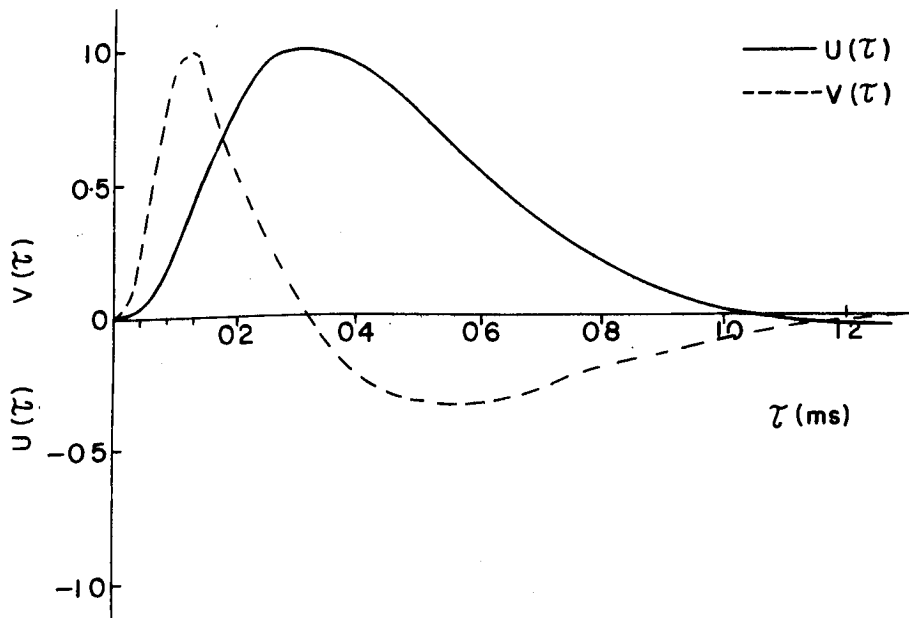of 3,400 g charges of Geogel 60% at r = 300 cm.

Figure 17.   Smoothed wave shapes resulting from detonation
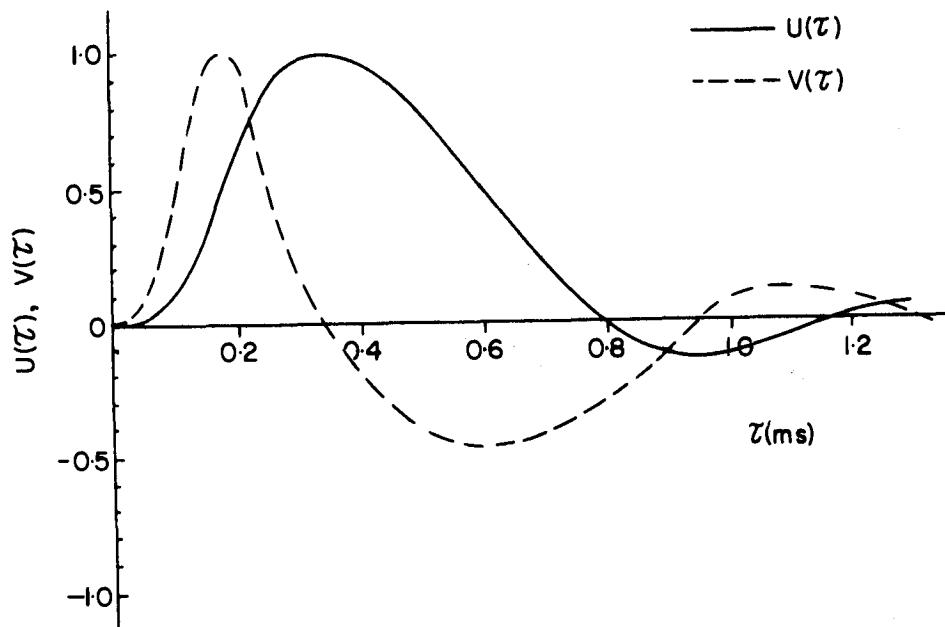of 3,400 g charges of Geogel 60% at r = 400 cm.

Figure 18. Smoothed wave shapes resulting from detonation
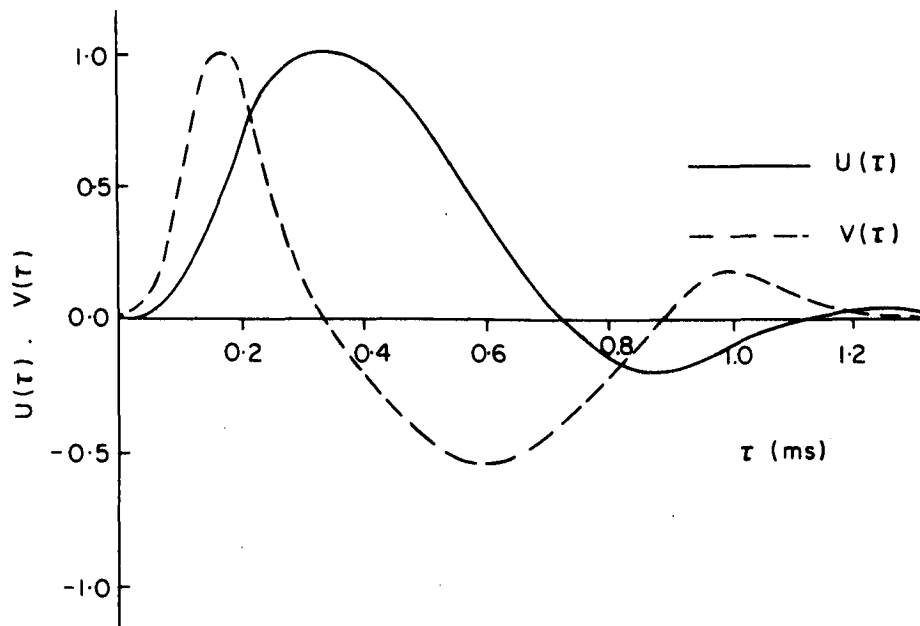of 2,950 g cartridge of Cilgel B 70% at r = 200 cm.

Figure 19. Smoothed wave shapes resulting from detonation
of 2,950 g cartridge of Cilgel B 70% at r = 350 cm.

The shear wave velocity in the test site area was determined, using records from gauge holes W_1 and W_2 and the same procedures as used in the determination of a dilatational wave velocity. The average shear wave velocity was found to be 3,420 m/sec. As mentioned before, the shear array layout used in this experiment was not ideal and as a result the data obtained were limited. Only two of the gauges functioned properly; it was found extremely difficult, with records from the other gauges, to separate the shear wave from the tail of the longitudinal wave and reflected waves from local discontinuities. According to the theory of elasticity, a power law relationship exists between the amplitude at peak displacement and distance, and the amplitude of peak particle velocity and distance. Therefore the maximum particle velocities caused by the shear waves at the two operational gauges were plotted on a log-log graph, as shown in Figure 20. Since the amplitude of maximum displacement could not be obtained from the shear array records, it was assumed that displacement and particle velocity had identical decay exponents. There was some justification in assuming equal attenuation constants for particle velocity and displacement, for the change in the duration of the first pulse of particle velocity with distance was found to be very small. Based on the above results, a value of 1.0 was determined as the value of h and k.

The values of constants used in the calculation are shown in Table 2.

TABLE 2

Values of Constants for Stress Computation

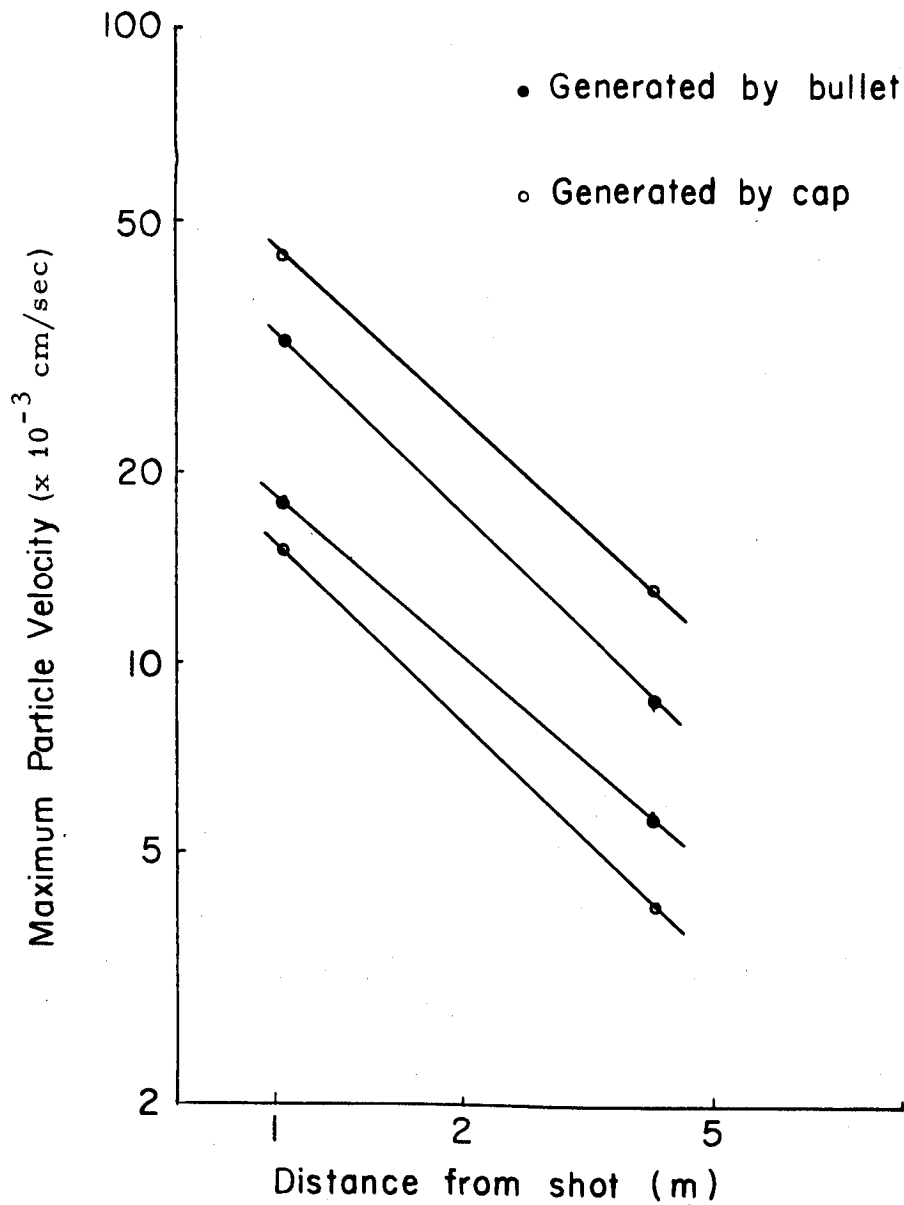| Explosive	3,400 g Geogel 60%	2,950 g Cilgel B 70%
C_L (m/sec)	6,400	6,400
C_T (m/sec)	3,420	3,420
ρ (g/cm^3)	3.6	3.6
A_o (cm)	40.3	19.5
B_o (cm/sec)	3.36×10^5	1.36×10^5
n	1.4	1.3
m	1.4	1.3
h	1.0	1.0
k	1.0	1.0

Figure 20. Logarithmic plot of maximum shear wave particle velocity vs. distance from shot point.

The elastic constants of this rock, shown below, were calculated from the values of C_L, C_T and ρ:

Lame's constants λ = 6.25×10^{11} dyne/cm^2

and μ = 4.15×10^{11} dyne/cm^2,

Young's modulus E = 10.6×10^{11} dyne/cm^2 = 1.1×10^6 kg/cm^2,

Poisson's ratio ν = 0.30.

The value of Poisson's ratio calculated in this manner agrees with that obtained from static tests.

5. DISCUSSION OF RESULTS

5.1 Results of Numerical Calculation of Displacement Based on the Theory of Elasticity [10, 11]

For the purpose of comparison with displacements realized from the field experiments, the displacement generated within a perfectly elastic infinite medium by a pressure pulse imposed on a spherical shell of radius a was calculated by using the equation derived from the wave equation for a perfect elastic medium, that is:

$$\frac{\partial^2 \overline{\phi}}{\partial t^2} = C_L^2 \, \nabla^2 \overline{\phi}, \qquad \text{Eq.25}$$

where $\overline{\phi}$ is a stress potential.

The pressure pulse considered at r = a was as follows:

$$P(t) = P_o \, N\left(e^{-\omega t/\sqrt{2}} - e^{-\sqrt{2}\,\omega t}\right),$$

$$\omega = 2\sqrt{2} \; C_L/3a, \qquad \text{Eq.26}$$

where P_o = peak pressure and N = a constant.

The displacements at r = a, 1.5a, 2a, 3a, 5a and r→∞ produced by the above pressure pulse are shown in Figure 21. The logarithmic plot of maximum displacement against distance is shown in Figure 22, where the decay exponent is initially 1.6 at r = a and decreases with increasing distance, finally reaching the value of 1.0. The decay exponent at r = 3a is already 1.17; therefore, in an elastic medium the change in the value of the decay exponent beyond 3a is small in comparison with the change in the value in the region r < 3a. Furthermore, as shown in Figure 21, the duration of the initial displacement pulse decreases with increase of distance and approaches asymptotically the value of $\omega t = 0.84\pi$. The change in duration beyond r = 3a is very small.

The changes in the decay exponent and the duration of first pulse with distance in the equivalent region where the field experiment was performed were found to be very small. Comparison of the results of the above numerical calculation with the results of the field experiments indicates that the rock at the site is fairly elastic. Since measurements were made in a region where r > 3a (that is, r > 1.4 m for Cilgel B 70% and r > 2.2 m for Geogel 60%), the decay exponents n and m can be expected to increase with decreasing distance.

5.2 Stress Wave Projected from the Explosion

When a longitudinal wave diverges from a shot point, the displacement and the particle velocity decay respectively in inverse proportion to the nth and m^{th} powers of distance, as shown in Equation 17. Therefore, the quantities $U_w(T_{ip}) \cdot dU_p(r)/dr$ and $U(r, T_{ip})/r$ in Equation 10 both decay in inverse proportion to the $(n + 1)^{th}$ power of r, and the quantity $V(r, T_{ip})/C_L$ in inverse proportion to the mth power of r. Since in the present case, from Figures 10, 11, 13 and 14, the value of n is equal to m, the former two quantities decay with distance from the charge centre at a higher rate than the latter quantity. Let r_b denote the distance from the shot centre to the point where the maximum absolute value of $U_w(T_{ip})dU_p(r)/dr$ is equal to that of $V(r, T_{ip})/C_L$. Then, as the radial stress $\sigma_{r\,ip}$ is chiefly dependent on the radial strain $U_w(T_{ip}) \cdot dU_p(r)/dr - V(r, T_{ip})/C_L$, the decay exponent of radial stress within the range of r < r_b increases with decrease of r and approaches the value (n + 1). On the other hand, within the range of r > r_b, the decay exponent decreases with increase of r and approaches the value of m.

Since the tangential stresses $\sigma_{\theta\,ip} = \sigma_{t\,ip}$ are mainly dependent on tangential strain $U(r, T_{ip})/r$, the decay exponents of the tangential stresses are nearly equal to (n + 1) in the vicinity of an explosion. With distance, however, the decay exponents of these stresses approach m; by substituting Equation 17 into Equation 10, referring to Equation 11 and putting r = ∞ and $\lambda = \mu$, the following relations are obtained for radial and tangential stresses at large distances from the shot centre:
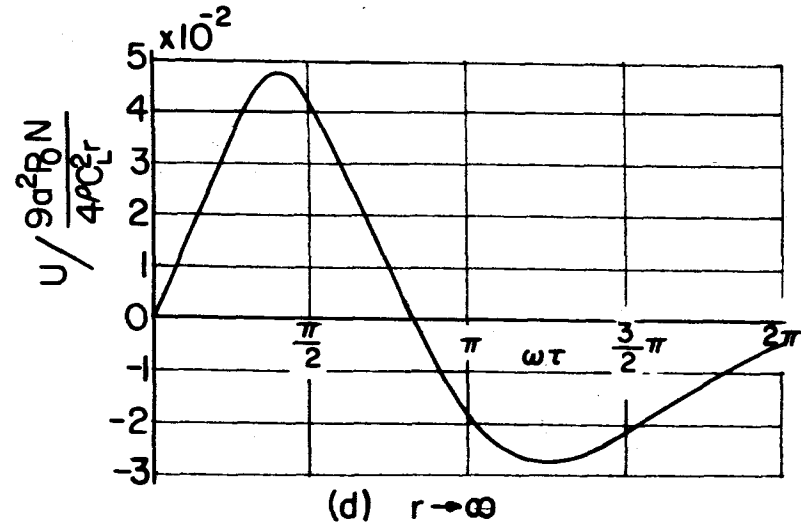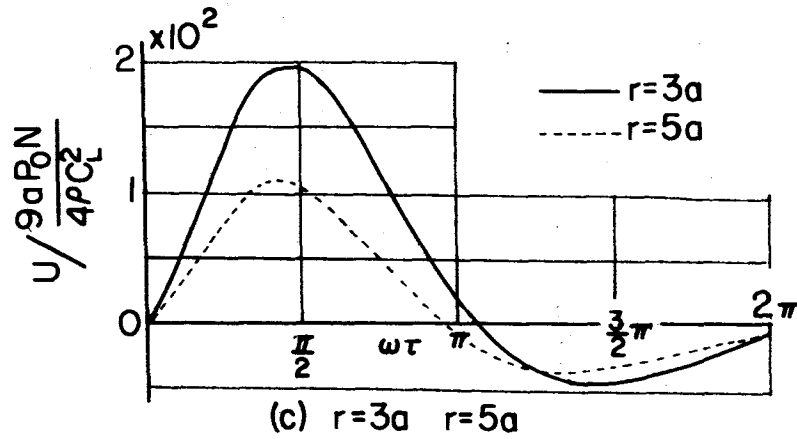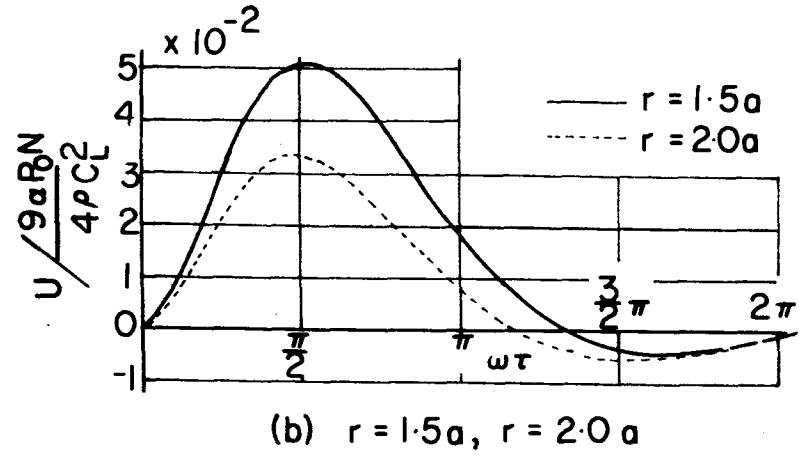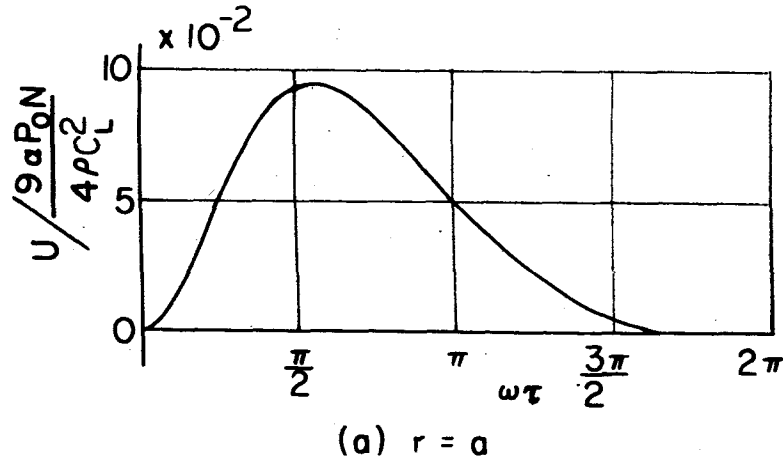
Figure 21. Displacement resulting from the application of a pressure pulse of the form $P(t) = P_0 N \left(e^{-\frac{\omega t}{\sqrt{2}}} - e^{-\sqrt{2}\omega t} \right)$ to a spherical cavity of radius $r = a$, in a homogeneous elastic medium.
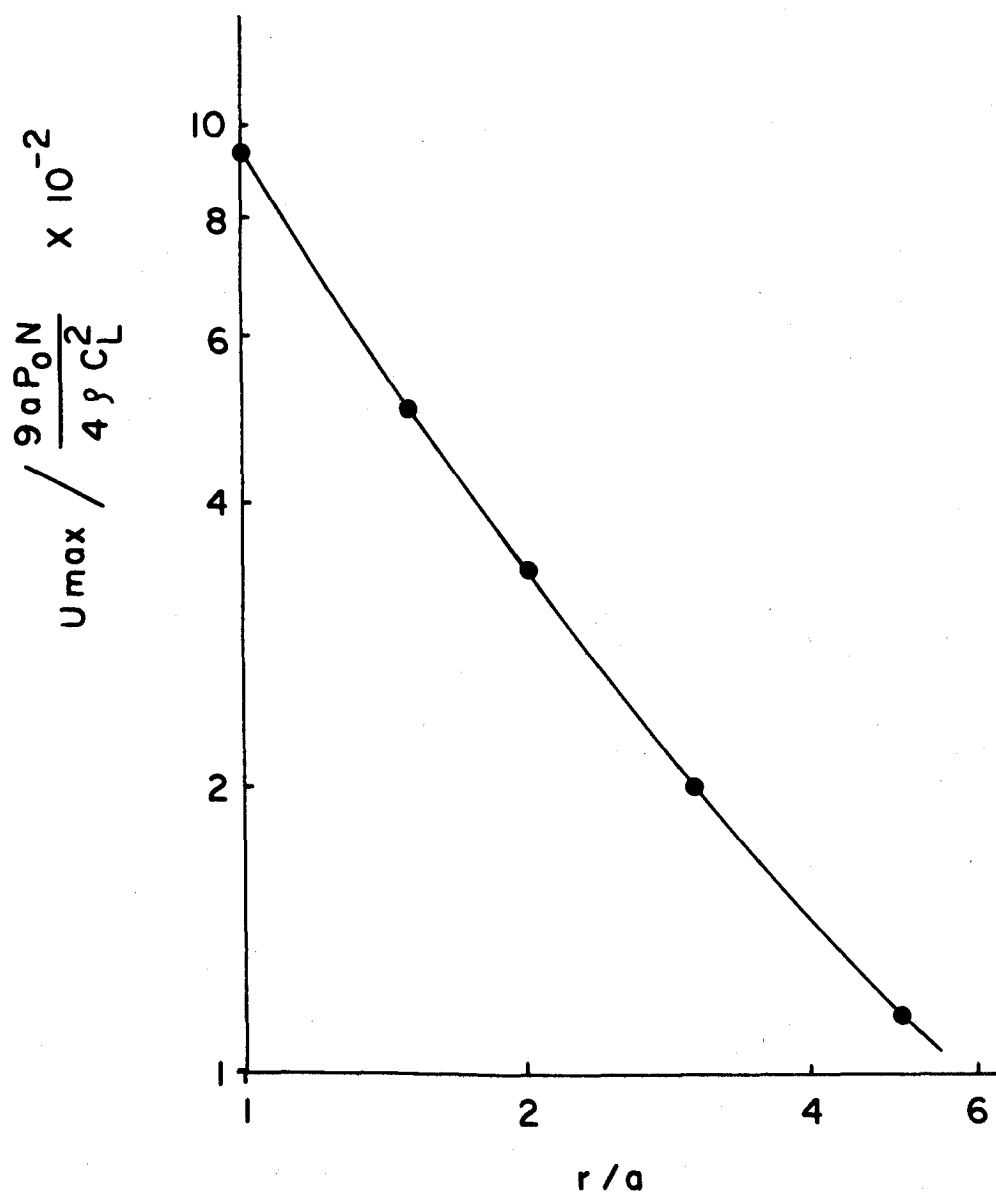
Figure 22. Attenuation of maximum displacement with distance, for the
case of a perfect elastic body.

$$\sigma_r = -\rho \, C_L \, V(r, T_{ip})$$

$$\sigma_\theta = \sigma_\phi = -\rho \, C_L \, V(r, T_{ip})/3$$

Eq. 27

Equation 27 shows that the wave shape and the attenuation of both radial stress and tangential stresses at a point far from the explosion are the same as those of the particle velocity. However, in the vicinity of the explosive charge, where the stresses depend chiefly on the quantities $U_w(T_{ip}).dU_p(r)/dr$ and $U(r, T_{ip})/r$, the wave shapes of the stresses are similar to those of displacement. Therefore, the radial stress wave shape changes from that of the displacement to that of the particle velocity near $r \doteq r_b$; the duration of the first compressive radial stress pulse decreases with increase in distance, and this change is particularly evident in the vicinity of $r = r_b$.

The stresses projected by the detonation of 3,400 g charges of Geogel 60% and 2,950 g charges of Cilgel B 70% were calculated by using Equation 10 and the data shown in Table 2 and Figures 16 to 19.

Logarithmic plots of the maximum values of radial stress $\sigma_{r\,ip}$ and tangential stresses $\sigma_{\theta\,ip}$ (= $\sigma_{t\,ip}$) against distance for both explosives are shown in Figures 23 and 24. Also, the changes in amplitude of $\sigma_{r\,ip}$ and $\sigma_{\theta\,ip}$ (= $\sigma_{\phi\,ip}$) with time are shown in Figure 25 for various distances from a 3,400 g Geogel 60% shot.

As shown in Figure 25, both radial and tangential stresses are initially compressive. The tangential stresses with time become tensile and achieve their maximum values as tensile stresses. The maximum values attained by the radial stresses are compressive. Values of $r_b = 106$ cm and $r_b = 123$ cm were obtained for 3,400 g charges of Geogel 60% and 2,950 g charges of Cilgel B 70%, respectively. By comparing Figures 10, 11, 13 and 14 with Figures 23 and 24, and Figures 16 to 19 with Figure 25, the general features of the stress components indicated above can easily be recognized. The decay exponents of radial and tangential stress decrease with increase of distance, and the former is smaller than the latter within the range of 1 m < r < 5 m. Also, the duration of the first radial compressive pulse at r = 60 cm is 0.55 msec, while at r = 311 cm it is 0.33 msec.

In Table 3 the ratios of detonation pressure (P_d) and imposed pressure (P_t) with the maximum radial stress at r = 100 cm and r = 200 cm are given for Geogel 60% and Cilgel B 70%. Detonation pressures for the two explosives were obtained by means of an aquarium technique. The imposed pressures on the explosive-rock interfaces shown in Table 3 were calculated by assuming as valid an acoustic coupling relation. Since the values of n and m for Geogel 60% are larger than those for Cilgel B 70%, the ratio $\sigma_{r\,ip\,max}$(Geogel)$\big/\sigma_{r\,ip\,max}$(Cilgel) increases with decreasing distance.
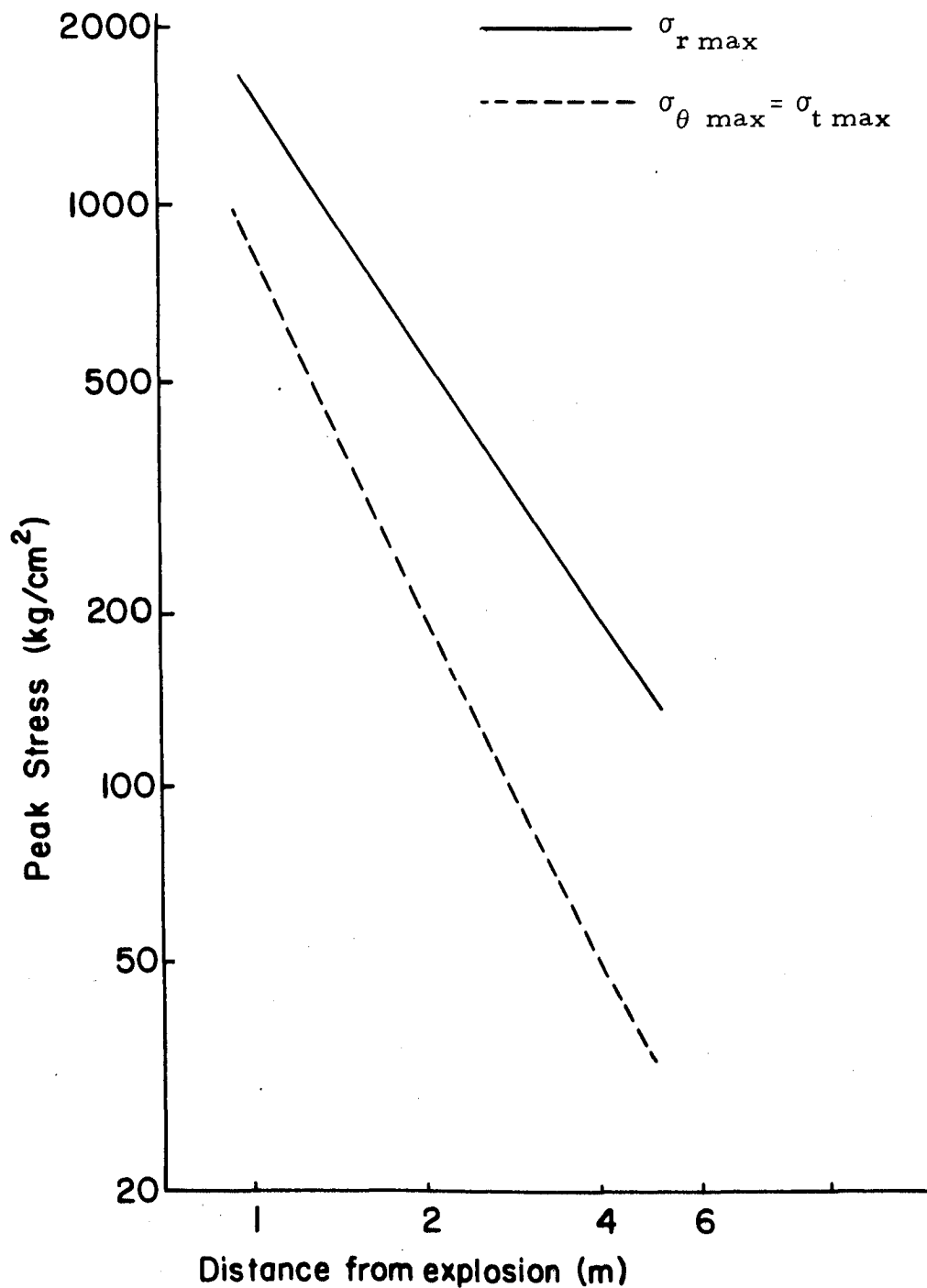
Figure 23. Logarithmic plots of the maximum values of $\sigma_{r\,max}$ and $\sigma_{\theta\,max}$ (= $\sigma_{t\,max}$) resulting from detonation of 3,400 g (2,300 cm³) cartridge of Geogel 60% vs. distance from charge centre.
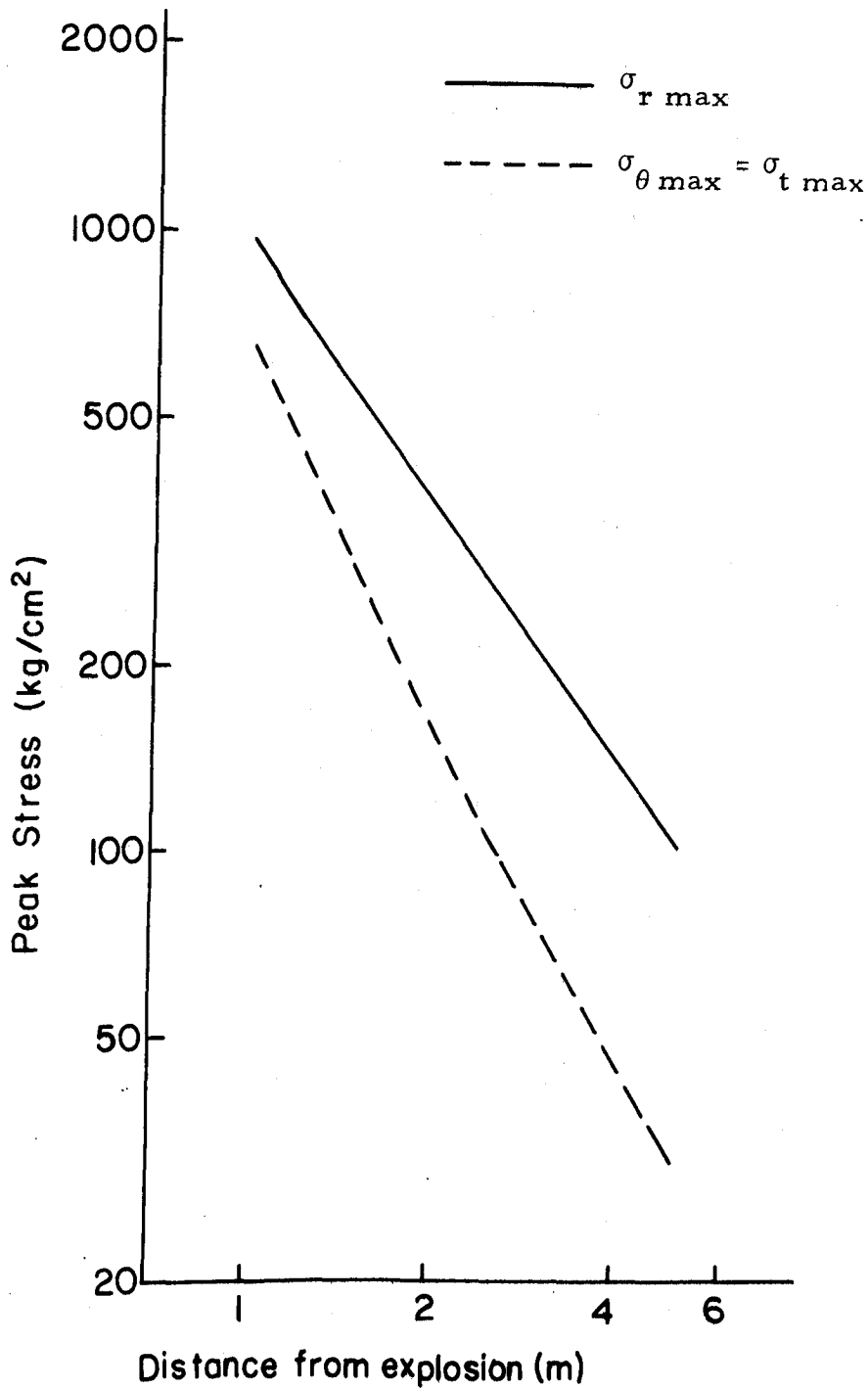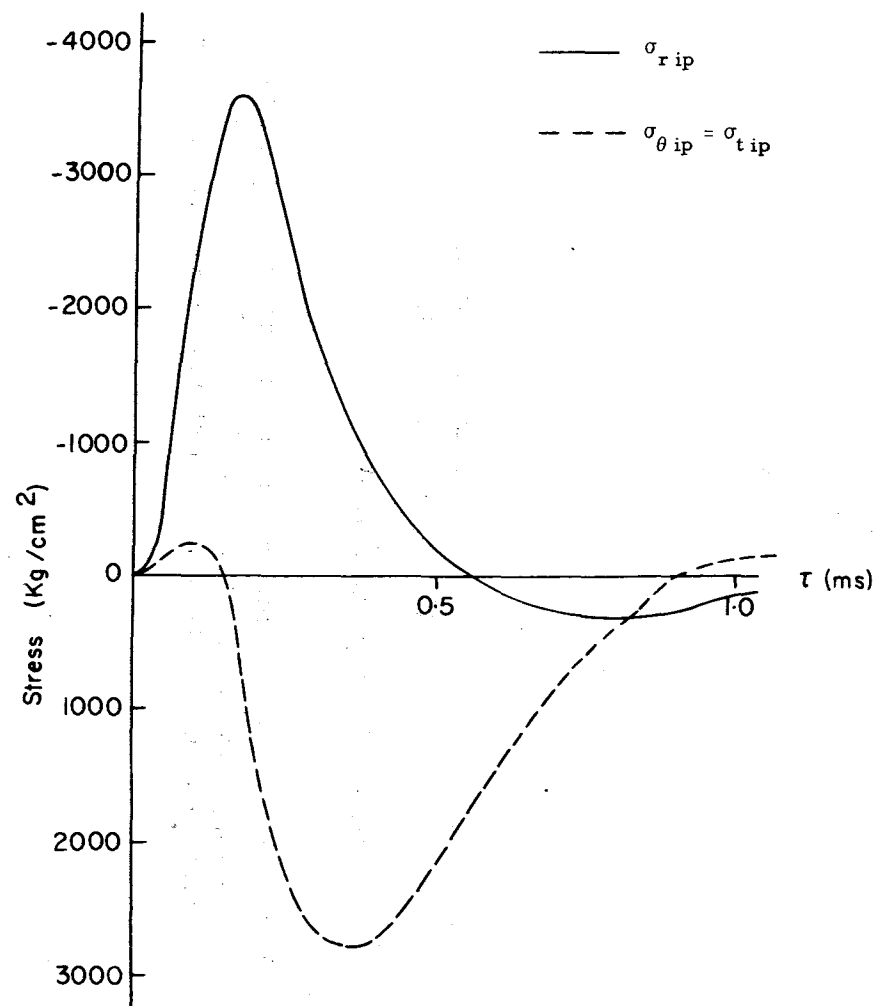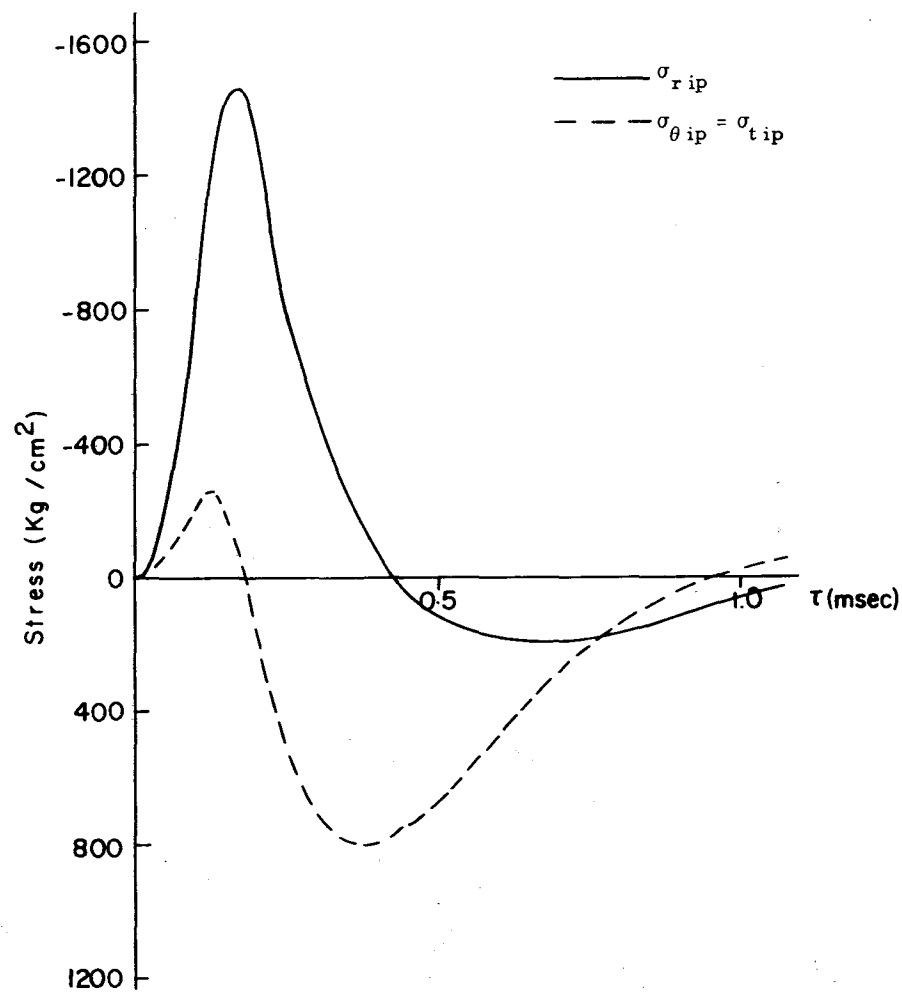
Figure 24. Logarithmic plots of the maximum values of $\sigma_{r\,max}$ and $\sigma_{\theta\,max}$ (= $\sigma_{t\,max}$) resulting from detonation of 2,950 g (2,300 cm3) cartridge of Cilgel B 70% vs. distance from charge centre.
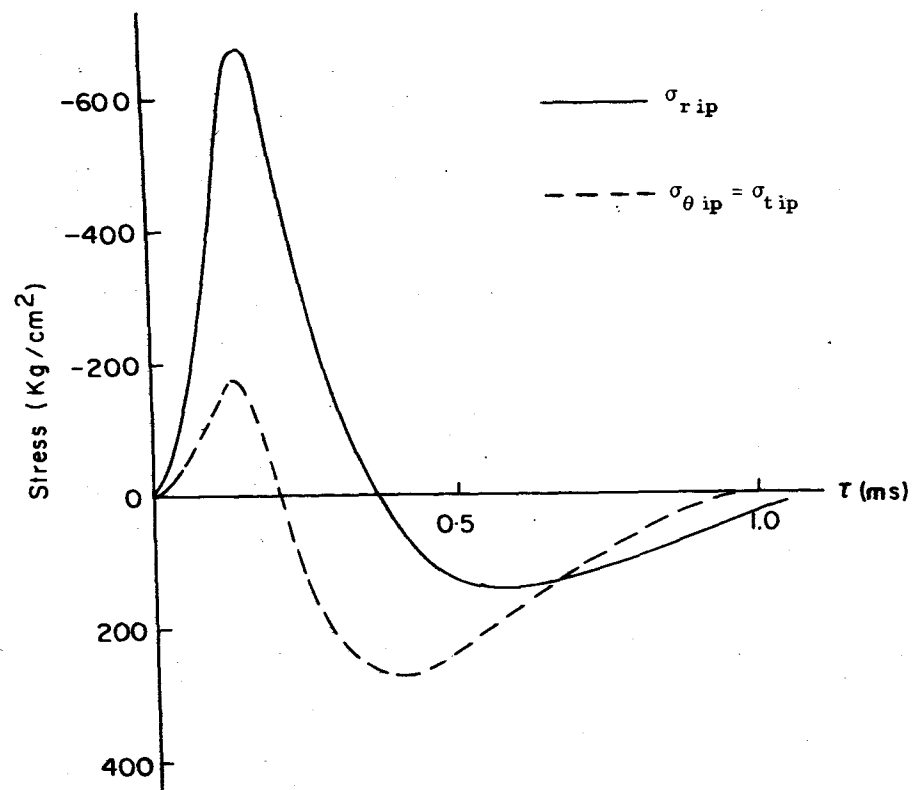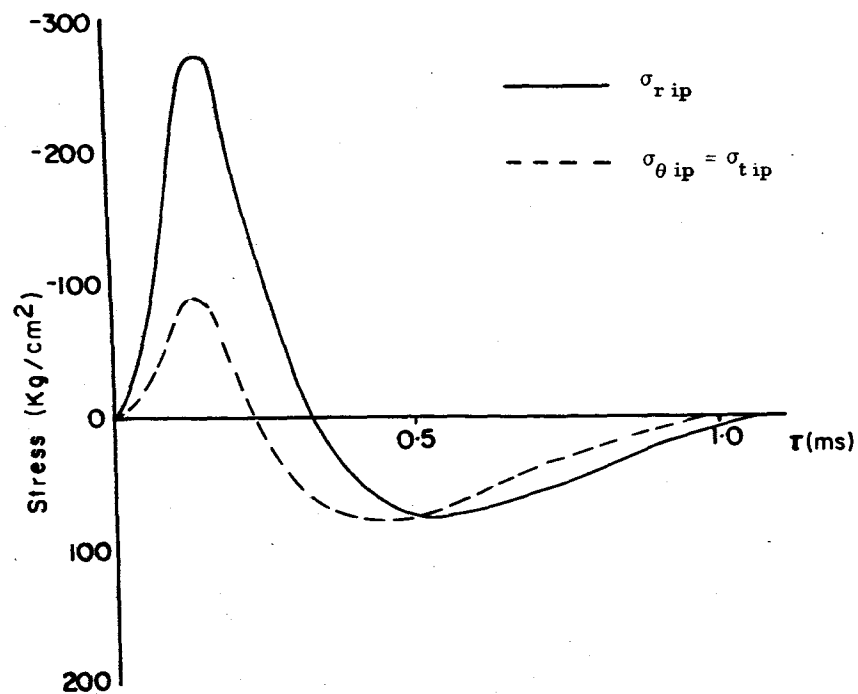
Figure 25 (a and b). Stresses caused by IP (explosive: 3,400 g Geogel 60%)

(a) at r =   60 cm
(b) at r = 103 cm

Figure 25 (c and d).   Stresses caused by IP (explosive: 3,400 g Geogel 60%)

(c) at r = 170 cm
(d) at r = 311 cm

TABLE 3

Values of P_d(Geogel)/P_d(Cilgel), P_t(Geogel)/P_t(Cilgel),
and $\sigma_{r\,ip\,max}$(Geogel)/$\sigma_{r\,ip\,max}$(Cilgel)

$\dfrac{P_d(Geogel)}{P_d(Cilgel)}$	$\dfrac{P_t(Geogel)}{P_t(Cilgel)}$	$\sigma_{r\,ip\,max}$(Geogel/$\sigma_{r\,ip\,max}$(Cilgel)	
		r = 100 cm	r = 200 cm
1.95	1.68	1.6	1.5

The total energy radiated outward through spherical shells
of various radii in the rock was calculated by using the following equation:

$$E = 2\pi r^2 \int_{t=0}^{t=t_e} (\sigma_{r\,ip} \cdot V)dt \qquad \text{Eq. 28}$$

Figure 26 is a logarithmic plot of total energy contained
within the stress wave as a function of distance, for 3,400 g charges of
Geogel 60% and 2,950 g charges of Cilgel B 70% in the range 1 m < r < 4 m.
Table 4 shows the total energy of the explosive per unit weight ($NRT/\gamma - 1$)
and the percentage of the totally available explosive energy E in the stress
wave at several scaled distances from the charge centre.

TABLE 4

Values of $NRT/(\gamma - 1)$ and $E \times 100/(NRT/(\gamma - 1))$

Explosive	$NRT/(\gamma - 1)$ (dyne cm/g)	$E \times 100/(NRT/(\gamma - 1))$ (%)		
		$r/r_c = 12.3$	$r/r_c = 24.6$	$r/r_c = 36.8$
Geogel	4.57×10^{10}	4.3	2.2	1.3
Cilgel	5.34×10^{10}	2.2	1.2	0.6

By plotting the total strain energy in the stress wave per pound
of explosive for data obtained by previous U.S. Bureau of Mines work (12, 13)
against the product of total explosive energy per pound of explosive and
detonation velocity of explosive, $(NRT/(\gamma - 1)) \cdot D$, a linear relation was obtained,
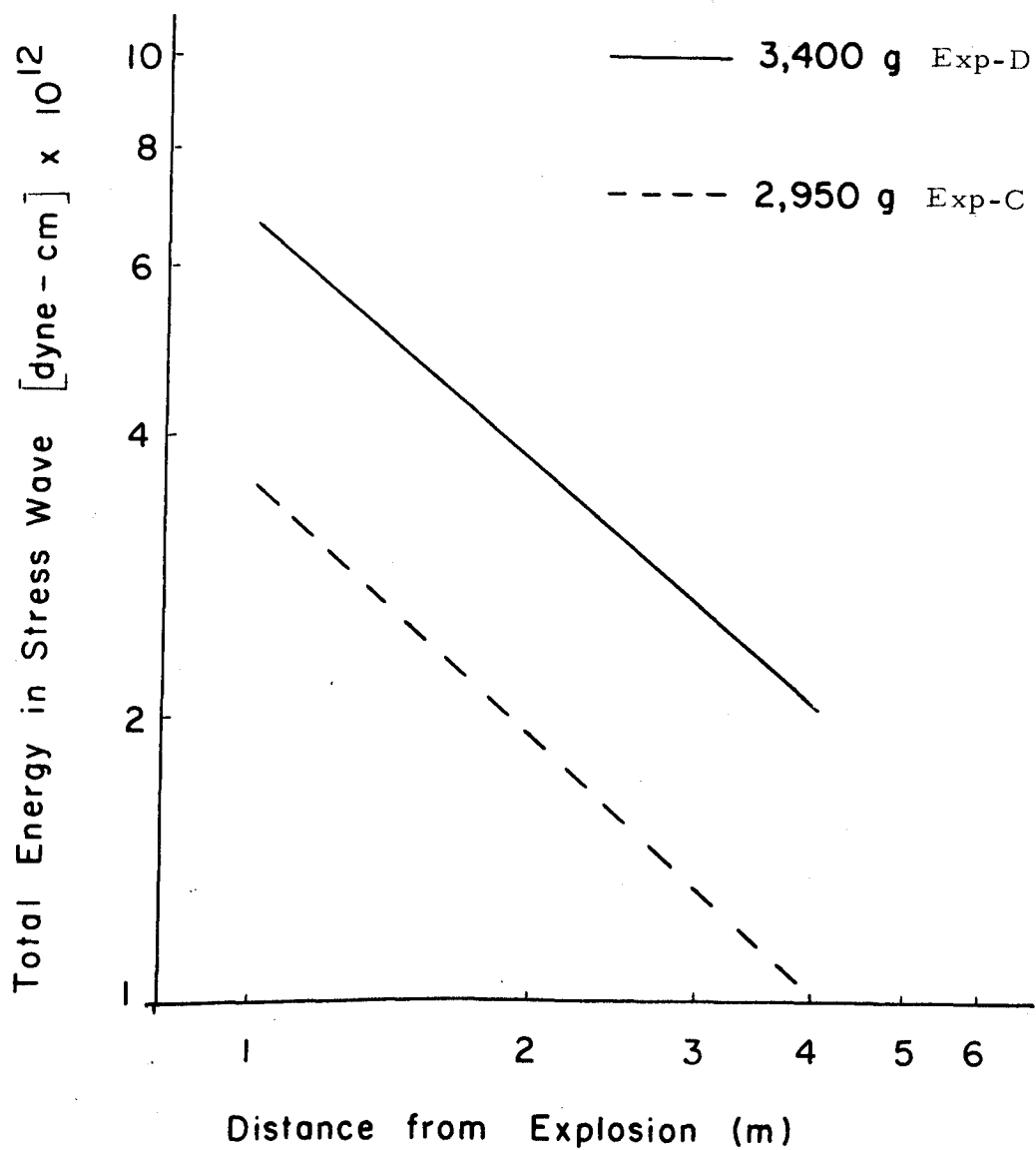
Figure 26. Relation between total energy in stress wave and distance from explosion.

as shown in Figure 27. Therefore, although the quantity of data from the present experiments is small, by using Figure 28 which shows plots of the total energy in the stress wave per 1 g of explosive at different distances against $(NRT/(\gamma-1)).D$, the total energy in the stress wave for this particular type of rock may be deduced for various types of explosives.

5.3 Dynamic Stresses Produced by One Free Face Blasting and Appearance of Breakage Presumed from the Results of this Investigation

In this study, the dynamic stresses caused by 3,400 g (2,300 cm^3) charges of Geogel 60% and 2,950 g (2,300 cm^3) charges of Cilgel B 70% were analysed for burdens of 100 cm, 120 cm, 150 cm, 200 cm and 240 cm. In order to compare the crater dimensions expected from the results of this investigation with actual crater dimensions, crater experiments were performed at the test site using the same types of explosive. In this analysis, spherical coordinates (r, θ, ϕ) with the direction of the Z-axis coinciding with that of burden and the origin at the centre of the charge, were used as shown in Figure 29. With this coordinate system, the two principal stresses in the $r\theta$ plane vary in direction with time, while the third principal stress remains fixed in the ϕ direction. In this report, the principal stress that coincides with the ϕ direction is denoted as σ_3, and the principal stresses in the $r\theta$ plane by σ_1 and σ_2.

The principal stresses due to charges of Cilgel B 70% and Geogel 60% were similar except for the peak stress values attained. Reference will be made in this report chiefly to the behaviour of the principal stresses resulting from detonation of 3,400 g charges of Geogel 60%.

Figure 30 shows the time-dependent behaviour of the principal stresses on the normal from the charge centre to the free surface in the case of a 3,400 g charge of Geogel 60% with W = 100 cm. For X = 0, the direction of σ_1 coincides with the normal from the charge centre to the free surface, and σ_2 ($= \sigma_3$) is perpendicular to the normal. As shown in Figure 30, the maximum compressive stress values of σ_1 decrease more rapidly than normally realized in a continuous medium when a free face is approached, whereas the maximum tensile values of σ_2 and σ_3 are increased as a result of the presence of the free face above what is normally realized in a continuous elastic medium. Table 5, where $-\sigma_{1\,max}/-\sigma_{r\,ip\,max}$, $\sigma_{2\,max}/\sigma_{\theta\,ip\,max}$ and $\sigma_{3\,max}/\sigma_{t\,ip\,max}$ are presented, indicates the effect of the free face on the maximum values of the principal stresses realized.
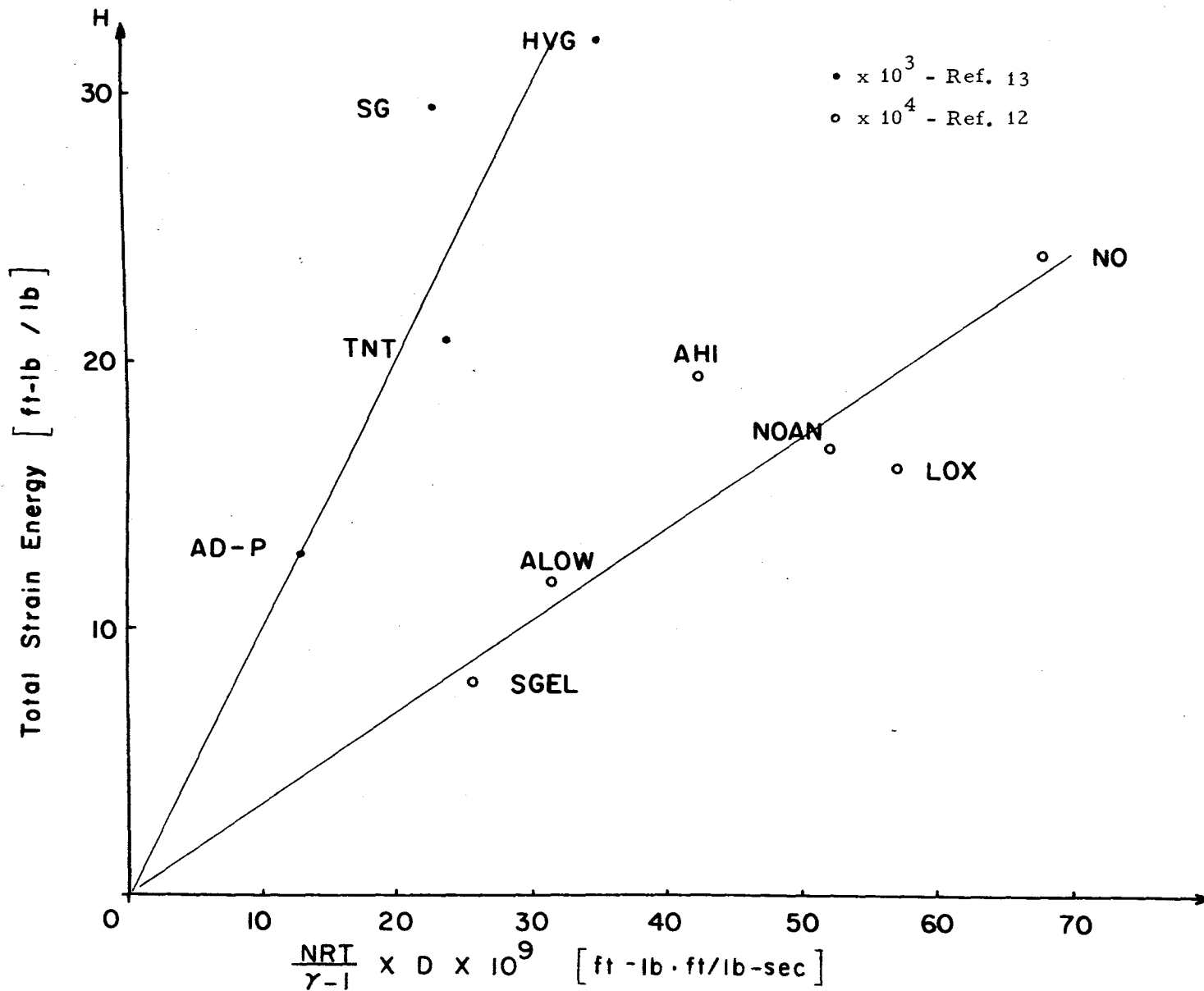
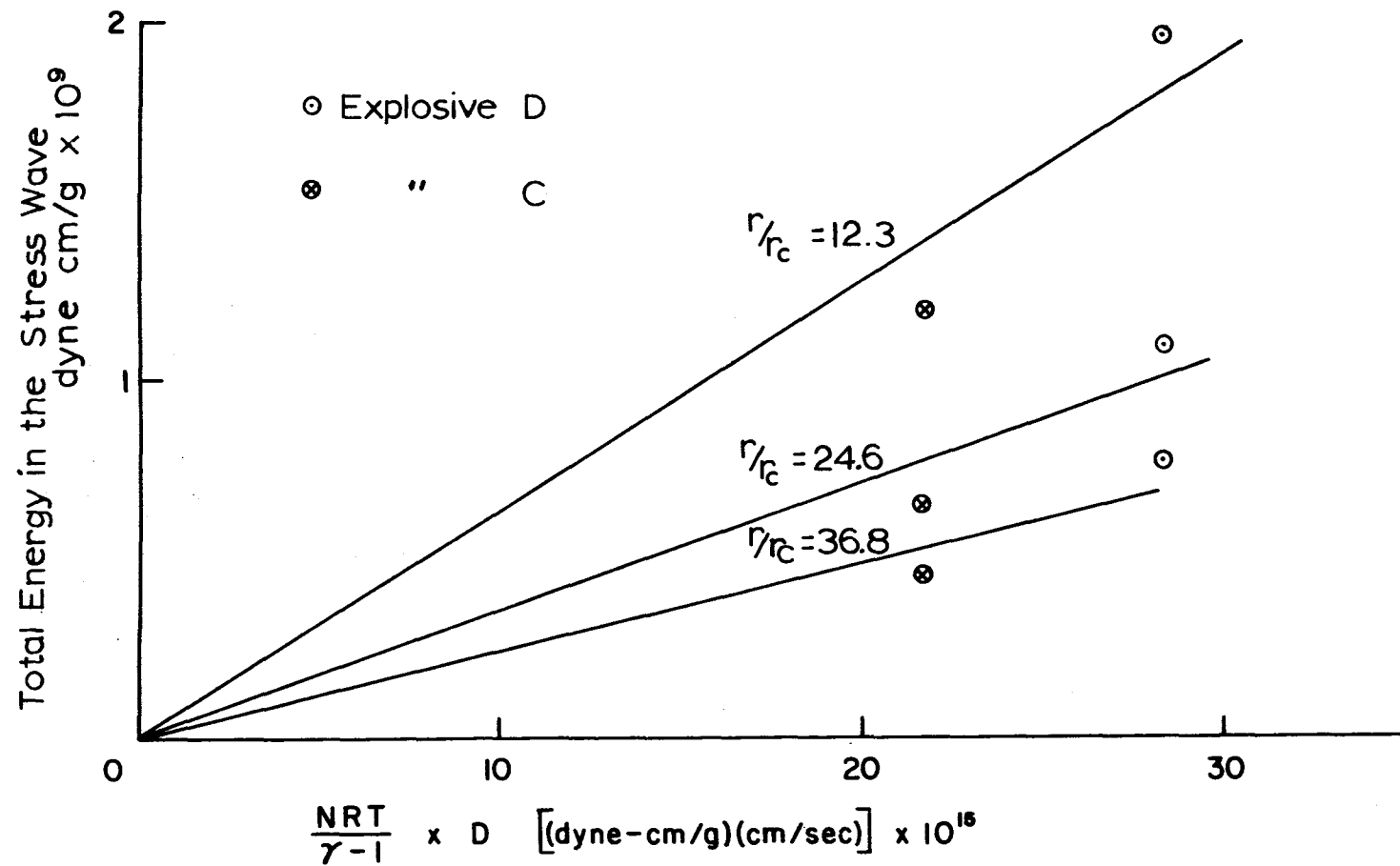Figure 27. Total strain energy vs. total energy of explosive x detonation velocity (measured).

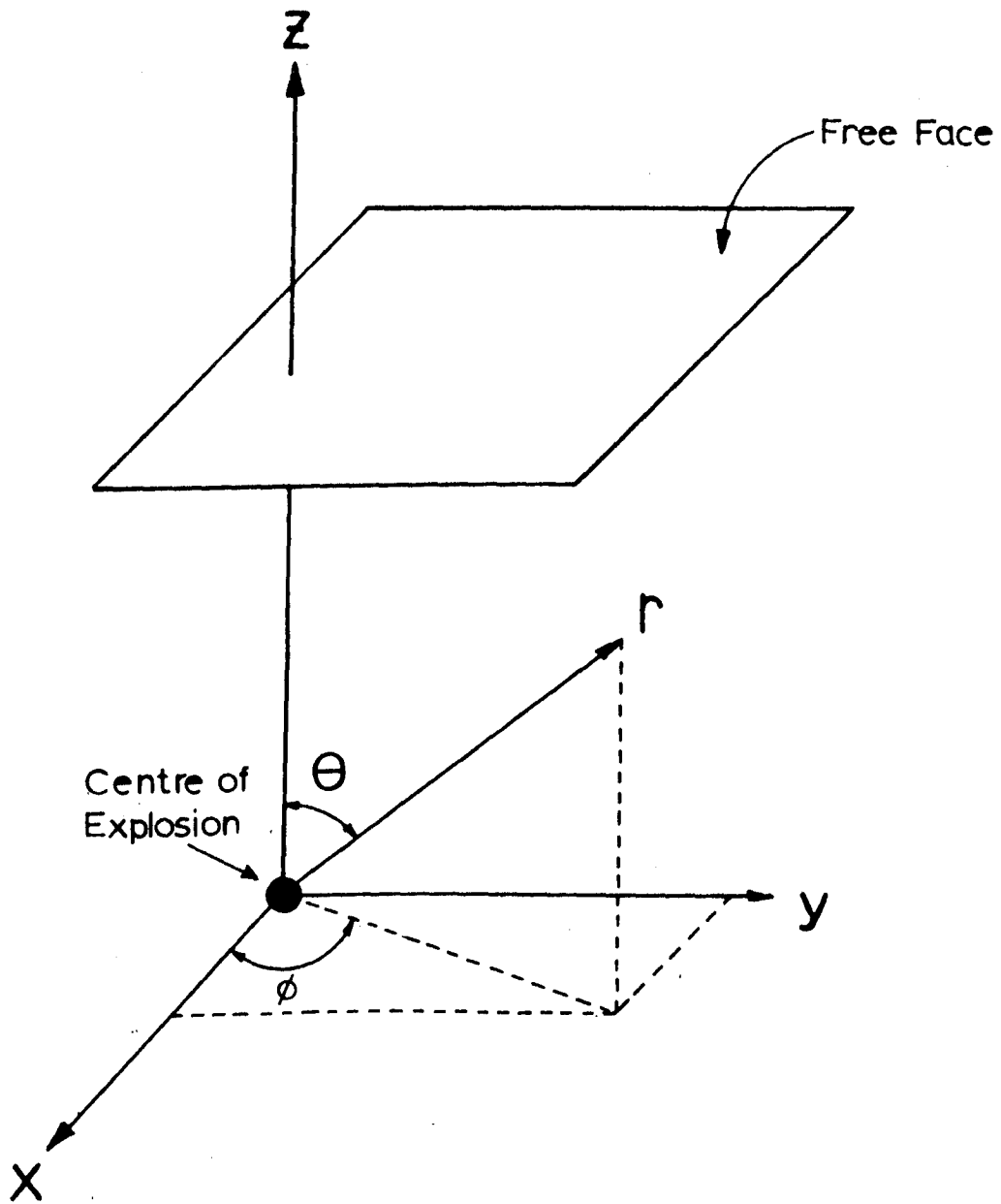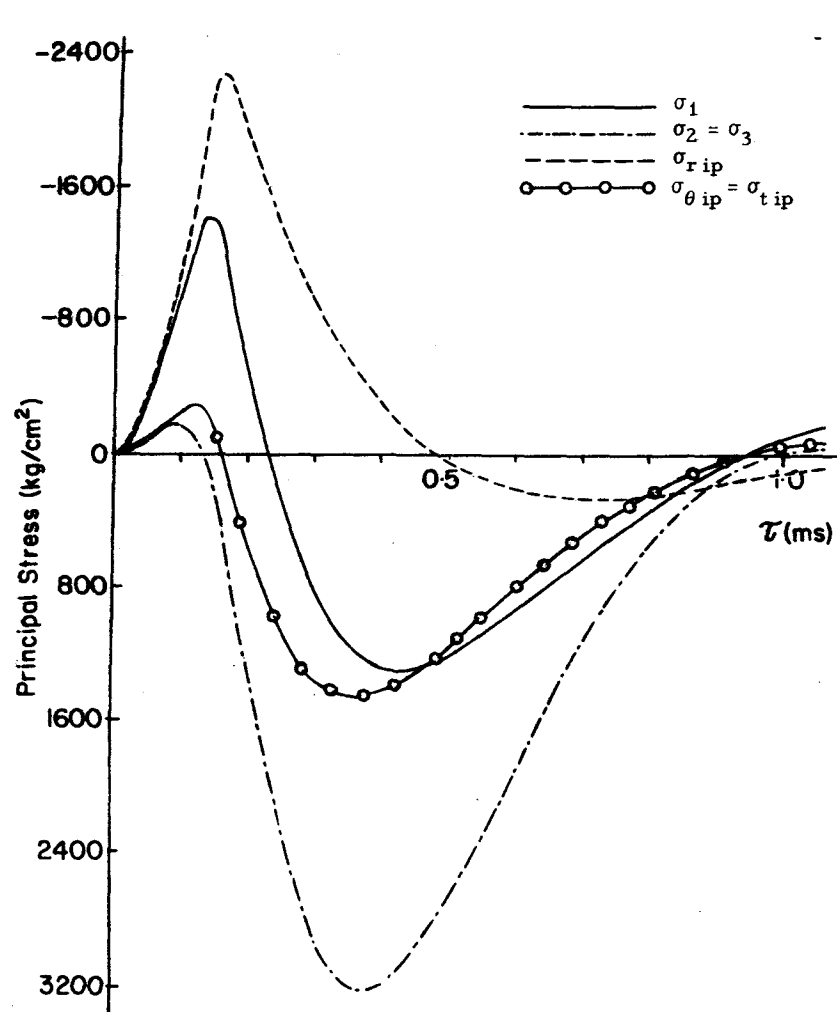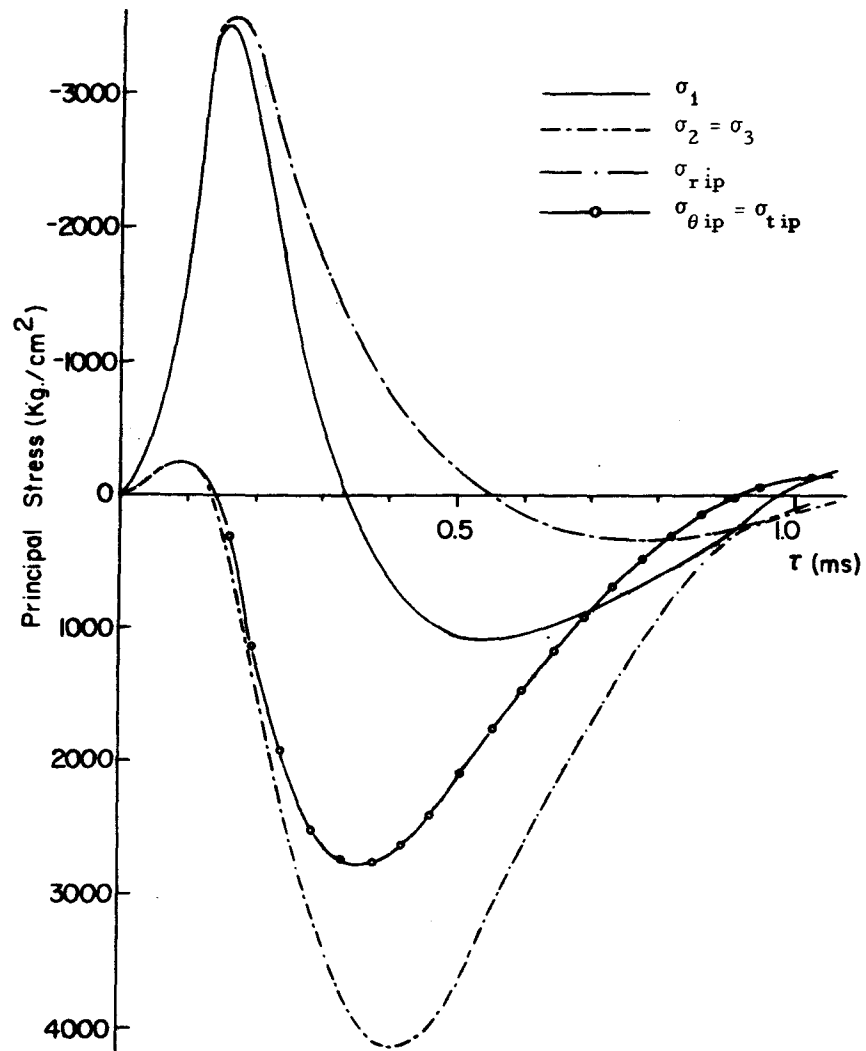Figure 28. Total energy in the stress wave vs. total energy of explosive x detonation velocity (measured).

Figure 29. Spherical coordinates used to determine the principal stresses.

Figure 30(a and b).   Principal stresses and the stresses caused by IP at X = 0 and W = 120 cm, using 3, 400 g of Geogel 60%:
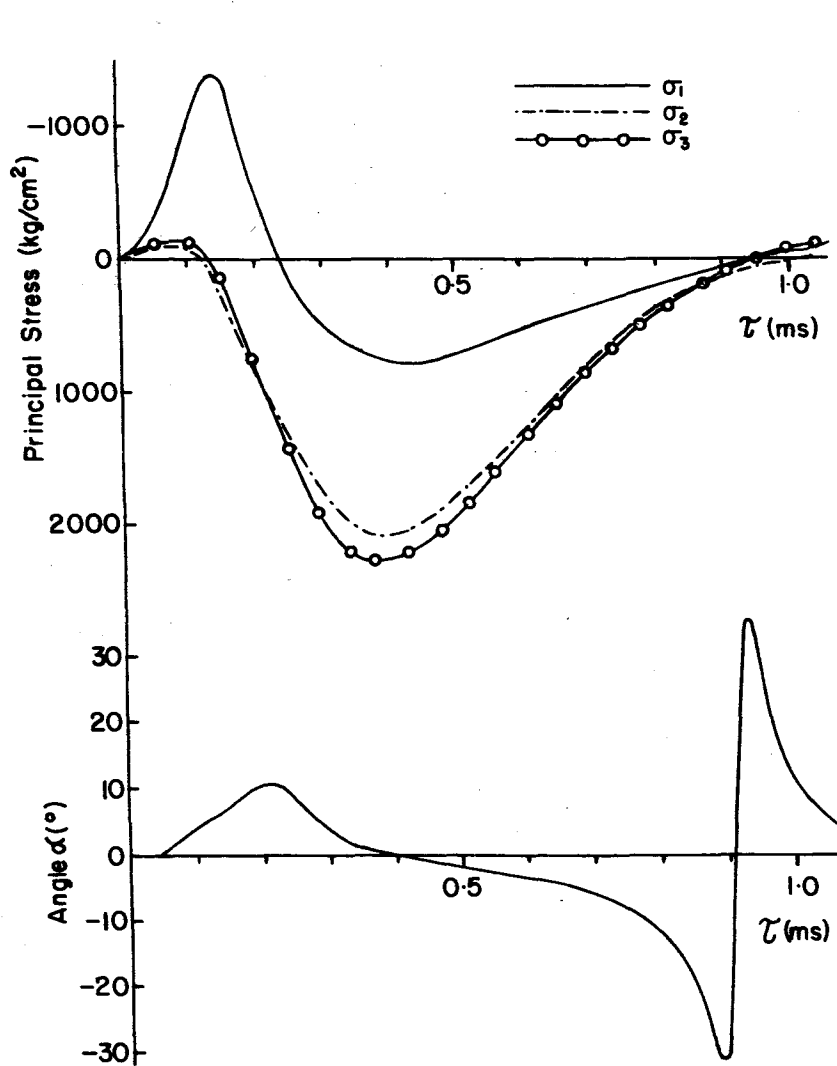
(a) Q = 20 cm
(b) Q = 40 cm

TABLE 5

Values of $-\sigma_{1\,max}/-\sigma_{r\,ip\,max}$, $\sigma_{2\,max}/\sigma_{\theta\,ip\,max}$, and $\sigma_{3\,max}/\sigma_{t\,ip\,max}$ for the case of W = 150 cm and 3,400 g Geogel 60%

|	X(cm)	2.89	32.23	63.43	98.71	141.62	198.93	286.46
Q = 30 cm	$-\sigma_{1\,max}/-\sigma_{r\,ip\,max}$	0.864	0.876	0.905	0.931	0.951	0.905	0.979
	$\sigma_{2\,max}/\sigma_{\theta\,ip\,max}$	2.161	2.072	1.805	1.500	1.520	1.305	1.435
	$\sigma_{3\,max}/\sigma_{t\,ip\,max}$	2.161	2.132	2.020	1.838	1.580	1.275	1.045
	X(cm)	3.17	35.30	69.28	107.30	152.85	212.62	302.32
Q = 60 cm	$-\sigma_{1\,max}/-\sigma_{r\,ip\,max}$	1.000	1.000	1.000	0.979	0.978	0.964	0.965
	$\sigma_{2\,max}/\sigma_{\theta\,ip\,max}$	1.315	1.280	1.390	1.460	1.660	1.780	1.935
	$\sigma_{3\,max}/\sigma_{t\,ip\,max}$	1.315	1.355	1.400	1.470	1.370	1.172	1.070
	X(cm)	3.45	38.38	75.13	115.89	164.08	222.32	318.18
Q = 90 cm	$-\sigma_{1\,max}/-\sigma_{r\,ip\,max}$	1.000	1.000	1.000	1.000	1.000	0.989	1.000
	$\sigma_{2\,max}/\sigma_{\theta\,ip\,max}$	1.025	1.110	1.319	1.512	1.638	1.930	2.295
	$\sigma_{3\,max}/\sigma_{t\,ip\,max}$	1.025	1.042	1.110	1.150	1.150	1.015	1.050

On Figure 31 (a to f), the principal stresses for a 3,400 g charge of Geogel 60% are shown at various locations with respect to the free face and charge centre. In these examples, the change in the magnitudes of the principal stresses with time and the change in the direction of σ_1 with time are shown, where α is the angle indicated in Figure 32. α is positive when H lies between 0 and the free face on the Z-axis. As shown in Figures 30 and 31, until the reflected waves arrive at A, the angle α is equal to zero and the principal stresses σ_1, σ_2 and σ_3 are determined from the plots for σ_r, σ_θ and σ_t. The directions of σ_1 and σ_2 then change with time; α is initially positive and with time becomes negative. With the arrival of the reflected free face stress components, σ_1 initially moves in a direction towards paralleling the free face and subsequently in the direction of the normal to the free face. In brittle rock the direction of tensile cracking is perpendicular to the direction of the applied tensile stress; therefore, the direction of cracking in the $r\theta$ plane should coincide with σ_1, when σ_2 reaches the dynamic tensile strength value of the rock.

Figure 33 shows the direction of σ_1 and σ_2 when the tensile stress, σ_2, reaches 200 kg/cm^2. Figure 34 shows the directions of σ_1 and σ_2 when the maximum tensile values are attained. From Figures 33 and 34, in the region $\theta > 45°$, the expected crack contours on approaching the free surface should curve gradually with distance from the shot centre, toward parallelism with the free face. As a result, convex crater profiles should be expected; and some of the craters produced at the test site had this tendency. Assuming that the dynamic tensile strength of a rock is 200 kg/cm^2, within the region $\sigma_{2\,max}$ = 200 kg/cm^2, there is the possibility that cracks will develop. These cracks would propagate in the direction of the principal stress σ_1, as shown in Figure 33.

Figure 35 shows the values of σ_1 and σ_2 on the plane Q = 20 cm at 0.3 msec and 0.5 msec after detonation for the case of W = 100 cm and a 3,400 g charge of Geogel 60%. It is evident, from Figures 31 and 35, that in all regions higher tensile stresses due to σ_2 precede the tensile stresses due to σ_1. As an example, in Figure 35a, the tensile stress due to σ_2 already exceeds the value of 200 kg/cm^2 within the region X $\leq$ 54 cm, while σ_1 in this region is still compressive. At 0.5 msec after the explosion the region (Figure 35b) in which σ_2 exceeds 200 kg/cm^2 in tension has expanded to X = 160 cm while X $\leq$ 65 cm is the region where σ_1 has exceeded 200 kg/cm^2 in tension. The tensile segment of σ_1 is chiefly produced by the reflected waves from the free face. It is therefore possible that the reflected waves which produce the tensile segment of σ_1 may be intercepted by cracks produced by the tensile segment of σ_2. Near the burden where cracks caused by σ_2 coincide almost with the radial direction from the explosive charge centre, the tensile component of σ_1 will be least affected by σ_2. Figure 36 shows the relationship of the maximum values of the principal stresses on the plane Q = 20 cm to the lateral distance X, for the case of 3,400 g charges
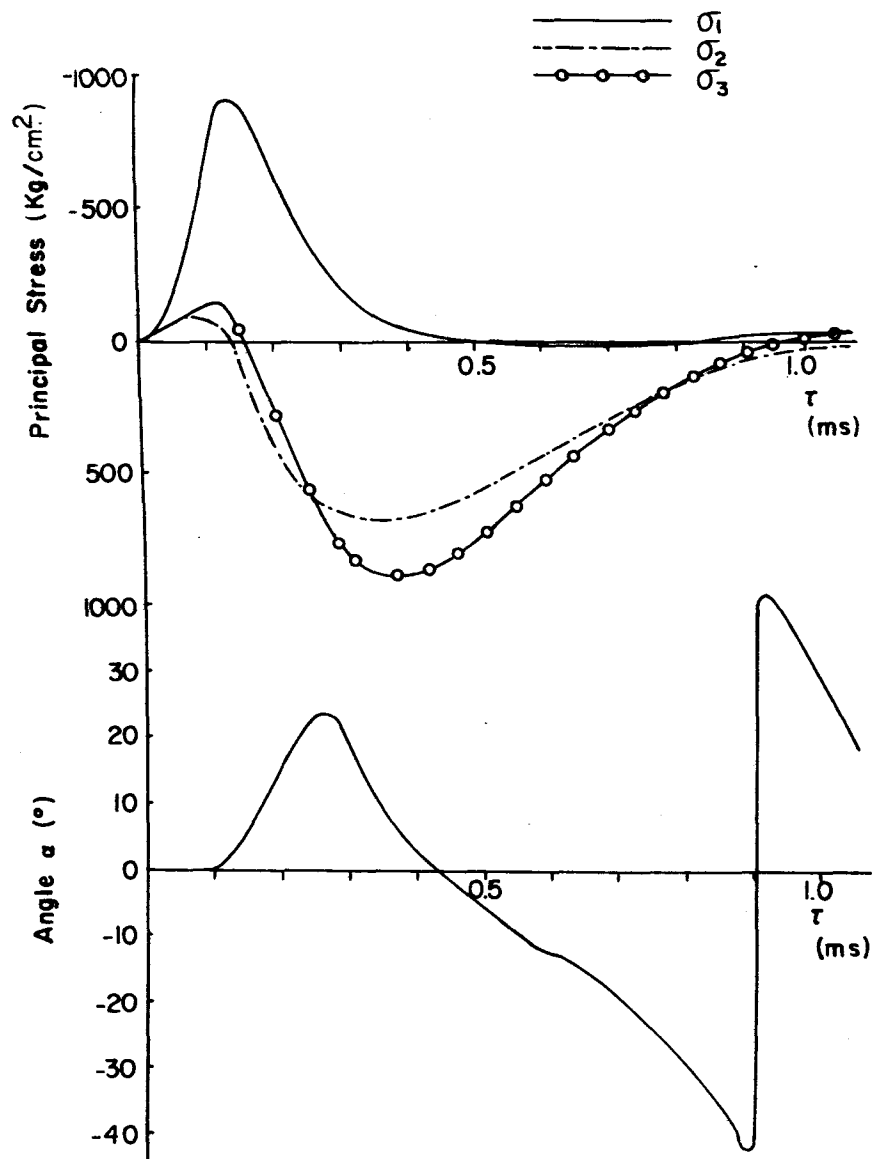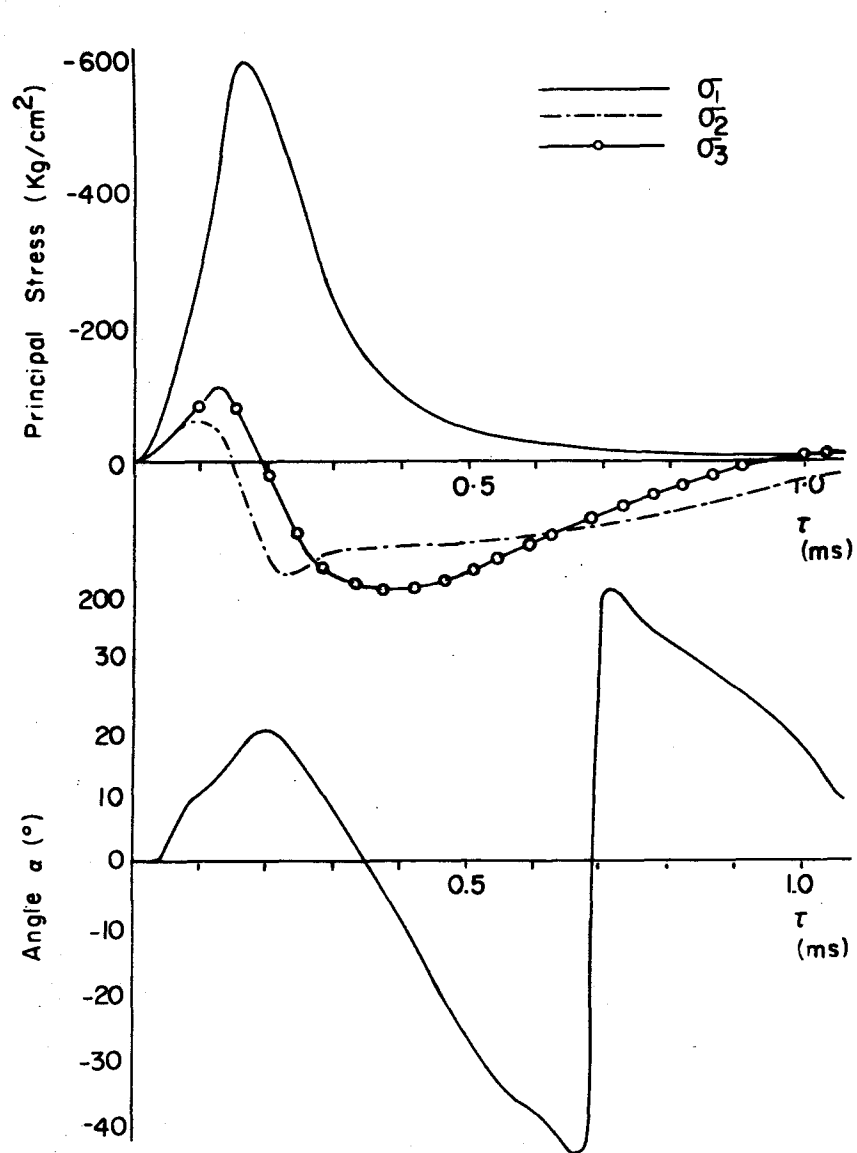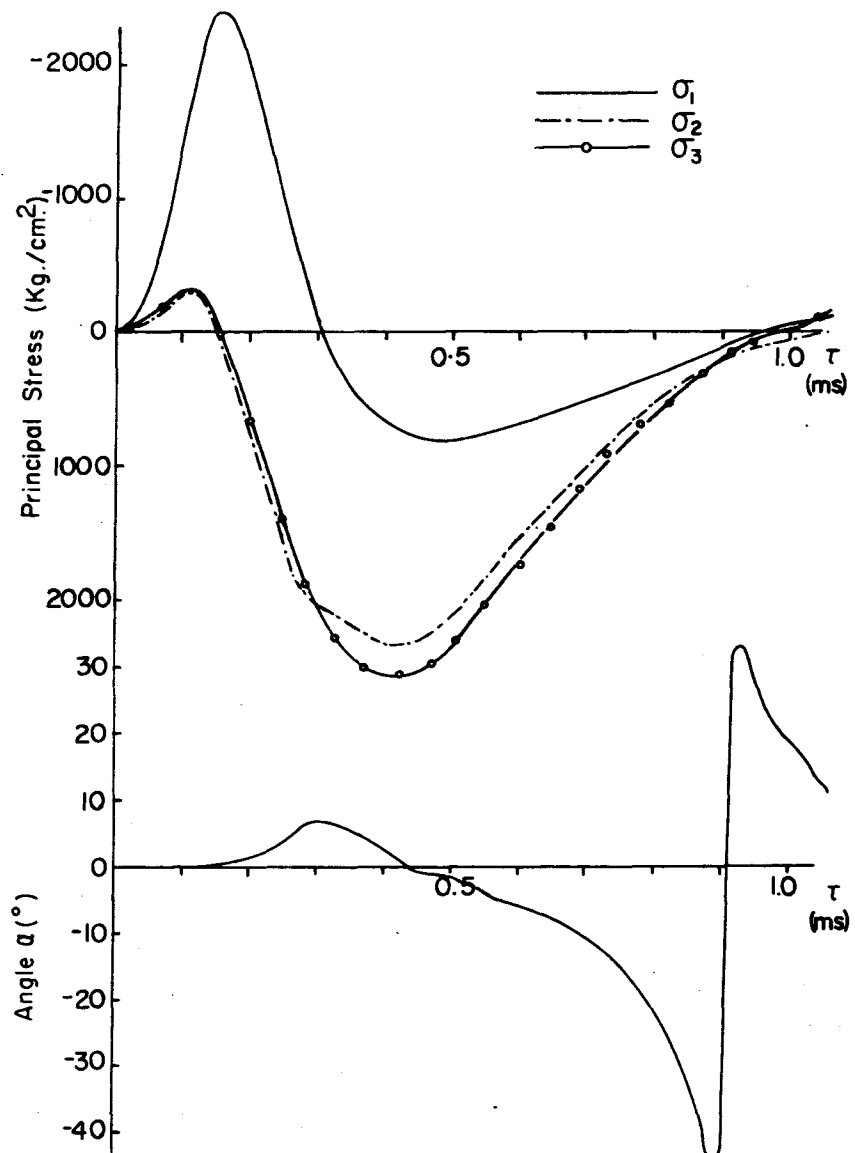
Figure 31(a and b). Principal stresses and direction resulting from detonation of a 3,400 g charge of Geogel 60%:

(a) Q = 20 cm, X = 40 cm, W = 100 cm
(b) Q = 20 cm, X = 94 cm, W = 100 cm
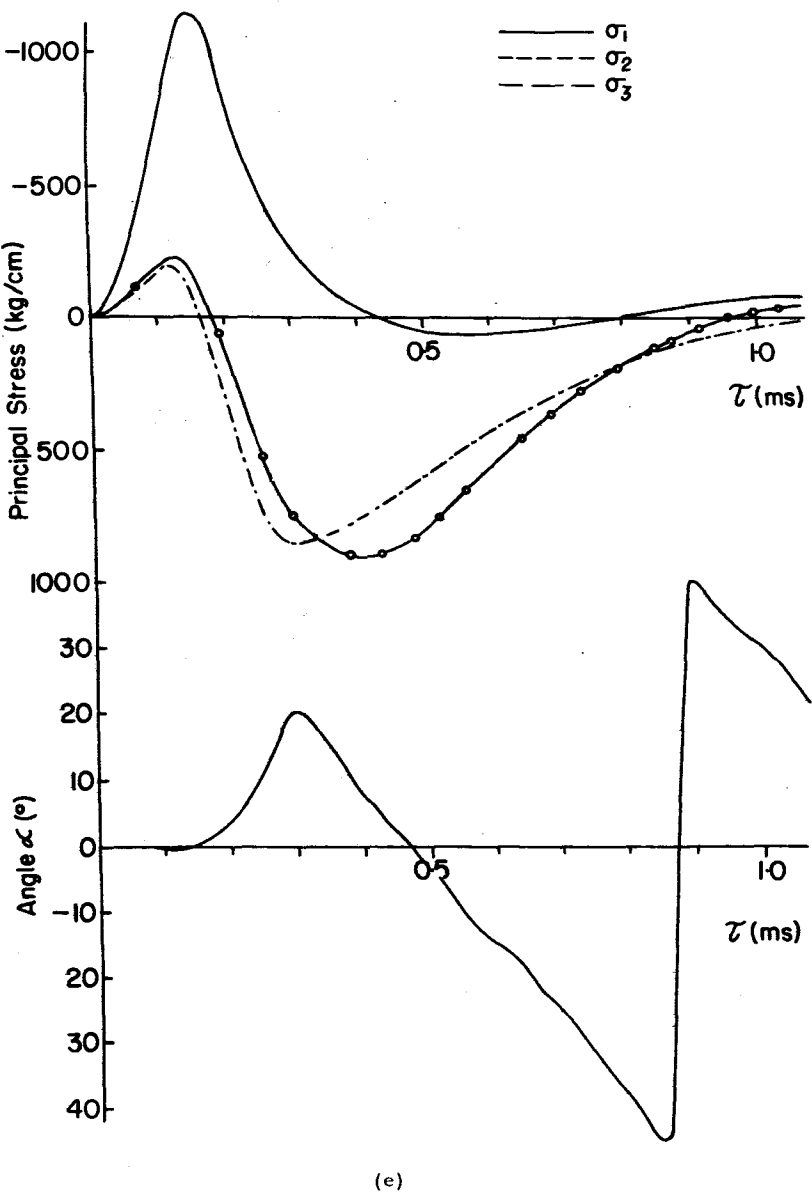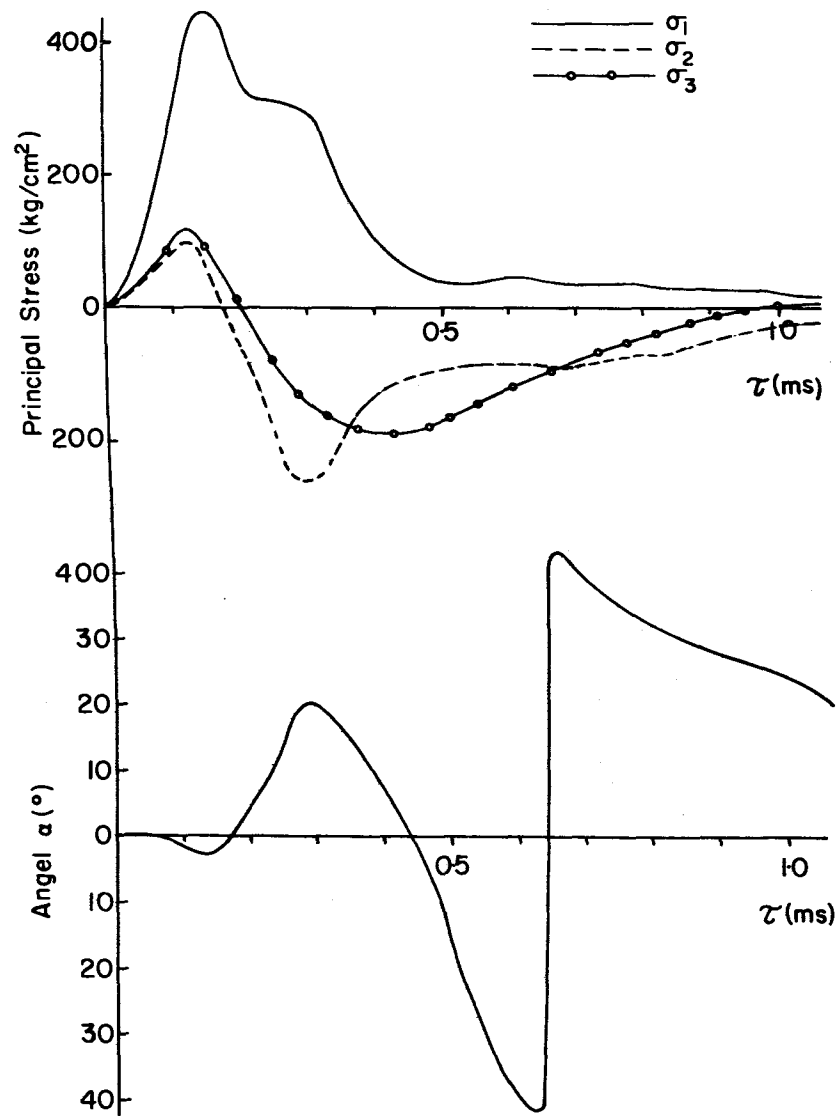
Figure 31(c and d).   Principal stresses and direction resulting from detonation of a 3,400 g charge of Geogel 60%:

(c) Q = 20 cm, X = 191 cm, W = 100 cm
(d) Q = 40 cm, X = 46 cm, W = 100 cm

Figure 31(e and f). Principal stresses and direction resulting from detonation of a 3,400 g charge of Geogel 60%:

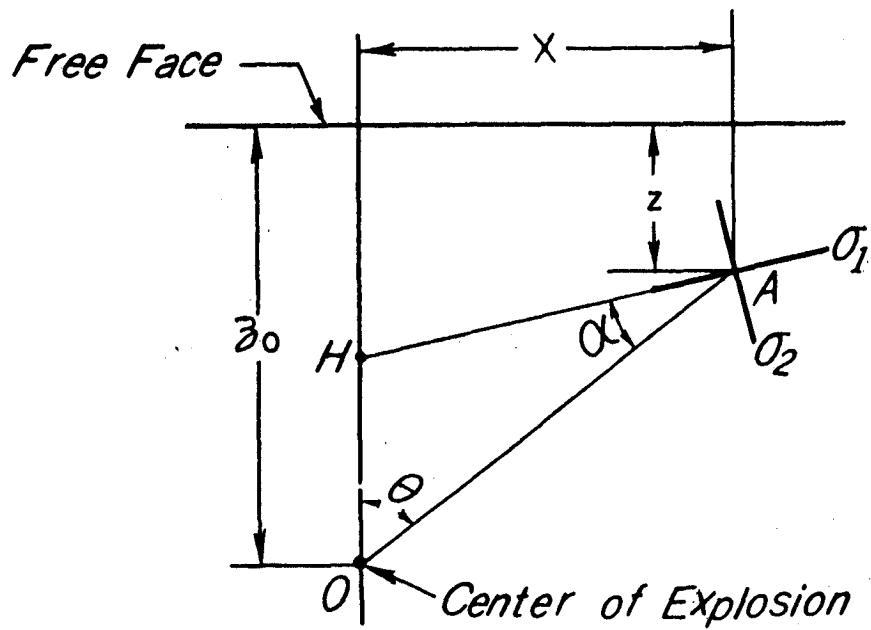(e) Q = 40 cm, X = 102 cm, W = 100 cm
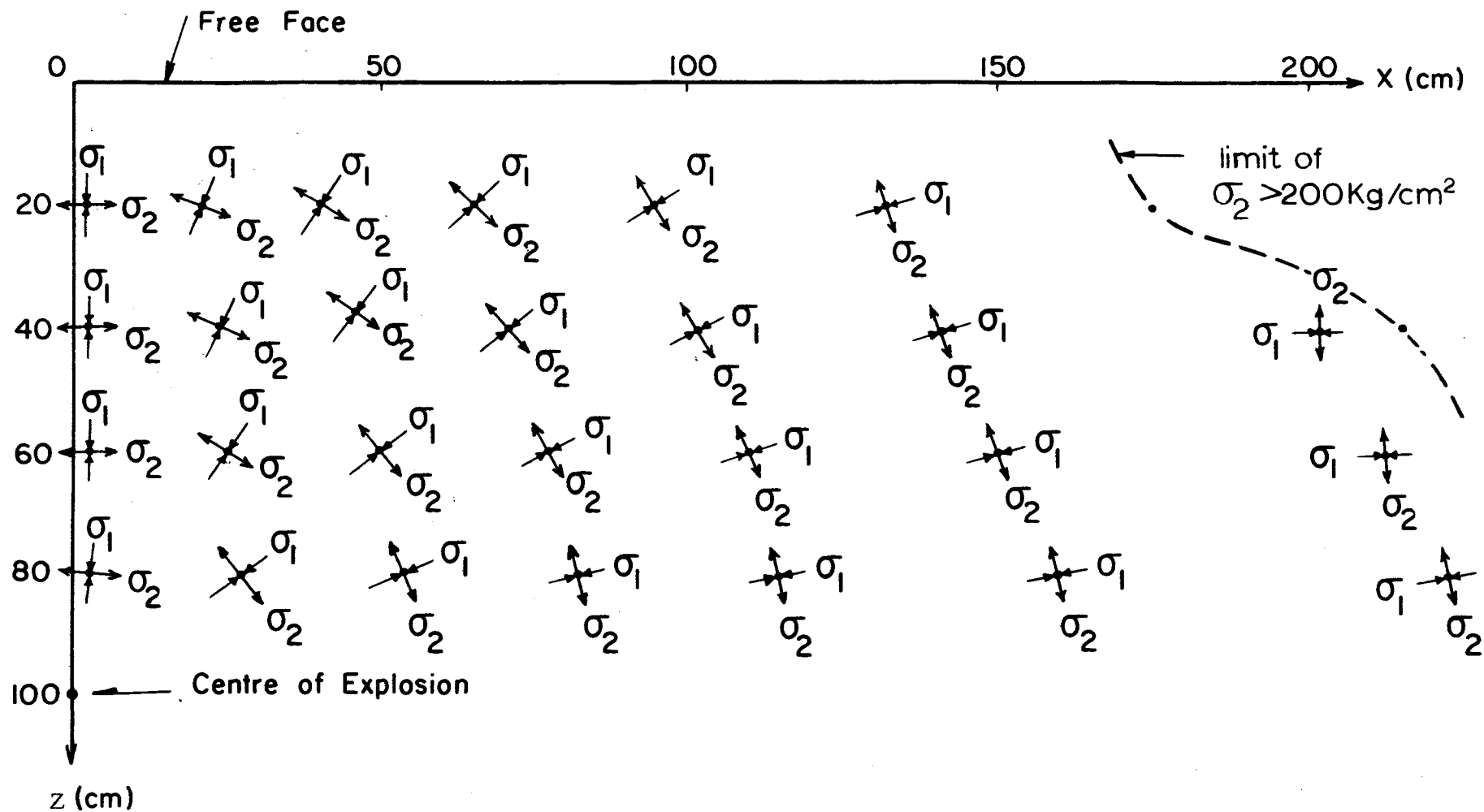(f) Q = 40 cm, X = 202 cm, W = 100 cm

Figure 32. Explanation of α.

Figure 33. Directions of the principal stresses when the tensile stress value of σ_2 attains 200 kg/cm^2 for the case of W = 100 cm. (Explosive charge: 3,400 g Geogel 60%).
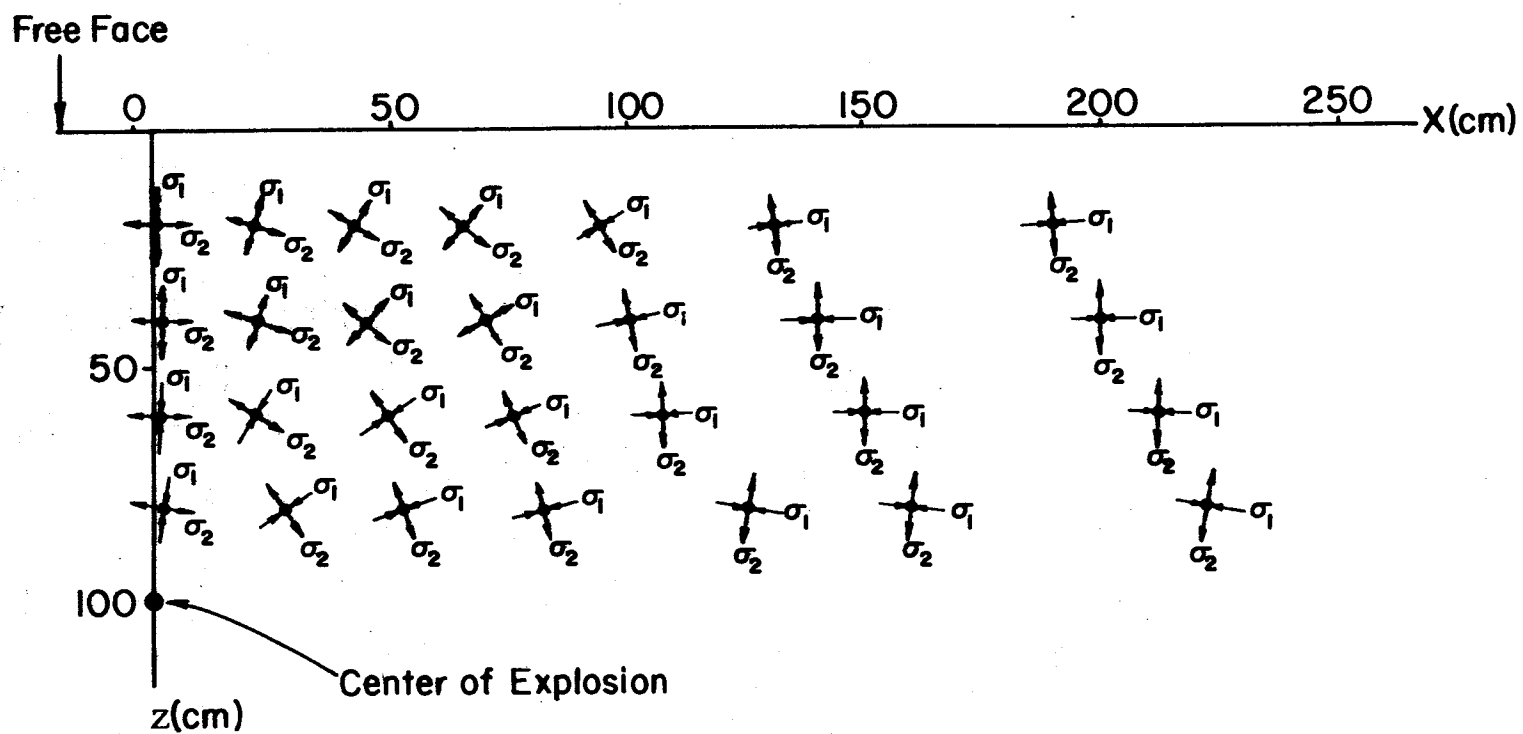
Figure 34. Directions of σ_1 and σ_2 when the tensile stress value of σ_2 attains its maximum value for the case of W = 100 cm. (Explosive charge: 3,400 g Geogel 60%).
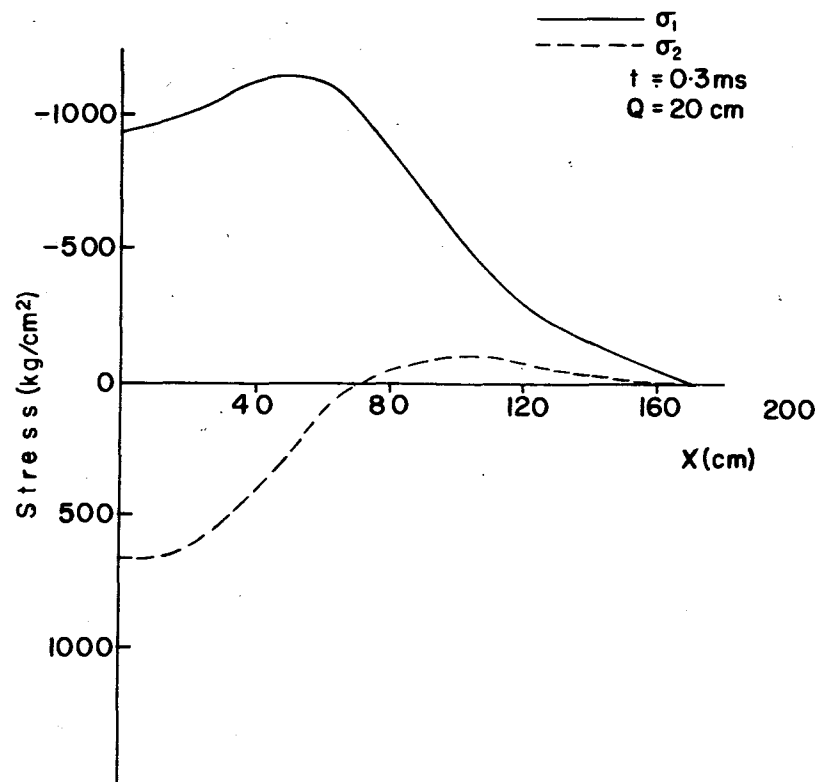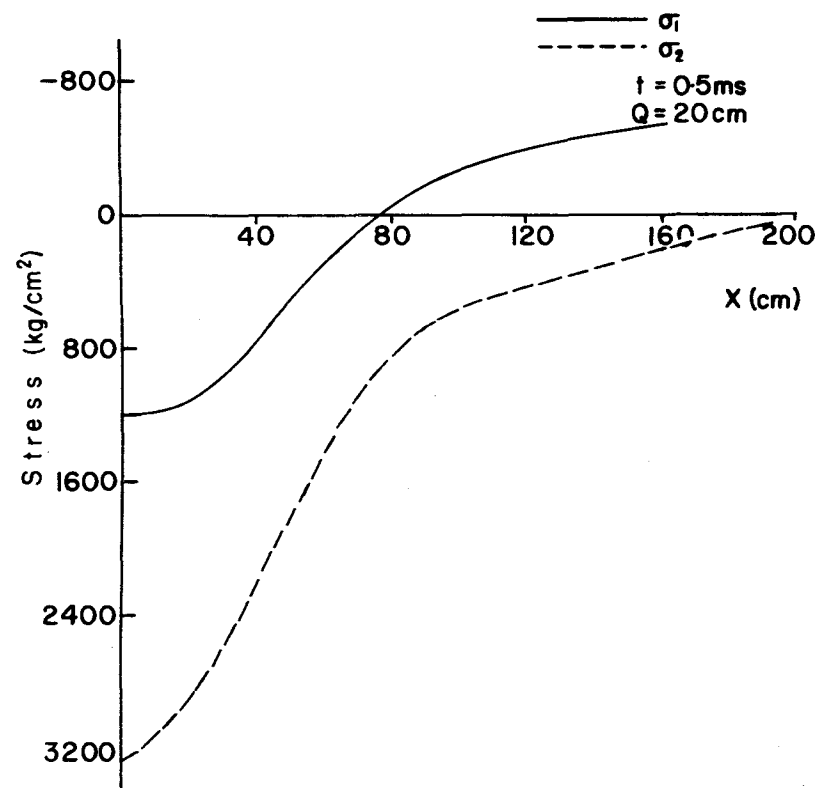
Figure 35(a and b). Stress condition on the plane Q = 20 cm after detonation, for the case of W = 100 cm.
(Explosive charge: 3,400 g Geogel 60%).

(a) 0.3 ms
(b) 0.5 ms

Figure 36. Relation between the maximum values of principal stresses on the plane of Q = 20 cm versus the lateral distance, for the case of W = 100 cm. (3,400 g Geogel 60%).

of Geogel 60%, W = 100 cm. Even if no cracks are produced by σ_2, σ_1 only has a tensile segment within the range X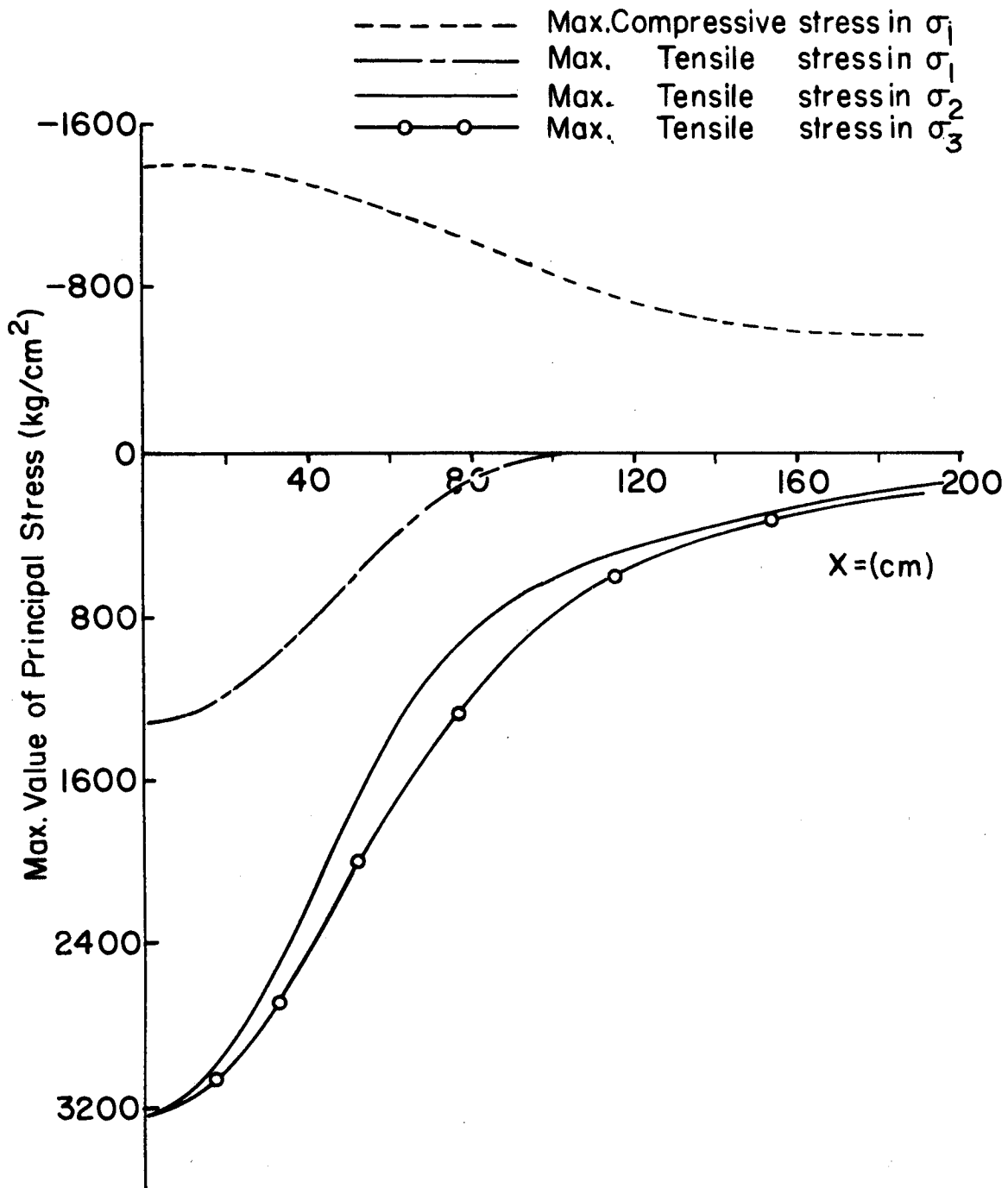 < 100 cm. However, cracks that are parallel to the free face and in the region of the burden are believed to be due to σ_1 tensile stresses. Since the maximum tensile stress value of σ_3 is always larger than that of σ_2 at any location, radial cracks on the free face should be more extensively developed than concentric cracks, resulting in a tendency for concentric cracks to terminate on radial cracks.

5.4 Comparison Between the Crater Dimension Predicted from this Investigation and That Obtained by the Crater Test Near the Test Site

For the purpose of comparison with predicted crater dimensions, some crater tests were performed at the test site, using Geogel 60% and Cilgel B 70% (7). Shot holes 7.5 cm in diameter were drilled using a percussion drilling machine. These holes were drilled in from the surface, at an angle of 45º with respect to the free face. The charge weights for the crater tests were selected so as to maintain the previously used length-to-diameter ratio of 3 to 1. For the crater tests, the charge weights were 1,440 g and 1,250 g for the Geogel 60% and Cilgel B 70% respectively.

TABLE 6

Summarized Condition of Crater Studies

Explosive	Amount of Explosive	Length of Burden	Number of Shots
Geogel 60%	1,440 g	90 cm 165 cm 173 cm 180 cm	4 1 1 1
Cilgel B 70%	1,250 g	75 cm 135 cm 150 cm 165 cm	3 1 1 1

Comparison of predicted and actual craters was made only in the case of Geogel 60%; the crater results realized with Cilgel B 70% were too scattered to be conclusive. The actual crater dimensions realized with 1,440 g charges of Geogel 60% were adjusted to equivalent craters for 3,400 g charges of Geogel 60%. Figure 37 shows the adjusted profiles of two craters produced with Geogel 60%. Figure 38 shows the relation between the maximum value of the principal stresses on the plane Q = 20 cm as a function of lateral distance X.
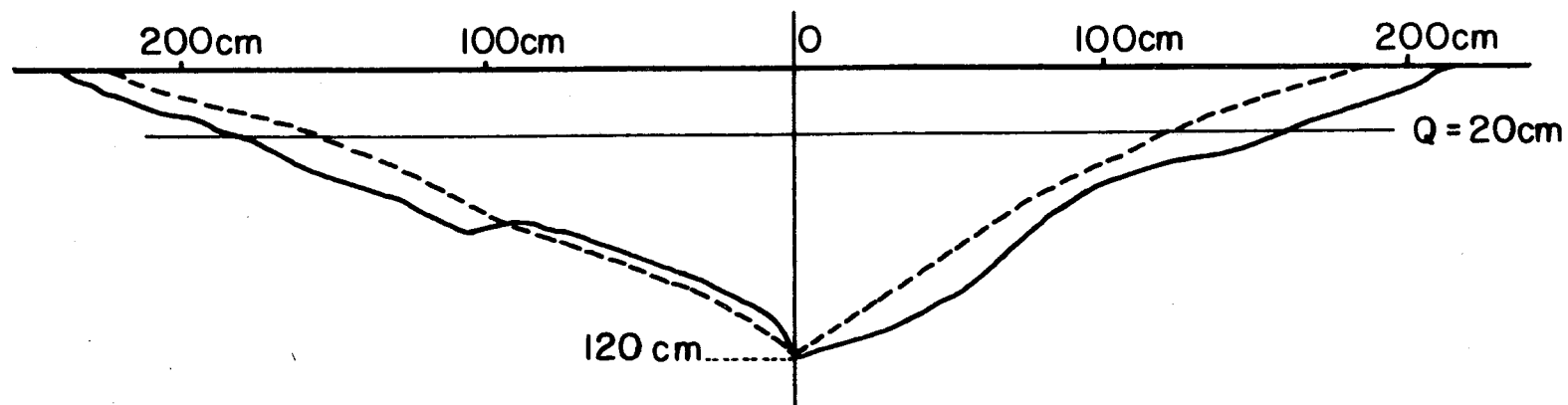
Figure 37. Crater profiles expected from 3,400 g charges of Geogel 60%
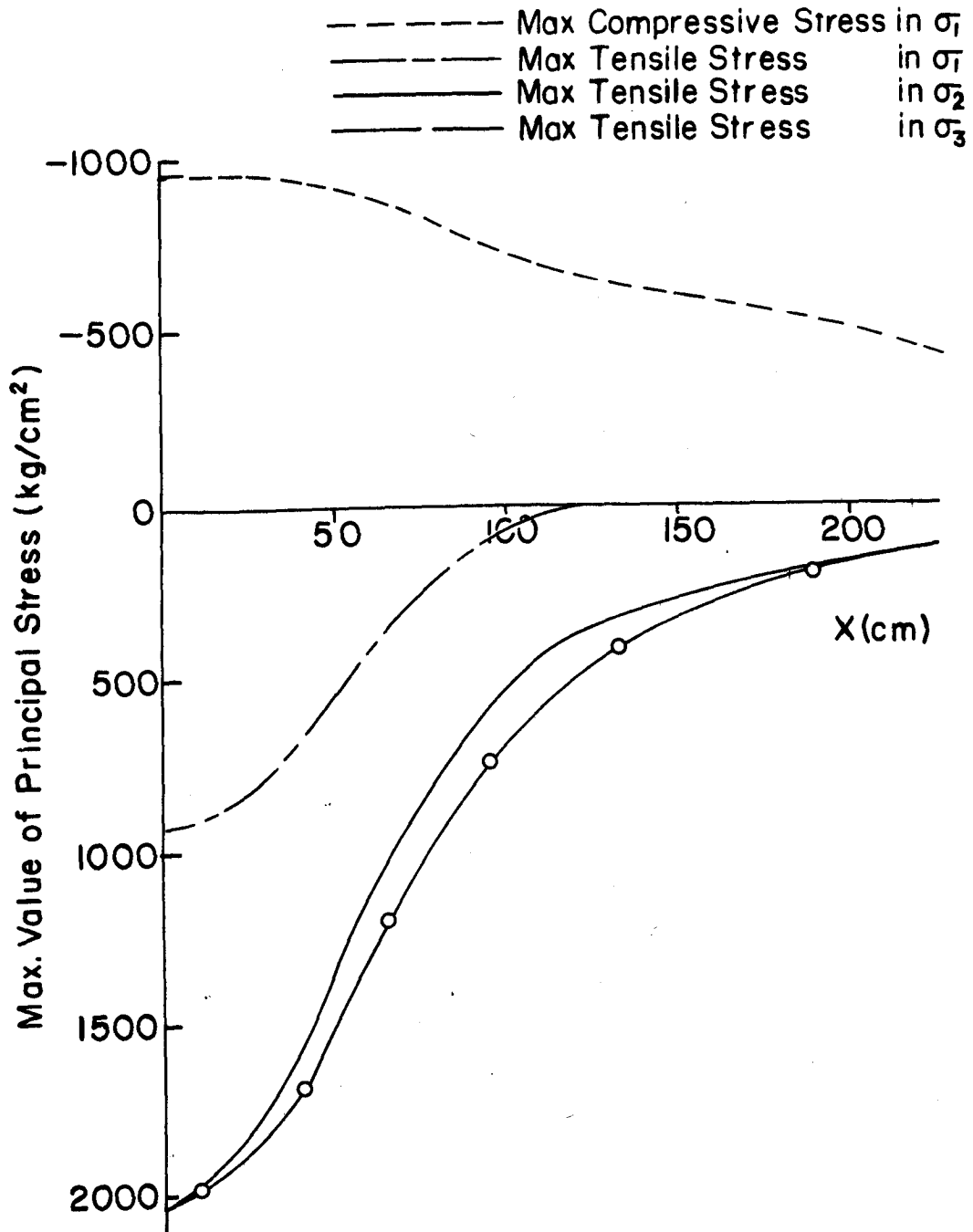for the case of W = 120 cm.

Figure 38. Relations between the maximum principal stress values on the
plane Q = 20 cm, for the case of W = 120 cm.   (3,400 g Geogel 60%).

The dynamic tensile strength of the rock in the Carol Lake deposit was determined as 130 kg/cm^2. Applying this value to Figure 38, X = 220 cm is obtained as the limiting distance where the maximum tensile stress value of σ_2 exceeds the dynamic tensile strength of the rock.

As mentioned earlier, it is assumed that the radial cracks resulting from an explosion follow the direction of σ_1 when the maximum tensile stress value of σ_2 exceeds the dynamic tensile strength of the rock and that they terminate when the maximum tensile stress value of σ_2 is equal to the tensile strength of the rock. Assuming that the cracks caused by σ_2 determine the shape of a crater for normal rock blasting, it is noted that cracks may propagate within the range X $\leq$ 200 cm beyond the plane of Q = 20 cm. For Q < 20 cm, no cracks exist in the region X > 220 cm for the case of W = 120 cm and a 3,400 g charge of Geogel 60%. As a result the expected crater radius for the case of W = 120 cm and a 3,400 g charge of Geogel 60% is about 200 cm.

6. CONCLUSIONS

This study indicates that relative stress levels in elastic rock masses, resulting from the detonation of contained charges, possibly can be determined from the dynamic properties of the rock and the detonation properties of the explosive by means of the acoustical coupling relationship. Some agreement has been realized between predicted and actual surface crater dimensions; thus the region of successful application of this method of analysis has been extended from the previously reported small charges (4) to moderate size explosive charges. It thus seems that the method of stress analysis used in this work provides a valid representation of the stress conditions beyond the crushed zone and that the maximum tensile strength theory is a good representation of the mode of failure in this region.

7. ACKNOWLEDGEMENTS

8. REFERENCES

1. Sassa, K. and Coates, D.F., "Stress Waves Close-in from Surface Explosions", Divisional Report FMP 64/126-MRL, Mines Branch, Department of Mines and Technical Surveys, Canada (1964).

2. Atchison, T.C., Duvall, W.I. and Pugliese, J.M., "Effect of Decoupling on Explosion-Generated Strain Pulses in Rock", U.S. Bureau of Mines Report, RI 6333 (1964).

3. Austin, C.F., Cosner, L.N. and Pringle, J.K., "Shock Wave Attenuation in Elastic and Inelastic Rock Media", 7th Symposium on Rock Mechanics, Pennsylvania State University (1965).

4. Sassa, K. and Ito, I., "Dynamic Stresses Induced within Rock for the Case of Blasting with One Free Face", SME TRANSACTIONS (Oct. 1963).

5. Ito, I. and Sassa, K., "On the Detonation Pressure Produced at the Inner Surface of the Charge Hole", International Symposium on Mining Research (Pergamon Press, 1962), p. 103.

6. Ito, I. and Sassa, K., "On the Dynamic Stresses within Rock Caused by an Explosion", Bulletin of Min. and Metall. Inst., Japan, Vol. 1, No. 1 (Dec. 1961).

7. Larocque, G., Sassa, K. and Darling, J.A., "Blasting Research Field Report", Divisional Report FMP 65/104-MRL, Mines Branch, Department of Mines and Technical Surveys, Canada (1965). Unpublished report.

8. Parsons, R.C., "Physical and Mechanical Properties of Carol Lake Ore", Divisional Report FMP 65/107-MRL, Mines Branch, Department of Mines and Technical Surveys, Canada (1965). Unpublished report.

9. Larocque, G.E., "Determination of the Dynamic Tensile Strength of a Series of Magnetite Specimens from Carol Lake, Labrador", Divisional Report FMP 65/9-MRL, Mines Branch, Department of Mines and Technical Surveys, Canada (1965). Unpublished report.

10. Ito, I., "On the Radial Strain Caused by Explosion in Rocks", Suiyokwai-
    shi (Trans. Min. and Metall. Alumni Assoc. Kyoto Univ.),
    Vol. 13, No. 5 (1957).

11. Sassa, K., "Mechanism of Breakage by Blasting", doctorate thesis,
    Kyoto University (1962).

12. Fogelson, D.F., Duvall, W.I. and Atchison, T.C., "Strain Energy in
    Explosion-Generated Strain Pulse", U.S. Bureau of Mines
    Report, RI 5514 (1959).

13. Nicholls, H.R., "Coupling Explosive Energy to Rock", Geophysics,
    Vol. 27, No. 3 (1962).

- - - -

9. GLOSSARY OF SYMBOLS AND ABBREVIATIONS

a	-	attenuation coefficient
$A_o(L)$	-	displacement intercept on y-axis on a log-log plot of peak particle displacement vs distance or range
AX	-	diamond drill hole size, 1 7/8 in. diameter
$B_o(LT^{-1})$	-	velocity intercept on y-axis on a log-log plot of peak particle velocity vs distance or range
$cc(L)$	-	centre to centre
$cc(L^3)$	-	cubic centimetre
$cf(L^3)$	-	cubic foot
cm/sec	-	centimetres per second
cm/sec^2	-	centimetres per second per second
$C_i(LT^{-1})$	-	local propagation velocity of stress wave
$C_i'(LT^{-1})$	-	average propagation velocity for certain interval
$C_L LT^{-1})$	-	propagation velocity of longitudinal stress or P-wave
$C_T(LT^{-1})$	-	propagation velocity of shear or S-wave
$C_w(LT^{-1})$	-	propagation velocity of stress wave in water
$d(L)$	-	diameter of specimen
$D(LT^{-1})$	-	detonation velocity
E	-	blast hole, east side of linear array
$fs(LT^{-1})$	-	feet per second
$g(LT^{-2})$	-	acceleration due to gravity
G	-	gage hole

h(D)	–	decay exponents on range for peak particle displacement in S-wave
HM	–	diamond drill hole size, 3 7/8 in. diameter
in./sec(LT^{-1})	–	inches per second
IP, ip	–	incident P-wave
is(LT^{-1})	–	inches per second
k(D)	–	decay exponents on range for peak particle velocity in S-wave
kg/cm^2	–	kilogram per square centimetre
ksc	–	kilogram per square centimetre
KB(FL^{-2})	–	kilobar or one thousand atmospheres
l(L)	–	length of specimen
m(D)	–	decay exponents on range for peak particle velocity in P-wave
m(L)	–	metre
m/sec(LT^{-1})	–	metres per second
ms(T)	–	millisecond
n(D)	–	decay exponents on range for peak particle displacement in P-wave
NRT(FLM^{-1})	–	ballistic mortar parameter
psi(FL^{-2})	–	pounds per square inch
P(MLT^{-2})	–	force
P-wave	–	compressional wave
P_d($ML^{-1}T^{-2}$)	–	detonation pressure
P_o(FL^{-2})	–	pressure parameter in theoretical analysis

$P_t(ML^{-1}T^{-2})$ — transmitted, imposed pressure

$P_w(ML^{-1}T^{-2})$ — shock pressure in water

$Q_u(FL^{-2})$ — uniaxial compressive strength

$r(L)$ — radius or radial distance

$r_c(L)$ — equivalent radius for spherical charge

$R_c(L)$ — crater radius

RP, rp — reflected P-wave

RS, rs — reflected S-wave

$sc(L^2)$ — square centimetre

$sf(L^2)$ — square foot

$si(L^2)$ — square inch

$S(ML^{-1}T^{-2})$ — stress behind the stress wave front

S-wave — shear wave

$S_i(ML^{-1}T^{-2})$ — initial peak pressure

$S_o(ML^{-1}T^{-2})$ — stress in front of the stress wave front

$S_p(ML^{-1}T^{-2})$ — peak stress

$t(T)$ — time

$t_d(T)$ — duration of shock pulse

$t_r(T)$ — shock pulse rise time

$T(T)$ — time after arrival of shock wave

$T_d(FL^{-2})$ — dynamic tensile strength

$T_s(FL^{-2})$ — static uniaxial tensile strength

$U(L)$ — displacement

$U_i(L)$ — intermediate value of displacement

$U_p(L)$	-	maximum value of displacement
U_w	-	change in displacement with time
$v_m(LT^{-1})$	-	peak radial velocity
$V(LT^{-1})$	-	particle velocity in the stress wave
$V(L^3M^{-1})$	-	specific volume behind the stress wave front
$V_c(L^3)$	-	crater volume
$V_i(LT^{-1})$	-	intermediate particle velocity in the stress wave
$V_o(L^3M^{-1})$	-	specific volume in front of the stress wave front
$V_w(LT^{-1})$	-	change in particle velocity with time
W	-	blast hole, west side of linear array
$x(L)$	-	coordinate in direction of x-axis
$\bar{x}$	-	scaled distance
$x_i(L)$	-	symbol for certain thickness of specimen
$y(L)$	-	coordinate in direction of y-axis
$z(L)$	-	coordinate in direction of z-axis
$Z(L)$	-	$z_o - z$
$z_o(L)$	-	optimum depth of explosive
$\alpha(D)$	-	direction of σ_1
$\gamma(D)$	-	shear strain
$\gamma(FL^{-3})$	-	unit weight or weight density $= \rho g$
$\epsilon(D)$	-	linear strain
$\epsilon_r(D)$	-	linear strain in the radial direction
$\epsilon_t(D)$	-	linear strain in the tangential direction
$\epsilon_\theta(D)$	-	linear strain in the tangential direction

$\lambda(L)$ -   wave length

μ -   micro or one millionth or microstrain

μs -   microsecond

ρ $(ML^{-3}$ or $FL^{-1}T^2)$ -   mass density

ρ (ML^{-3}) -   density

$\rho_e(ML^{-3})$ -   density of explosive

$\rho_w(ML^{-3})$ -   density of water

$\sigma(FL^{-2})$ -   normal stress

$\sigma'(FL^{-2})$ -   normal effective stress

$\sigma_i(FL^{-2})$ -   incident stress

$\sigma_r(FL^{-2})$ -   radial stress; reflected stress

$\sigma_\theta(FL^{-2})$ -   tangential stress

$\sigma_t(FL^{-2})$ -   tangential stress; transmitted stress

$\sigma_o(FL^{-2})$ -   peak radial stress in a shock

$\sigma_{yp}(FL^{-2})$ -   elastic limit or yield point

$\sigma_1(FL^{-2})$ -   major principal stress

$\sigma_2(FL^{-2})$ -   intermediate principal stress

$\sigma_3(FL^{-3})$ -   minor principal stress

$\tau(FL^{-2})$ -   shear stress

$\omega(T^{-1})$ -   angular frequency